NANOSTRUCTURED SPECTRALLY SELECTIVE COATINGS FOR HIGH-TEMPERATURE SOLAR THERMAL APPLICATIONS

Thesis

Submitted in partial fulfilment of the requirements for the degree of

DOCTOR OF PHILOSOPHY

By

JYOTHI J

(Register Number: PH13P01)

DEPARTMENT OF PHYSICS

NATIONAL INSTITUTE OF TECHNOLOGY KARNATAKA,

SURATHKAL, MANGALORE-575025

March, 2018

DECLARATION

I hereby declare that the Research Thesis entitled **"Nanostructured spectrally selective coatings for high-temperature solar thermal applications"** which is being submitted to the National Institute of Technology Karnataka, Surathkal in partial fulfilment of the requirements for the award of the Degree of **Doctor of Philosophy** in **Physics** is a *bonafide report of the research work carried out by me*. The material contained in this Research Thesis has not been submitted to any University or Institution for the award of any degree.

Jyothi J

(Register No. 135033PH13P01)

Department of Physics

Place: NITK, Surathkal

Date:

CERTIFICATE

This is to *certify* that the Research Thesis entitled **"Nanostructured spectrally selective coatings for high-temperature solar thermal applications"** submitted by   Jyothi J. (Register Number: **135033PH13P01**) as the record of the research work carried out by her, is accepted as the Research Thesis submission in partial fulfilment of the requirements for the award of degree of **Doctor of Philosophy**.

Research Supervisors

Dr. H. S. Nagaraja   **Dr. Harish C. Barshilia**

Assistant Professor   Chief Scientist and Head

Dept of Physics   Surface Engineering Division

NITK, Surathkal   CSIR-NAL, Bangalore

Date: Date:

                                                              Chairman-DRPC

Dedicated to my beloved dad

ACKNOWLEDGEMENT

ABSTRACT

A spectrally selective TiAlC/TiAlCN/TiAlSiCN/TiAlSiCO/TiAlSiO coating was deposited on stainless steel substrate and silicon substrates by unbalanced magnetron sputtering system. Each individual layer of the tandem absorber was optimized by varying the reactive gas flow rates (C_2H_2, N_2 and O_2) and target power densities (Ti, Al and Si). The optimized tandem absorber shows a solar absorptance of 0.960 and an emittance of 0.15 at 82°C, measured using solar spectrum reflectometer and emissometer, respectively. The refractive indices and extinction coefficients of the tandem absorber were studied using the phase-modulated spectroscopic ellipsometry. Absorption coefficient of each layer was calculated from the extinction coefficient of the layer. The results indicate that the first three layers (i.e., TiAlC, TiAlCN, and TiAlSiCN) are absorbing in nature, while TiAlSiCO and TiAlSiO act as intermediate and antireflection layers. The obtained refractive indices and extinction coefficients of the tandem absorber were used to simulate the reflectance of the deposited tandem absorber using SCOUT software. Simulated reflectance data of the tandem absorber showed a good agreement with the experimental data. The angular dependence of the selective properties of the tandem absorber was studied by measuring the reflectance spectra of the tandem absorber at different incident angles. The thermal emittance of the tandem absorber at high temperatures (80–500°C) was also studied in detail. At the temperature of 200°C, 300°C, 400°C and 500°C the tandem absorber shows the emittance of 0.152–0.157, 0.181–0.19, 0.214–0.246 and 0.251–0.275, respectively with an absorptance of ~0.930. These results show the good selectivity of the tandem absorber even at high operating temperatures (e.g., 500°C). The performance evaluation of the tandem absorber has been evaluated by heating it in air at 325 °C for 600 h and in vacuum upto 600°C for 910 h under cycling heating conditions without any significant degradation of the optical properties. Thus demonstrating its suitability for high-temperature solar thermal power generation applications.

Keywords: *Absorptance, Emittance, Tandem absorber; Selectivity, Ellipsometry, Extinction coefficient, Refractive index, Absorption coefficient, Thermal stability.*

CONTENTS

CHAPTER 3

DESIGN AND FABRICATION OF SPECTRALLY SELECTIVE TiAlC/TiAlCN/TiAlSiCN/TiAlSiCO/TiAlSiO TANDEM ABSORBER FOR HIGH-TEMPERATURE SOLAR THERMAL POWER APPLICATIONS

CHAPTER 4

EFFECT OF COMPOSITION ON SELECTIVE PROPERTIES OF THE TiAlC/ TiAlCN/ TiAlSiCN/ TiAlSiCO/ TiAlSiO TANDEM ABSORBER

solar and IR regions

LIST OF FIGURES

of wavelength and (e) '*k*' at 500 nm.

The samples were heated in air for 8 h at 500 and 600°C.

The adhesion remained unaffected after the thermal shock tests.

LIST OF TABLES

ABBREVATIONS

CSP	Concentrating solar power
UV	Ultra violet region
VIS	Visible region
NIR	Near infrared region
IR	Infra-red region
AM	Air mass
PVD	Physical vapor deposition
DC	Direct current
SSR	Solar spectrum reflectometer
TM	Transverse magnet
TE	Transverse electric
FTIR spectroscopy	Fourier-transform infrared spectroscopy
NIST	National Institute of Standards and Technology
ASTM	American Society for Testing and Materials
PID	A proportional-integral-derivative
XRD	X-ray diffraction
XPS	X-ray photoelectron spectroscopy
FESEM	Field emission scanning electron microscopy
EDAX	Energy dispersive analysis of X-rays
AFM	Atomic force microscopy
RMS	Root mean square
TEM	Transmission electron microscopy

CIE	International commission on illumination
JCDPS	Joint committee on powder diffraction standards
SCCM	Standard cubic centimeters per minute
RT	Room temperature
HT	High temperature

NOMENCLATURE

α	Solar absorptance
ε	Thermal emittance
C	Concentration ratio
A_a	Area of the collector aperture
A_r	Absorber energy
h	Planck's constant
k	Boltzmann's constant
σ	Stefan-Boltzmann constant
λ	Wavelength
f	Selectivity
T	Absolute temperature
F	Figure of merit
η	Efficiency of the selective coating
X	Solar concentration
q	Solar flux intensity
V_B	Bias voltage
R_a	Surface roughness
n	Refractive index
k	Extinction coefficient
E	Photon energy
E_g	Optical band gap

A_T	Tauc coefficient
P	Cauchy principal value
R_p	TM polarization
R_s	TE polarization
$R(\lambda, T)$	Spectral reflectance measured at temperature
$G(\lambda)$	Solar spectrum (ASTM-G173 AM 1.5 direct+ circumsolar)
$P(\lambda, T)$	Blackbody emission spectrum at T, given by Planck's law.

Chapter 1

INTRODUCTION

This Chapter gives introduction to the selective surfaces and their importance in the field of harnessing solar energy through photothermal conversion route. An overview of literature survey on various selective surfaces is discussed in this Chapter. This Chapter also concludes the scope and objective of the work.

1.1. INTRODUCTION

Now-a-days, the demand of energy increases day-by-day due to extrapolation of population, rapid industrialization, continuance of the economic growth, developing technology, etc., and this leads to excess consumption of fossil fuels (Cartalis et al., 2001). The dominant usage of the non-renewable resources contributes to the drastic change in environmental conditions by overloading the greenhouse gases (Dincer et al., 2000; Zekai et al., 2008). It is necessary to take some precautions to avoid or minimize the usage of the non-renewable resources and looking forward to utilize the renewable energy. Solar energy is the one of the best renewable energy resources, due to its abundance, cleanliness and falling cost (Sayigh et al., 2012).

Solar energy can be utilized in two ways: (1) converting solar energy directly into electricity (Photo voltaic) (2) conversion of solar energy into a thermal energy by using a special exchanger called solar collectors. Solar collectors are categorized in two types on the basis of concentration ratios. (i) Non–concentrating solar collectors (mainly used for low temperature applications) have the concentration ratio of 1. In case of concentrated solar powers (mainly utilized for power generation applications) have the concentrating ratio >1. This concentrating ratio is calculated from the geometrical characteristics such as (Kennedy et al., 2002; Selvakumar et al., 2012):

$$C = \frac{A_a}{A_r} \qquad (1.1)$$

where A_a is the collector aperture area; A_r is the energy absorber.

Concentrated solar power (CSP) consists of majorly three steps (i) concentrated mirrors are used to focus the solar radiation on heat collectors. (ii) Heat collectors convert the focused solar radiation in to thermal energy. (iii) The obtained thermal energy is absorbed by the heat-transfer fluid, which is circulated in the heat collectors, thus producing the steam. Turbines are used to generate electricity by the high pressure, super saturated steam. The efficiency of the CSP mainly depends on the heat collector receiver tubes. This indicates that the receiver tubes play an extensive role in converting solar energy into thermal energy. The increase in efficiency of the receiver tubes decreases the cost of CSP. Usually, a thermally conducting material such as stainless steel and super alloy substrates are used as receiver tubes. Basically metals are reflectors, which have low selective properties. It essential to improve the selective properties of the receiver tubes. So, spectrally selective coatings are utilized to enhance the efficiency of converting solar energy into thermal energy.

1.2. SOLAR AND THERMAL RADIATION

Fig. 1.1. shows the normalized spectral distribution of solar radiation and blackbody radiation at 500°C. Solar energy is radiant (electromagnetic) energy from the sun. It consists of 8% of UV, 42.3% of visible range and 49.4% of infrared radiation. Total wavelength range (0.3–50 µm) interested for solar thermal applications includes both solar spectrum range (0.3–4 µm) and spectral range of thermal radiation (2–50 µm) emitted by the surface (Iqbal et al., 1983).

The radiation in the electromagnetic spectrum ranging from 0.2–1000 µm is called thermal radiation, which is emitted by the object by virtue of its temperature. Planck's law gives the spectral distribution of radiation from a blackbody (Planck et al., 1914).

$$E_{\lambda b} = \frac{2\pi h c_0^2}{\lambda^5 [\exp\left(\frac{h c_0}{\lambda K T}\right) - 1]} \qquad (1.2)$$

where h = Planck's constant; k = Boltzmann's constant

The total energy emitted per unit area by a blackbody is given by

$$E_b = \int_0^\infty E_{\lambda b}\,d\lambda = \sigma T^4 \qquad (1.3)$$

σ is Stefan-Boltzmann constant = 5.6697×10^{-8} W/m^{2}K^4.
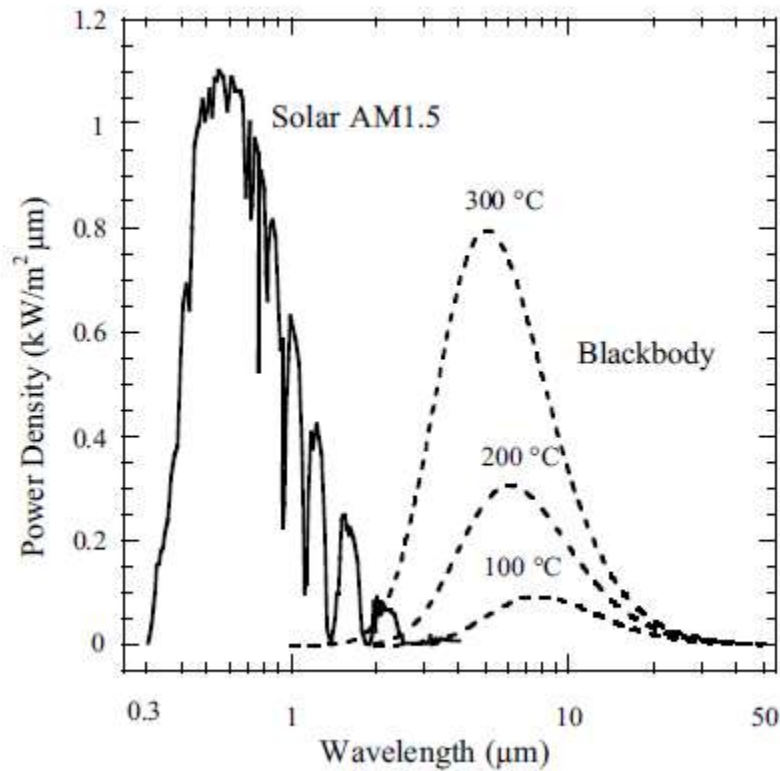
Figure 1.1: Solar hemispherical spectral distribution of solar irradiance and blackbody radiation spectrum at three different temperatures (100°C, 200°C and 300°C) (Tesfamichael et. al., 2000).

1.3. SPECTRALLY SELECTIVE COATINGS

Selective surfaces are the surfaces which have the high absorptance in the solar spectrum range (>90%) and low thermal emittance (<10%) in the IR region. Solar absorber is designed in such a way that plasma edge (where electrons in the material start vibrating collectively) has to be compared with the ideal characteristics of the material. Plasma edge of metals is located too far from UV to give sufficient solar absorptance. There are essentially three groups of metals which are differentiated by the metallic action of

produced electrons. If it is by *s*-electrons called noble metals, *sp* electrons called good metals and *d*-electrons means poor metals. The transition metals belong to this poor metals' category. In order to achieve the ideal characteristics of transition metals for spectrally selective coatings, one needs to use the hybridized bond between the *d*-electrons of transition metals and *sp* electrons of the impurity atoms such as: carbon, nitrogen, boron, oxygen, etc. (Seraphin et al., 1979; Duffie et al., 2006).

The spectral selectivity of a material is discussed here. If materials or surfaces can be found or synthesized, that they differentiate in their absorption, reflection or transmission characteristics above 2.0 µm (i.e., thermal range) and wavelength below 2.0 µm (i.e., solar range) then it may be possible to trap the solar energy. (i.e., to collect it by absorption but to prevent or minimize the thermal re-radiation loss). Such surfaces are called "selective". Therefore, these types of coatings have high absorptance in solar radiation and high reflectance in the long-wavelength radiation (Niklasson et al., 1983; Andersson et al., 1980; Srinivasa et al., 2015). In the context of solar thermal conversion, this can be summarized as: "The spectral selectivity indicates high absorptance in the visible region and low thermal emittance in the infrared region. In other words, the spectrally selective coatings should have low reflectance in the visible region and high reflectance in the infrared region". The schematic diagram of an ideal spectrally selective coating is shown in Fig. 1.2.
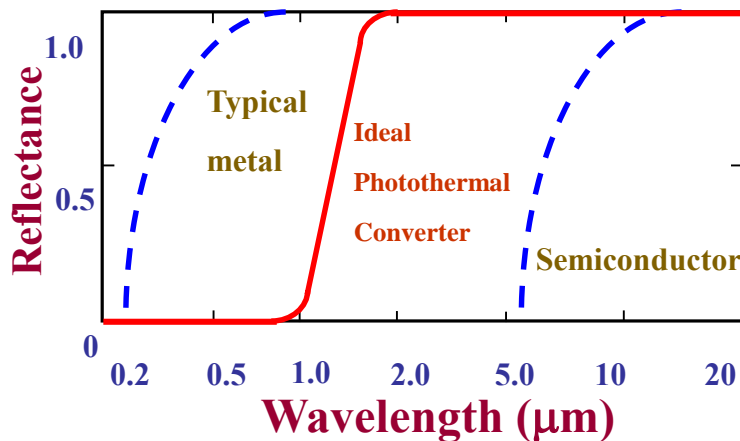
Figure 1.2: Schematic diagram of the ideal characteristic of a selective coating.

1.4. METHODS TO ACHIEVE SELECTIVE COATINGS

Various methods are used to achieve selective absorber coatings such as intrinsic absorption, metal-dielectric composite coating, multilayer absorber, textured and absorber-reflector tandem (Ritchie et al., 1977; Schon et al., 1994; Agnihotri et al., 1981; Harding et al., 1981; Cao et al., 2014; Atkinson et al., 2015; Lee et al., 2015; Atasi et al., 2017; Zhang et al., 2017).

1.4.1 Intrinsic absorption

Intrinsic absorption is a simplest type of design where material has intrinsic selective property. But no material in nature exhibits ideal intrinsic absorption property, as shown in Fig. 1.3(a).
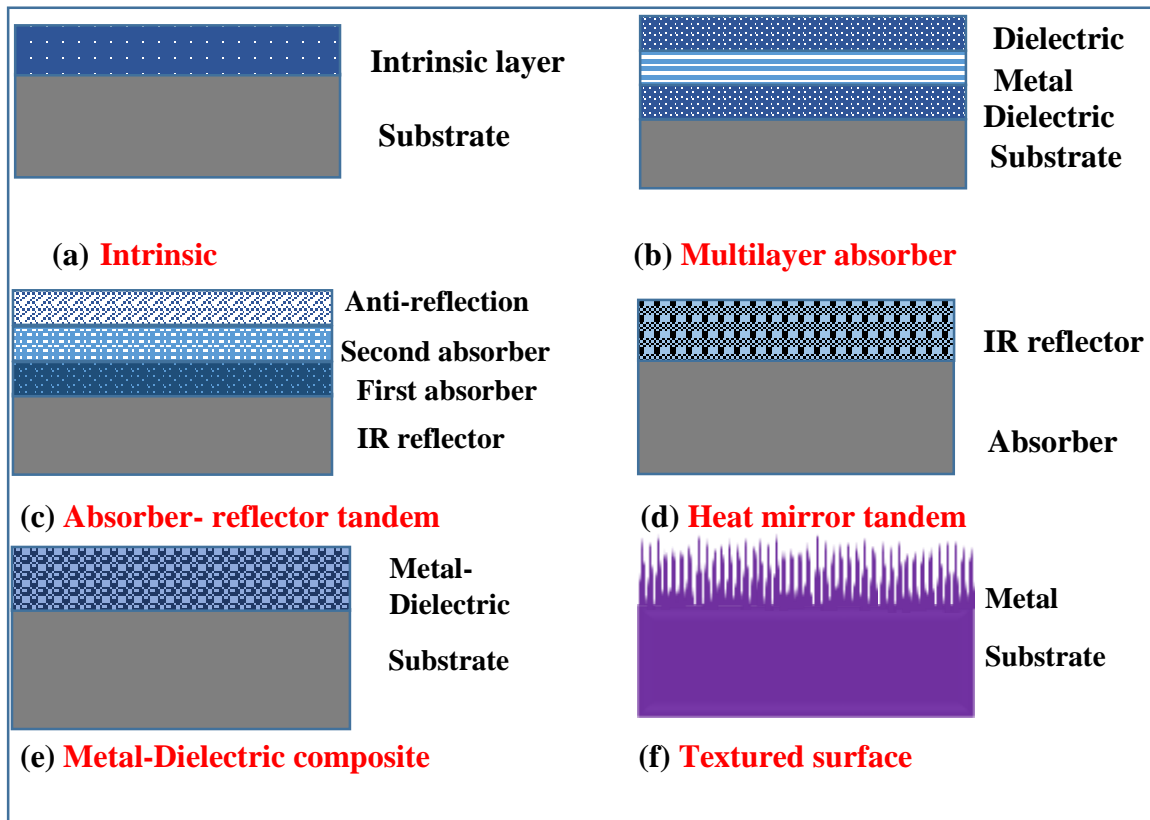
Figure 1.3: Different types of selective surfaces.

However, some transition metals and semiconductors indicate the existence of intrinsic property (Agnihotri et al., 1981; Randich et al., 1984) such as ZrB_2, HfC, MoO_3, V_2O_5, LaB_6, Fe_3O_4, TaC, HfB_2 etc., (Touloukian et al., 1974; Ehrenreich et al., 1975; Randich et al., 1984; Gonzale et al. 2011, Sani et al. 2011, Sani et al. 2012). Among all these types of materials plasmon frequency of ZrB_2 roughly matches with the ideal cutoff wavelength. The main drawback of intrinsic absorption materials is the changeover of low to high reflectance occurs at too short wavelengths.

1.4.2. Multilayer absorber

One of the efficient ways to achieve selective properties is the multilayer absorber. It achieves the selective properties due to destructive interference and multiple reflections of the coating. It consists of several alternate dielectric and semitransparent metallic materials as shown in Fig. 1.3(b). A thin metallic layers is sandwiched between the dielectric layers. This top dielectric layer reduces the visible reflectance and leads to high absorption. Various combinations of multilayer absorber coating designed are Mo, Ag, Cu, Ni and dielectric layers Al_2O_3, SiO_2, CeO_2, and ZnS, etc., for high temperature solar thermal applications. (Andersson et al., 1980; Craighead et al., 1981; Fan et al. 1977; Kumar et al., 1983; Kennedy et al., 2002; Zhang et al. 2008).

1.4.3. Tandem absorber

Tandem absorber coatings comprise with two or more different materials/layers. Selective properties of the coating can be achieved due to the different optical properties of the materials. Tandem absorber coatings are majorly divided into two types: (i) Absorber-reflector tandem (i.e., Dark mirrors) and (ii) Heat mirrors.

(i) Absorber-reflector tandem

Absorber-reflector tandem absorber coating consists of a metal substrate that acts as an IR reflector and a thin selective layer deposited on the substrate acts as an absorbing layer. Thus, these type of materials have high solar absorptance in the solar region and low

6

emittance in the IR region. Absorber layer is designed in such a way that metal volume fraction decreases from the substrate to the top layer of the absorber, as shown in Fig. 1.3(c). In the present work, this concept has been used to deposit the designed tandem absorber coating. The detailed explanation about the dependence of thickness of the layer, metal volume fraction, refractive index of the layers is discussed in Chapter 4 and Chapter 5.

(ii) Heat mirrors

Heat mirrors are vice versa of dark mirrors, which consist of absorbing substrate covered with a thin IR reflecting layer. As depicted in the Fig. 1.3(d), the top layer of IR reflects the radiation above the wavelength $\lambda > 3$ µm and transmits the solar region $\lambda < 3$ µm. So, that the absorbing substrate absorbs in the solar region. This heat mirrors works in reverse to the normal tandem absorbers. Highly doped InO_2, SnO_2 or the combination of both ITO have been used to produce this type of materials (Goldner et al., 1976).

1.4.4. Metal-dielectric composite coating

Metal-dielectric composite or cermet is one of the substantial ways to achieve the spectrally selective coatings. Metal-dielectric composite coatings consist of metal particles embedded in a dielectric matrix, as shown in Fig. 1.3(e). The cermets are generally considered to have the great promising for high temperature solar thermal applications (Chester et al., 2011). These coatings are transparent in the IR region but highly absorbing in the solar region due to inter-band transition of metals and small particle resonance. So many combination of metals such as Co, C, W, Mo, Ag, Cu and Ni with dielectrics such as Al_2O_3, SiO_2, CeO_2, ZnS are used for high temperature applications (Antonaia et al., 2010; Xue et al., 2013; Barshilia et al., 2008, 2014; Nuru et al., 2012; Cao et al., 2014).

1.4.5. Textured absorbing surfaces

Textured coating design is mainly based on the geometric trapping. Creating a texture on highly reflecting metal substrate with required geometry absorbs the solar energy by trapping light through multiple reflections as shown in Fig. 1.3(f). This textured dendrites look like a rough surface in the visible region and smooth surface in the IR region. A chemical vapor deposition and sputtering method were used to create dendrite structure on surface of the rhenium, tungsten and nickel, copper and stainless steel (Cuomo et al. 1975; Seraphin et al., 1976; Harding et al., 1981; Alejandro et al., 2006).

1.5. LITERATURE ON HIGH-TEMPERATURE SOLAR SELECTIVE COATINGS

So many combination of materials and above discussed methods are utilized to develop selective coatings. A large number of coatings have been developed by the researchers with the combination of metal and dielectric multilayers. Coatings such as Pt-Al_2O_3, Ni-Al_2O_3, Cr-SiO, $MoSiO_2$, etc. (Craighead et al., 1981; Antonaia et al. 2010; Wang et al., 2012) exhibit good selective properties but they fail at high operating temperatures. At higher temperatures the metal layer in the coating undergoes the inter diffusion or oxidation, which affects directly on the performance of the selective coatings. To overcome this problems researchers have investigated a combination of transition metal with nitrides, oxy-nitrides, oxides, etc. These materials can be utilized for selective coating by properly optimizing the stoichiometry. Schuler et al., studied structural and optical properties of single TiAlN layer, which shows the absorptance of 0.80 (Schuler et al., 2001). Ritchie and Window first proposed the graded selective coatings (Ritchie et al., 1977). A new concept double cermet layer structure was proposed by Qu-chu and Mills by which they achieved the highest performance of selective coating (Qu-chu et al., 1992). Using this concept so many selective coatings have been developed for better performance. Recently, Liu et al. designed a new selective coating SS/Fe_3O_4/Mo/TiZrN/TiZrN/SiON, which exhibit high

absorptance of 0.95 with an emittance of 0.08. This coating shows the high thermal stability in air upto 500°C in vacuum for 300 h (Liu et al., 2014). Du et al, optimized a selective coating for high temperature applications with a combination of TiAlN and AlN. The high and low metal volume fractions of TiAlN acts as an absorber and AlN acts as an anti-reflection layer. The optimized absorber shows the absorptance of 0.945 and emittance of 0.04 (Du et al., 2011). Krishna et al. fabricated a functional multi-layer nitride coating1 with TiAlCrN, TiAlN and AlSiN. The major absorber layer in the coating is TiAlN and an anti-reflection layer is AlSiN. TiAlCrN acts as an IR reflector. The fabricated coating shows the absorptance of 0.91 with an emittance of 0.07 (Krishna et al., 2013). Soum-Glaude et al. reported the optical characteristics of low and high refractive index of TiAlN with an anti-reflection layer of Al_2O_3. Coating shows the high absorptance of 0.93 with an emittance of 0.22 at 500°C (Soum-Glaude et al., 2015). Ping et al. fabricated an absorber coating $Al/NbMoN/NbMoON/SiO_2$ with an absorptance of 0.948 and an emittance of 0.11 (Ping et al., 2017). Ning et al., deposited a new selective coating $Mo/ZrSiN/ZrSiON/SiO_2$ by using the magnetron sputtering system. The absorptance of the coating is 0.94 with an emittance of 0.06 (Ning et al. 2017). Zhou et al. developed a new selective coating for high temperature applications AlCrSiN/AlCrSiON/AlCrO with an absorptance of 0.958 and emittance of 0.14. The designed coating shows the high thermal stability upto 600°C for 600 h in air (Zhou et al., 2016). Barshilia et al. have developed a large number of selective coatings for high temperature applications, by varying the metal volume fractions such as Ti/AlTiN/AlTiON/AlTiO, TiAlN/AlON, $TiAlN/AlON/Si_3N_4$, $NbAlN/NbAlON/Si_3N_4$ for high temperature applications. The coatings show an absorptance of >0.94 with low emittance < 0.1 (Barshilia et al. 2007; 2008; 2011; 2014). Similarly, Selvakumar et al. have designed selective coatings of AlHfN(H)/AlHfN(L), Ti/AlTiO/CoO/CNT, $HfMoN/HfON/Al_2O_3$ for high temperature applications with an absorptance of >0.91 and emittance of < 0.1 (Selvakumar et al., 2012; 2012).

1.6. SCOPE OF THE WORK

The efficiency of photo-thermal conversion can be enhanced by using the appropriate spectrally selective coating in solar collectors. It is clear from the literature that the degradation in selective properties of the coating at high operating temperatures is due to their unstable microstructure of the selective coatings (Kennedy et al., 2002; Selvakumar et al., 2012). This is the major problem for high temperature solar thermal applications. Materials such as: titanium, zirconium or hafnium metal carbides have the highest melting points in nature, high hardness, improved wear, corrosion and oxidation resistance and are believed to be promising materials for high temperature solar thermal applications (Kosolapova et al., 1971; Toth et al., 1971).

1.6.1. Transition metal carbides

Transition metal carbides of group IV and V exhibit special physical and mechanical properties than the nitrides such as high hardness, high melting point, high elastic modules, good heat and thermal conductivity along with that they exhibit the high chemical stability. Thus, these materials are called as refractory compounds (Kosolapova et al., 1971; Toth et al., 1971).

(i) Crystal structure

According to the crystallography, transition metal carbides are interstitial compounds with a complex and different crystal structure. Especially for binary compounds, the properties and crystal structure are greatly influenced by the geometry of the interstitial sites. According to the Hagg's rule, the change in crystal structure depends on the nonmetal and metal radii ratio.

$$r = \frac{r_{nonmetal}}{r_{metal}} \qquad (1.4)$$

If r > 0.59, the complex structure was observed rather than the simple structure due to the accommodation of large number of non-metal atoms in the host metallic cage (Toth et al., 1971).

If r < 0.59 the metal atoms forms the simple fcc, hcp or hexagonal structures with the non-metals in the corresponding tetrahedral or octahedral interstitial sites of the host metal structure as shown in Fig. 1.4. Even, majority of the transition metal carbides show r < 0.59 (Toth et al., 1971).

The special properties of the transition metal carbides are strongly associated with the interatomic bonding. Carbon atoms occupy the interstitial sites in the metallic lattice to achieve the strong bonding between the metal –nonmetal and metal –metal bonding.
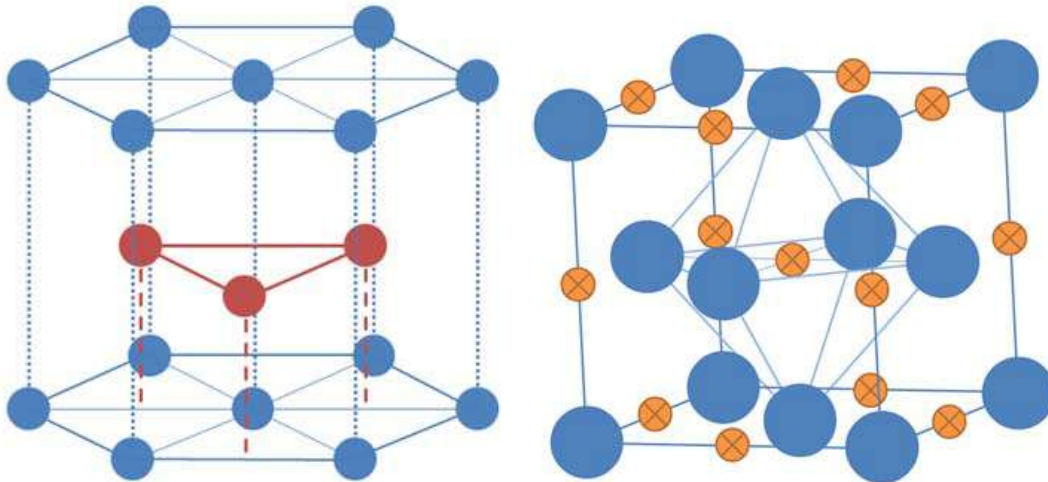
Figure 1.4: Two examples of interstitial sites in a hexagonal (left) and fcc (right) structure (namely trigonal sites, in red, and octahedral sites, in orange).

(ii)   Bonding in transition metal carbides

Transition metal carbides exhibit both metallic and ceramic properties. Thus, the bonding in the compounds is a combination of metallic, covalent and ionic properties. Recent studies have also proved that the bonding in the transition carbides is most likely to be metallic rather than the covalent and ionic components. The strength of the bond

strongly affects the special properties of the compounds. The hardness and stability of these compounds can be determined or controlled by the composition of the non-metallic material. It is well known that the bonding in the transition carbides is due to the interaction of 2s and 2p of nonmetal atoms to the metal'd' orbitals. The Engel-Brewer theory states that the crystal structure of the compound is associated with the number of sp electrons (Brewer et al., 1967; Oyama et al., 1996). The increase in amount of the sp electrons leads to change in the crystal structure from the bcc to hcp to fcc. Transition metals of group IV and V exhibit the fcc structure due to the incomplete filling of d orbital in the metal.

(iii) Properties of transition metal carbides

Table 1.1 shows the properties of the transition metal carbides. The nitrides and carbides of the transition metals show the highest melting point, hardness, etc.

Material	Melting Point (°C)	Micro-hardness (Kg/mm^2)	Modulus of elasticity (GPa)
TiC	3370	3000	451
ZrC	3670	2700	348
HfC	4170	2600	352
VC	2970	2900	422
NbC	3870	2000	338
TaC	4070	1800	285
Cr_3C_2	2070	1400	373
Mo_2C	2770	1500	533
WC	3070	2200	696

Table 1.1: Properties of transition metal carbides.

But when we compare both the nitrides and the carbides of the transition metals, transition carbides show the best properties in terms of melting point, hardness, etc. (Toth et al., 1971).

1.7. LITERATURE ON CARBIDE BASED COATINGS

The attractive properties of the transition metal carbides are widely used in industrial applications. Recently, so many combinations of titanium compounds, such as pure nitride (TiN) to the pure carbide (TiC), along with carbo-nitride (TiCxNy), oxycarbide (TiCxOy) and the oxy-carbo-nitride phases (TiCxNyOz) are being used for various applications. TiC possesses a higher hardness with an extraordinary wear resistance than TiN (Santhanam et al., 1990). Titanium carbo-nitride (TiCN) is used to coat metals in order to increase hardness, which have the properties of both nitrides and carbides (Santhanam et al., 1990). Ei-Awadi et al., 2013, studied the characterization and properties of the TiAlC layer. TiC shows the high hardness and scratch resistance; incorporating aluminum to the TiC layer shows the improved tribological and oxidation resistance properties (Ei-Awadi et al., 2013). Wihelmsson et al. proposed the nanocomposite coating TiAlC. The degree of nanocrystalline and amorphous nature of the coating can be tuned by varying the carbon concentration. Mechanical and friction of the coating also depends upon the carbon composition in the TiAlC coating. TiN coating is widely accepted in the industrial applications due to its wear resistance. The oxidation resistance of the TiN is increased by introducing the aluminum in the coating. The promising approach to improve the wear resistance of the coating is by adding carbon to the TiAlN (Wihelmsson et al., 2006). Zhang et al. studied the influence of carbon in TiAlCN coating deposited by magnetron sputtering system. The increase in carbon reduces the friction coefficient of the coating. Silicon nitride based coatings have the high fracture toughness and hardness with an excellent wear resistance. This type of coating shows the high thermal stability (Petzow et al., 2002). Shtansky et al. investigated the comparison of TiAlSiCN and TiCrSiCN coatings. The

Material	Hardness	Heat of formation Kcal/mole	Crystal structure	Melting point (°C)	References
TiC	27 GPa	-44.1	Cubic	3370	Azadi et al., 2013; Toth et al., 1971; Robert et al.,1982
TiAlC	30 GPa	-	Cubic	2100	Harsh et al., 2015; Robert et al., 1982
Silicon carbide	23 GPa	-15.36	Hexagonal	2830	Du et al., 2012; Haynes et al.,2011; Muranaka et al., 2008
Aluminum carbide	7 GPa	-49.9	Rhombohedral	2100	Gesing et al., 1995; Yate et. al., 2009
TiN	30 GPa	-80.8	Tetrahedral	2950	Krishnan et al., 2013; Toth et. al., 1971
AlN	11 GPa	-78	Wurtzite	2200	Yate et al., 2009; Robert et al.,1982
Si_3N_4	14-19 GPa	-177.7	Cubic	1900	Yamada et al., 2004 Jiang et al., 2001
TiAlCN	41 GPa	-	Cubic	-	Jang et al., 2005
TiAlSiCN	46 GPa	-	Cubic	-	Shtansky et al., 2011
Silicon carbo-oxide	23 GPa	-	-	1000	Kathy et al., 2016
Titanium oxide	12 GPa	-210	Tetragonal	1843	Leng et al., 2003; Dubrovinsky et al., 2011
Aluminum oxide	14-16 GPa	-400.5	Trigonal	2000	Patnaik et al., 2002
Silicon dioxide	13 GPa	-217	Cubic	1713	Vila et al., 2003; Haynes et al., 2011; Levien et al., 1981

Table 1.2: Properties of the combinations of titanium, aluminum, silicon carbides, nitrides, carbo-nitrides, carbo-oxides and oxides.

TiAlSiCN coating shows the good thermal stability and oxidation resistanceup to 1300°C in vacuum and 1000°C in air (Shtansky et al., 2011). Oxy-carbides such as Al_2OC, Al_4O_4C and TiAlSiCO have also been reported to exhibit high thermal stability up to 1400°C as they form Al_2O_3, SiC, SiO_2, TiC and Al_2OC compounds after annealing at high temperatures (Sitnikov et al., 2004; Mikhelashvili et al., 2006; Shi et al., 2007; Edlmayr et al., 2010). Table 1.2. shows the properties of the combination of titanium, aluminum, silicon carbides, carbonitrides, carbo-oxides and oxides.

It is clear from the literature that the combination of titanium, aluminum and silicon carbide, carbonitrides, carbo-oxides and oxides such as TiAlC, TiAlCN, TiAlSiCN, TiAlSiCO and TiAlSiO are the materials capable to withstand at high operating temperatures. The recent literature on the solar selective coating also shows that the optical properties of the titanium can be tuned by doping to achieve selective properties, whereas aluminum and silicon increase the oxidation and thermal stability of the coating. So, it is worthwhile to use these materials for high temperature solar thermal applications.

1.8 CHARACTERISTICS OF THE SELECTIVE COATINGS

When light is incident on a surface, some part of light is absorbed, reflected and transmitted by the surface. So, conservation of energy states that the sum of the light absorbed, reflected and transmitted is equal to 1. The performance of the selective surfaces is estimated by using the two parameters such as solar absorptance and thermal emittance.

1.8.1 Solar absorptance

It is defined as the ratio of amount of light is absorbed by the surface to the total incident radiation (Jackson et al., 1999).

$$\alpha(\theta) = \frac{\int_{\lambda_1}^{\lambda_2}(1-R(\lambda,\theta)).G(\lambda)d\lambda}{\int_{\lambda_1}^{\lambda_2}G(\lambda)d\lambda} \qquad (1.5)$$

where λ_1 (0.25 µm) and λ_2 (2.5 µm) are the minimum and maximum solar wavelengths, respectively, $G(\lambda)$ is radiative flux and θ is angle of incidence . For opaque substrate T = 0.

1.8.2 Thermal emittance

The directional thermal emittance gives the performance of the selective coating in IR region. It is defined as a ratio of amount of heat emitted by the surface to the blackbody at the same temperature (Kuhn et al., 1978; Dewitt et al., 1988).

$$\varepsilon(T,\theta) = \frac{\int_{\lambda_1}^{\lambda_2}(1-R(\lambda,T,\theta)).B(\lambda,T)d\lambda}{\int_{\lambda_1}^{\lambda_2}B(\lambda,T)d\lambda} \qquad (1.6)$$

where $B(\lambda,T)$ is blackbody emission spectrum at T.

λ_1 and λ_2 are 2.5 µm and 25 µm , respectively.

The selectivity (*f*) of the selective coatings is measured by the ratio of the solar absorptance of the surface to the thermal emittance of the surface. Hence high value of '*f*' indicates the good performance of the surface.

1.9 HIGH TEMPERATURE EMISSIVITY

Emissivity is a key parameter in calculating the thermal losses in the solar collectors. As discussed above, generally the selective surfaces are studied from room temperature to <100 °C. It is important to study the selective properties at high operating temperatures, because the performance of the selective coatings can estimate at these temperatures. So, many methods are being used to calculate the high temperature emissivity.

1.9.1 Literature on High-Temperature Emissivity Measurements

In order to measure the emittance at higher temperatures, calorimetric or (spectro) radiometric/photometric methods on heated samples can be used. Calorimetric methods measure the temperature elevation of a fluid heated by the radiative emission of the hot sample (Jaworske et al., 1997; Effertz et al., 2016). (Spectro) radiometric/photometric methods either measure the (spectral) emissive power of the hot sample in the infrared

region (with a FTIR spectrometer) compared with known blackbody references (Cao et al., 2012; Bartelmeß et al., 2014; Brodu et al., 2015; Giraud et al., 2016; Mercatelli et al., 2016; Ren et al., 2016), or the (spectral) infrared reflectance R of the sample thanks to a reflectometer (Hanssen et al., 2007; Bartelmeß et al., 2014; Soum-Glaude et al., 2017;). The reflectometer can be equipped with an integrating sphere (Hanssen et al., 2007; Bartelmeß et al., 2014) or a semiellipsoidal infrared mirror (Soum-Glaude et al., 2017) for directional hemispherical or hemispherical directional measurements, respectively. It is then assumed that the emissivity is $1 - R$ (for opaque materials) according to Kirchhoff's law of radiation. Other examples of these techniques can be found in the literature (Markham et al., 1990; Qi-chu et al., 1992; Woskov et al., 2002; Moore et al., 2011; Daniel et al., 2015).

Each of these techniques has its drawbacks. In calorimetric measurements, the difficulty arises from the necessity to have a very efficient insulation of the measuring system to avoid parasitic heat losses and accurately estimate the sample emissivity (He et al., 2009). In radiometric techniques where the emissive power is directly measured, the accuracy is conditioned to the control and knowledge of the emissive power and temperature of the reference blackbody (He et al., 2009), as well as to the control of the sample temperature (Hanssen et al., 2007). In high temperature reflectometry measurements one has to assume that Kirchhoff's law of radiation is valid for the considered material, so that emittance can be deduced from reflectance, which is not necessarily the case. All these techniques are valid ways to retrieve the emittance of a sample if they are implemented with caution, and lead to similar results (Bartelmeß et al., 2014).

1.10 PERFORMANCE EVALUATION OF THE SELECTIVE ABSORBER

1.10.1 Figure of merit and absorber efficiency

(i) Figure of merit

Sergeant et al. stated the merit function of the tandem absorber $F(T)$ (Sergeant et al., 2009).

It defined by the absorptance (α), emittance (ε) and the operating temperature (T).

$$F(T) = \propto_{solar} \times [1 - \varepsilon_{thermal} T] \qquad (1.7)$$

To achieve the better value of the figure of merit, low emittance with high absorptance is preferable.

(ii) Photo-thermal conversion efficiency

Cinderella and Ho et al. proposed the efficiency of the selective coating to convert solar to thermal energy, at a particular temperature, is defined as (Cinderlla et al., 2007; Ho et al., 2012):

$$\eta = \alpha - \left(\sigma \varepsilon T^4 / Xq\right) \qquad (1.8)$$

where α is solar absorptance, ε is thermal emittance of the selective coating at a temperature T, σ is Stefan-Boltzmann constant, X is solar concentration and q is solar flux intensity. Therefore, in order to increase the efficiency of the photothermal conversion, the selective coating should maintain the selective properties (i.e., high absorptance and low emittance) even at high operating temperatures (> 450°C). It is, therefore, very important to know the emissivity of the selective coating at high temperatures.

1.10.2. Thermal stability

One of the critical factors to study the tandem absorber is performance of the selective absorber at high operating temperatures. Usually, tandem absorber degrades at higher temperatures due to the lack of thermal stability or oxidation of the absorber, which leads to reduced optical performance of the tandem absorber. The decrease in optical performance of the tandem absorber results in maintenance cost of the coated substrate (e.g., receiver tubes and panels). It is necessary to study the long-term thermal stability of tandem absorber at different temperatures in different environments such as air and vacuum environments to estimate the performance, cost and service life of the selective coating.

1.11. DEPENDENCE OF REFRACTIVE INDEX TO ACHIEVE SELECTIVE PROPERTIES OF THE COATINGS

A recent literature on solar absorbing coatings shows that the different methods are being used to achieve selective properties. Among these, tandem absorber method shows the great interest on literature due to its promising nature at high temperatures applications (> 400°C). It is observed from the literature that the basic structure of the tandem absorber

consist of an absorber layer, a semitransparent layer and an anti-reflection layer. In this thesis, to achieve a best thermal stability coating with selective properties, absorber layer is divided into three layers along with one semitransparent and anti-reflection layers. Each layer of the tandem absorber has its own importance such as absorber itself acts as a strong absorber in the solar spectrum region, whereas the antireflection layer enhances the transmission of light in the solar region by eliminating the reflection in the region. The whole stack of the tandem absorber acts as an effective filters.

It is well known from the previous works that the optimization of the each layer depends upon the refractive index of the materials. Various methods are utilized to obtain the selective properties of the tandem absorber.

(i)   The stack of the tandem absorber is arranged in such a manner with an alternative high and low refractive index of the layers.

(ii)   The refractive index of the each layer in the tandem absorber decreases from substrate to the top layer.

(iii)   Increasing the refractive of each individual of the tandem absorber from substrate to the top layer.

In order to achieve the selective properties of desired materials (i.e., TiAlC, TiAlCN, TiAlSiCN, TiAlSiCO, TiAlSiO) for the high temperature applications, each layer of the tandem absorber is designed in such a way that refractive index of the layer decreases from substrate to the top layer. The refractive index of the material directly relates to the metal volume fraction of the layer. The designed tandem absorber of the present work was optimized by varying the metal volume fraction and thickness of the layer.

1.12. OBJECTIVES OF THE WORK

➢ The aim of the proposed work is to achieve the spectrally selective solar absorber coating for high temperature applications by using a combination of titanium, aluminum and silicon carbides, carbonitrides as absorbing layers (i.e., TiAlC, TiAlCN, TiAlSiCN). Further a combination of Ti, Al and Si carbo-oxides and oxides was used as an intermediate and antireflection layers (i.e., TiAlSiCO and TiAlSiO).

➢ To study the effect of composition and thickness on each individual layer of the tandem absorber by varying the reactive gas flow rate and deposition time of the layer. Each individual layer of the tandem absorber was optimized in such a way that the refractive index decreases from the bottom to top layer.

➢ To fabricate the designed tandem absorber by using four cathode reactive DC unbalanced magnetron sputtering.

➢ To study the optical performance (i.e., reflectance, absorptance, etc.), refractive index and extinction coefficient of the each individual layers of the deposited tandem absorber.

➢ To study the structural properties, emittance at high temperatures (T > 500°C) and photothermal conversion efficiency of the designed tandem absorber.

➢ To compare the results obtained from the experimental and simulated data.

➢ To study the thermal stability of the tandem absorber in different environments at different temperatures.

1.13. OUTLINE OF THE THESIS

The present thesis comprises of 7 Chapters and each Chapters are summarized concisely below.

Chapter 1: This Chapter gives introduction to the selective surfaces and their importance in the field of harnessing solar energy through photo-thermal conversion route. An overview of literature survey on various selective surfaces and their fabrication methods are also discussed in this Chapter. This Chapter concludes with the scope and objective of the work.

Chapter 2: Chapter 2 describes, the detailed experimental methods used for deposition of the tandem absorber. Characterization technique used to analyze the optical, structural and electrical properties of the tandem absorber have also been discussed. In addition, the details of SCOUT software are also given in this Chapter, which was used to simulate the obtained experimental data.

Chapter 3: In this Chapter, design and fabrication of the TiAlC/TiAlCN/TiAlSiCN/ TiAlSiCO/TiAlSiO tandem absorber are discussed. Importance of incorporating each layer on absorptance and emittance of the coating is analyzed in detail. Performance of the tandem absorber at different temperatures for short duration is also studied.

Chapter 4: This Chapter reveals the dependence of optical properties on composition and thicknesses of each individual layers of the tandem absorber to achieve spectrally selective properties.

Chapter 5: This Chapter is mainly concentrated on the significance of refractive index and extinction coefficient of the individual layers of the tandem absorber to achieve selective properties. The angular dependence of the tandem absorber on the selective properties is also studied in detail.

Chapter 6: In this the thermal emittance of the tandem absorber at higher temperatures (80°C–500°C) is studied in detail. Adhesion of the coating and effect of annealing temperature on roughness of the tandem absorber are also analyzed in this Chapter.

Chapter 7: This Chapter dedicates the overall summary of the results with justification described in previous Chapters. Moreover, this Chapter includes few propositions for the future work.

Chapter 2

Experimental details

This Chapter describes the experimental techniques used to deposit the tandem absorber. Characterization techniques used to analyze the tandem absorber such as optical and structural properties etc., are thoroughly described in detail.

2.1 Introduction

As studied in Chapter 1 solar selective coatings play a vital role in solar collectors. It is crucial to achieve the selective properties with thermal stability of the coating at high operating temperatures. Sputtering is one of the techniques widely used for the deposition of the solar selective coating, due to its ability to fabricate coating with controlled composition and thickness. It is easy to achieve better adhesion using sputtering process. Further, all the PVD processes are environmental friendly. (Kennedy et al., 2002; Selvakumar et al., 2012).

2.2 Experimental details

A Four Cathode Reactive DC Unbalanced Magnetron Sputtering System was used to deposit the solar absorber coatings. The schematic diagram of the four cathode reactive DC unbalanced magnetron sputtering system is shown in Fig. 2.1. The sputtering system consists of 760 mm diameter, 600 mm cylindrical double walled water-cooled vacuum chamber. It comprises of four direct cooled DC unbalanced magnetron cathodes with the target diameter of 7.25 inches mounted horizontally in opposed-cathode configuration, substrate holder plate for mounting three-dimensional objects with planetary rotation, heating facility and vacuum gauges, etc. Sputtering chamber is evacuated with the help of turbo molecular pump with a pumping speed of 900 lit/sec backed by a direct drive double stage rotary vacuum pump. Four number of ENI make 5 kW asymmetric-bipolar pulsed plasma generators (Model No.: RPG-50, frequency of 100 kHz, pulse width of 2976 ns, duty cycle of 30%, reverse bias of +37 V) were used as sputtering power supplies and a

1.5 kW DC power supply was used for substrate bias and ion bombardment.
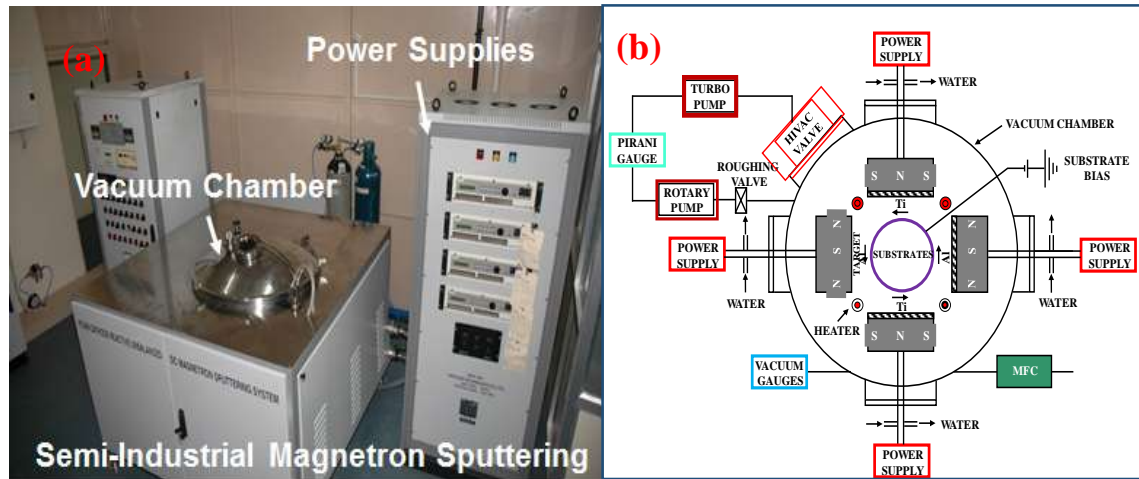
Figure 2.1: The four-cathode reactive DC unbalanced magnetron sputtering system. (a) Photograph and (b) Schematic diagram.

2.2.1 Substrate cleaning

Stainless steel substrates (30 mm×30 mm×2 mm) were used to deposit the designed tandem absorber. Before depositing the tandem absorber, substrates were metallographically polished to get smooth surface. Cleanliness of the substrate affects the film growth and adhesion of the tandem absorber. So, the substrates were ultrasonically cleaned in acetone and isopropanol to remove the contaminants like matter flakes, grease, fingerprints, etc. Coatings were also deposited on Si and glass substrates for various measurements.

2.2.2 Plasma cleaning

Cleaned substrates were placed inside the vacuum chamber and then evacuated the chamber to a base pressure of 8×10^{-4} Pa. The substrates were cleaned by in-situ of Ar ion bombardments (bias voltage (V_B): -1000 V) for 15 min to remove native oxide presence on the surface of the substrate.

2.2.3 Coating deposition

Deposition of the tandem absorber was carried out using two Ti (99.95%), one Al (99.9%) and one Si (99.9%) targets, which were sputtered in high purity (99.999%) gases such as $Ar + C_2H_2$, $Ar + C_2H_2 + N_2$, $Ar + C_2H_2 + O_2$ and $Ar + O_2$ plasmas, respectively. The flow rates of gases were controlled by mass flow controllers (MKS Type 247D four-channel mass flow controller power supply). The pressure inside the vacuum chamber during the deposition was accurately controlled by capacitance manometer (MKS make, Model 626 A). The distance between the substrate to target was 10 cm. In order to improve the adhesion of the coating a substrate bias (V_B = -100 V) was used. Uniformity of the coating was achieved by substrate rotation facility. In order to densify the coating, the deposition of the tandem absorber was carried out at a substrate temperature of 300°C.

2.3 ANNEALING STUDIES

Annealing studies of the designed coating were carried out in different environments such as in air and vacuum. The coated samples were heat treated in air for 2 h in a resistive tubular furnace at different temperature ranging with a heating rate of 10 °C/min.

The thermal stability of the coating in vacuum was also studied in a vacuum annealing system (6.0×10^{-4} Pa) at the different temperature ranges of 300–900 °C with a heating rate of 10 °C/min. Long term thermal cycling heating experiments were also carried out in both air and vacuum, where in the samples were heated and cooled several times and their optical properties were studied.

2.4 CHARACTERIZATION TECHNIQUES

2.4.1 Emissometer

Emittance is defined as a ratio between the amount of light reflected from a surface to the perfect blackbody at the same wavelength and temperature. In these studies, thermal emittance of the tandem absorber was measured by using Emissometer (Model AE1, M/s Devices and Services). Fig. 2.2. shows the setup of the emissometer.

Figure 2.2: Photograph of the emissometer.

In this instrument there is no need to heat the sample before measuring the emittance because the detector portion of the emissometer is heated electrically up to 82°C. Before measuring the sample, the emissometer was calibrated by using the high and low standards with emittance values of 0.88 and 0.05, respectively. The accuracy of the emissometer is 0.01 units (Barshilia et al., 2008).

2.4.2 Solar Spectrum Reflectometer (SSR)

The absorptance of the deposited tandem absorber was studied by using the Solar Spectrum Reflectometer (Model SSR-ER, M/s Devices and Services). A tungsten filament is used as a source of diffuse illumination at the sample port. A high absorbing materials is calibrated by using a blackbody cavity.

Figure 2.3: Photograph of the solar spectrum reflectometer (SSR).

A ceramic tile (NBS standard #2019) and an aluminium mirror (NBS standard #2023) are used as the standard for diffused and specular reflectance, respectively. Fig. 2.3 shows the photograph of the Solar Spectrum Reflectometer (SSR). A ceramic tile is calibrated before measuring the absorptance of the tandem absorber. Once tandem absorber coating is placed on the sample port, tungsten halogen lamp provides the diffuse illumination at the measurement port. The radiation reflected from the sample placed was measured at an angle of 20° to the normal surface. SSR contains four detectors in different wavelength ranges: UV, blue, red and IR region. The relative response of each detector has been designed in a combination of light source to approximate the solar wavelength range. The accuracy of the measured α values is ±2%. The absorptance of the tandem absorber was measured in four different positions and values provided herein are average of four measurements (Barshilia et al., 2008).

2.4.3 UV-Vis-NIR and FTIR Spectrophotometry

The reflectance of the tandem absorber in the solar spectrum region was studied by using the UV-VIS-NIR spectrophotometer. It consists of light source, monochromator, chopper, sample compartment, reflecting mirrors and detector compartment. In the present work, Lambda 950, UV-VIS-NIR spectrophotometer (PerkinElmer) with integrating sphere and

universal reflectance accessories (URA) was used to measure the reflectance of the tandem absorber coating. A tungsten halogen lamp and a deuterium lamp were used to emit light in the wavelength of UV/Vis and NIR regions, respectively. The reflected radiation from the material can be either specular or diffused or a combination of both, depending on the roughness of the material surface. The total reflectance (i.e., specular and diffused) of the sample was measured using 150 mm integrating sphere accessory in the wavelength range of 250-2500 nm. The angular dependent absolute transverse magnetic (TM, known as 'p' polarization) and transverse electric (TE, known as '*s*' polarization) reflectance measurements were also carried out using UV-VIS-NIR spectrophotometer. The incident angles can be varied from 8 to 58° in the wavelength regime of 300-2500 nm, with an illumination spot size of 5 mm × 5 mm.

To measure the reflectance of the tandem absorber at different temperatures two different spectrophotometers were used in the UV to mid-IR range (0.25-25 μm). The PerkinElmer Lambda 950 spectrophotometer is equipped with deuterium and tungsten lamps, PMT and InGaAs detectors, and a 150 mm integrating sphere coated with spectralon diffuse reflective coating. The reflection spectrum of the sample was measured at an incidence angle of 8° with near-normal hemispherical (specular and diffuse). A SOC-100 HDR reflectometer (Surface Optics Corporation) coupled with a Nicolet FTIR 6700 in wavelength range of 1.25 to 25 μm spectrophotometer were used for hemispherical directional reflectance measurements $R^{\cap,\theta}$, at different detection angles θ from 10 to 70° in the wavelength regime of 1.25 μm to 25 μm. A gold coated calibrated specular reflectance standard was used as reference during the measurements (NIST calibration).

The FTIR is equipped with InGaAs and DTGS/KBr detectors, coupled with Quartz and KBr beam splitters, respectively, to cover the whole spectral range from 1.25 to 25 μm. The SOC-100 is equipped with a 2π imaging hemi-ellipsoid (gold coated) to illuminate the sample from all directions using a 700 °C (973 K) blackbody as the infrared source. A moveable overhead mirror collects the light reflected by the sample at a chosen detection angle, then directs the collimated beam into the FTIR apparatus for signal treatment to retrieve the reflectance spectrum (Soum-Glaude et al., 2017).

In order to study the thermal emittance of the tandem absorber at high temperatures, a heating plate also equips the SOC100 sample holder for measurements at different temperatures, from room temperature to 500 °C (773 K). The temperature of the sample was controlled by a surface thermocouple connected to PID regulation of the heating resistance. The overlapping of reflectance spectra from the two apparatus between 1.25 and 2 μm was systematically checked and the values given by the SOC-100 reflectometer with InGaAs detector were preferably considered in this range. For the calculation of solar absorptance and (hemispherical directional) thermal emittance of the samples, the measured reflectance spectra (0.25–25 μm) and the solar spectrum were linearly interpolated and extrapolated in the 0.25–30 μm range, with a step of 5 nm. The extrapolation allows for a better estimation of thermal emittance at 550 °C (823 K). Total optical properties (integrated over wavelength), i.e., solar absorptance α_s and (hemispherical directional) thermal emittance $\varepsilon_\theta(T)$ were calculated from directional spectral reflectance (Soum-Glaude et al., 2017).

2.4.4 Phase modulated ellipsometry

Ellipsometry is a non-destructive and contact less optical technique, which is widely used for the characterization of the thin and bulk films. In ellipsometry, the variation of the amplitude and the phase difference between the parallel (*p*) and the perpendicular (*s*) components of the reflected light polarized with respect to the plane of incidence are expressed in two terms of Psi (ψ) and delta (Δ) (Azzam et al., 1977).

$$\rho = \frac{r_p}{r_s} = \tan(\psi)e^{i\Delta} \quad (2.1)$$

where r_p and r_s are the reflection coefficients for the *p* and *s* components, respectively of the waves.

In this study, phase-modulated ellipsometery technique was used to overcome the drawback of slow acquisition data by conventional ellipsometry. In this technique, the reflected light is modulated with a frequency of 50 kHz and thus it offers fast and precise data acquisition by measuring signal over 200 ms.

The refractive index and extinction coefficient of the deposited tandem absorber in the wavelength regime of 300-1200 nm (Bhattacharyya et al., 2001, Bhattacharyya et al., 2002) were obtained by using a spectroscopic phase-modulated ellipsometry (Model UVISEL TM 460, ISA–JOBIN–YVON–SPEX). The obtained data from ellipsometry were fitted with theoretical data considering an appropriate dispersion formulae for the TiAlC, TiAlCN, TiAlSiCN, TiAlSiCO and TiAlSiO layers. In order to achieve more realistic results, the optical constants of stainless substrate were measured, and these data were used for ellipsometric data fitting (Palik et al., 1985).

Assuming the sample structure, void fractions, trial values for thickness and parameters of dispersion formula for the different layers as fitting parameters, the measured ellipsometric spectra were fitted by minimizing the squared difference (χ^2) between the measured and calculated values of the ellipsometric parameters (I_s and I_c) given by:

$$\chi^2 = [\frac{1}{2N-P}] \sum_I^N [(I_{Si}^{exp} - I_{Si}^{cal})^2 + (I_{Ci}^{exp} + I_{Ci}^{cal})^2] \quad (2.2)$$

where N is the number of points, P is the number of model parameters. The maximum number of iterations allowed is 100 and the criteria for convergence used was $\delta\chi^2 = 0.000001$.

2.4.5 X-ray diffraction

X-ray diffraction is a non-destructive analytical technique mainly used for identification and quantitative determination of the crystal structure of solids. In general, the X-rays are directed to the sample produce constructive interference, when it satisfies the Bragg's law (Cullity et al., 1956).

$$n\lambda = 2d\sin\theta \quad (2.3)$$

where λ is wavelength of the X- rays,

d is the distance between two lattice planes

θ is the angle between the incoming X- rays and the normal to the reflecting lattice plane

n is the integer called the order of the reflection.

In this work, XRD has been used to examine the structural properties of the as-deposited and heat treated tandem absorber using thin film X-ray diffraction (Model: D8

Advanced Bruker X-ray diffractometer). Cu K_α radiation was used as a source with an energy of 8.04 KeV and a wavelength of 0.154 nm. The designed tandem absorber and heat treated samples were analysed by rotating the sample and detector at a constant speed and scan over angles (2θ) from 20° to 70° with a glancing angle of 1°.

2.4.6 X-ray photoelectron spectroscopy

XPS is a surface analysis tool, which is mainly used to analysis the elemental composition, empirical formula and electronic state of the elements within the material (Heide et al., 2012). The composition and electronic state of the sample were studied by analysing the kinetic energy distribution of the emitted photoelectrons from the sample.

The bonding structure and chemical composition of each individual layers of the tandem absorber coating were studied using the X-ray photoelectron spectroscopy (SPECS) using non monochromatic Al K_α radiation (1486.6 eV) as an X-ray source operated at 150 W (12 kV, 12.5 mA). The binding energies reported here were referenced with C1s peak at 284.6 eV. All spectra were recorded with a pass energy and step increment of 40 and 0.05 eV, respectively. For XPS analysis, sample was mounted on the sample holder and placed into a load–lock chamber with an ultrahigh vacuum of 8.0×10^{-8} mbar for 5 h in order to desorb any volatile species present on the surface. After 5 h, the sample was transferred into the analyzing chamber with UHV of 5×10^{-10} mbar.

2.4.7 Field emission scanning electron microscopy and EDAX

FESEM provides topographical information of the sample with higher magnification of 10x-300,000x (resolution = 1.0 nm). It offers the images with spatial resolution with 3-6 times better than the conventional SEM. A tungsten with sharp pointed end is used as a field emitter source. Generally, the acceleration voltage between the anode and the cathode is 0.5 to 30 KV with a vacuum of 10^{-6} Pa in the column of microscope. When the electron interacts with the sample and produces secondary electrons, back scattered electrons and X-rays. Secondary electrons are most widely used for imaging and give topographic information with excellent resolution (Goldstein et al., 2003). The topographical information was obtained by back scattered electrons. X rays are formed due to the displacement of inner shell electron by the primary electron and have been used for

the compositional characterizations. Field-emission scanning electron microscopy (CarlZeiss, SUPRA 40VP) was used to study the thickness of the each individual layer of the tandem absorber deposited on the silicon substrate and also the surface morphology.

The elemental composition of each individual layers of the deposited tandem absorber was analysed by using EDS (Oxford), which is a simple and powerful technique. EDS is attached to the FESEM, which detects the X-rays produced by a sample placed in an electron beam and automatically identifies the elemental composition of the materials with a sensitivity of >0.1% for elements heavier than boron.

2.4.8 AFM and 3D profilometer

AFM is a powerful microscopy technique because of its high atomic resolution along with angstrom scale resolution height information of the topographical images. It uses a cantilever with sharp tip to scan over a sample surface. The interaction between the probe and sample surface gives the topographical image of the sample. The difference between the raised and lowered portion of the sample surface causes the deflection of the cantilever and the changes in the cantilever are monitored by position sensitive photodiode (Peterman et al., 2011).

In this work, the RMS surface roughness (R_a) values of the individual layers of the tandem absorber and annealed tandem absorber samples were studied by using AFM manufactured by Antonparr Instruments with tip size of 10 nm. 3D profilometer developed by Nanomap 500LS (AEP Technologies) with a tip size of 100-150 nm, was also used for measuring the R_a and thickness of each individual layers of the deposited tandem absorber.

2.4.9 Transmission electron microscopy (TEM)

TEM is a powerful microscopy technique. It utilizes the high energetic electrons accelerated through a potential of 40 -200 kV, to study the morphology, composition and crystallographic nature the sample. It produces the high resolution two-dimensional images with a maximum resolution of < 1 nm. An image is formed from the interaction of the electron transmitted through the specimen. Imaging devices such as CCD camera, fluorescent screen and a photographic films are used for magnifying and focussing the image (Williams et al., 2009).

The Transmission electron microscopy studies on the designed tandem absorber was performed using a TECNAI 20UT high-resolution electron micro-scope (HRTEM). The microscope was operated at 200 kV. The quality of the TEM analysis depends on the sample preparation method. The preparation of the sample process for TEM is tedious and challenging process. In the present study, the deposited tandem absorber were transferred onto a Cu grid. The samples were prepared by the standard sample preparation technique as described in the literature (Sridhara et al., 2010).

2.4.10 Resistivity Measurements

The resistivity measurements of the individual layers of the tandem absorber were carried out using a two probe method (Keithley DC and AC Constant Current Source Meter, Model 6221). For this, 200 nm thick coatings of individual layers were prepared on glass substrates to avoid the contribution of substrate on the resistivity measurements.

2.4.11 Adhesion test

A standard test method ASTM 3359-07 was used to study the adhesion between the deposited tandem absorber to the stainless steel substrate. The Adhesion test was studied by tape peel off method. 3 M scotch$^{®}$ tape was used to perform the adhesion test. Deposited samples were fixed on a flat surface, a piece of tape is bonded to the deposited tandem absorber sample and peel backwards at a 180° angle. The same process was repeated for multiple times.

2.4.12 Scout Software

SCOUT software (SCOUT_98) was used for the analysis of optical spectra by comparison of measurements and models. The following quantities were simulated: reflectance, transmittance, absorbance, ATR, and ellipsometry parameters (ψ, Δ), etc., In SCOUT data, the agreement between the simulated and measured spectra was studied by the fit deviation value. If the fit deviation values are less than 0.1, 0.01, 0.001, 0.0001 and 0.00001, it indicate the fit as rejected, bad, acceptable, good and excellent, respectively (Theiss et al., 2017).

In this work, Scout software was utilized to simulate the reflectance spectra of each individual layer of the tandem absorber. The agreement between the simulated and the experimental data was studied by the fit deviation value.

Chapter   3

Design and Fabrication of Spectrally Selective TiAlC/TiAlCN/TiAlSiCN/TiAlSiCO/TiAlSiO Tandem Absorber for High-Temperature Solar Thermal Power Applications

In this Chapter, design and fabrication of the TiAlC/TiAlCN/TiAlSiCN/TiAlSiCO /TiAlSiO tandem absorber are discussed. Importance of incorporating each layer on absorptance and emittance of the coating is analyzed in detail. Performance of the tandem absorber at different temperatures for short duration is also studied.

3.1   INTRODUCTION

In general, for high temperature applications materials such as: borides, carbides, oxides, nitrides and silicides having very high melting points, high hardness, improved wear resistance, high corrosion and oxidation resistance are used. These materials may also be used for photothermal conversion provided their composition and optical properties are engineered suitably. Several high temperature stable absorber coatings have been reported in the recent literature. Liu et al. studied a new solar spectral coating on stainless steel substrate (Fe_3O_4/Mo/TiZrN/TiZrON/SiON), which is stable at 500°C for 300 h in vacuum (Liu et al., 2014). Du et al. studied the $Ti_{0.5}Al_{0.5}N$/$Ti_{0.25}Al_{0.75}N$/AlN absorber coating and the optimized coating exhibited an absorptance of 0.945 and emittance of 0.04 (Du et al., 2011). Valleti et al. developed a solar selective functional multilayered Cu/TiAlCrN/TiAlN/AlSiN with an absorptance of 0.91 and an emittance of 0.07 with high thermal stability (Valleti et al., 2014). There are several other reports on the fabrication of high temperature solar absorber coatings based on nitrides and oxy-nitrides/oxides of various transition metals (Feng et al., 2015; Gong et al., 2015; Liu et al., 2014; Wu et al., 2015). In addition to these works, over the years, Barshilia et al. have also developed a

large number of tandem absorber and multilayer absorber coatings for high temperature solar thermal applications (Barshilia et al., 2007; Barshilia et al., 2008; Biswas et al., 2008; Selvakumar et al., 2010, 2012, 2015; Barshilia, 2014).

Transition metal carbides and carbonitrides are majorly used for various industrial applications due to their unique properties such as high hardness, chemical stability, high melting temperature and better resistance to oxidation (Kosolapova, 1971 and Toth, 1971). It might be possible to achieve selective properties in these materials by adjusting their composition by controlling carbon and nitrogen contents as well as thicknesses during the sputtering. Lately, some attempts have been made to use these materials for photothermal conversion applications (Soum-Glaude et al., 2013; Fang et al., 2015). However, a great deal of research is required to achieve spectrally selective coatings with high thermal stability consisting of carbides/carbonitrides/oxides thin films. In the present work, have been chosen a combination of carbides, carbonitrides and oxides of titanium, aluminum and silicon for designing and fabricating a spectrally selective coating with very high thermal stability.

3.2 EXPERIMENTAL PROCEDURE

The coatings were deposited on stainless steel substrates (dimensions 35 mm $\times$ 35 mm $\times$ 2 mm) by a Four-Cathode Reactive Unbalanced Direct Current (DC) Magnetron Sputtering System with 6″ diameter targets. Before loading the substrates into the vacuum chamber, they were ground and metallographically polished to get the smooth surface and the substrates were ultrasonically cleaned in an isopropyl alcohol and acetone to remove grease and dust particles on the surface of the substrate. The samples were loaded in the vacuum chamber and pumped down the vacuum chamber up to a base pressure of 8.0×10^{-4} Pa. High purity titanium (2 Nos.), aluminum (1 No.) and silicon (1 No.) targets (purity >99.9%) were used for the deposition. The substrate to target distance was 10 cm. The substrates were cleaned by *in situ* argon ion bombardment for 15 min, wherein a DC bias (V_B) of -1000 V was applied to the substrate. Four pulsed DC power supplies were used to deposit TiAlC, TiAlCN, TiAlSiCN, TiAlSiCO and TiAlSiO layers by the reactive

sputtering of Ti, Al, Si metal targets in Ar, N_2, C_2H_2 and O_2 environment under the required composition and operating pressure (1.86 Pa).

S. No.	Stack description [Optimized thickness]	Optimized parameters
1	Layer 1 (TiAlC) [62 nm]	Ar: 28 sccm ; C_2H_2: 2 sccm V_B: -100 V Ti Target power density: 1.126 W/cm^2 Al Target power density: 1.314 W/cm^2 Deposition time : 3 min 21 sec
2	Layer 2 (TiAlCN) [20 nm]	Ar: 28 sccm; C_2H_2: 3 sccm; N_2: 8 sccm V_B: -100 V Ti Target power density : 1.126 W/cm^2 Al Target power density: 1.689 W/cm^2 Deposition time: 3 min 10 sec
3	Layer 3 (TiAlSiCN) [18 nm]	Ar: 28 sccm; C_2H_2: 1.5 sccm; N_2: 10 sccm V_B: -100 V Ti Target power density: 1.126 W/cm^2 Al Target power density: 1.126 W/cm^2 Si Target power density: 0.563 W/cm^2 Deposition time: 4 min 30 sec
4	Layer 4 (TiAlSiCO) [16 nm]	Ar: 28 sccm; C_2H_2: 1.5 sccm; O_2: 5 sccm V_B: -100 V Ti Target power: 1.126 W/cm^2 Al Target power: 1.407 W/cm^2 Si Target power: 1.032 W/cm^2 Deposition time: 5 min
5	Layer 5 (TiAlSiO) [27 nm]	Ar: 18 sccm; O_2: 12 sccm; V_B: 0 V Ti Target power: 1.877 W/cm^2 Al Target power: 2.252 W/cm^2 Si Target power: 1.314 W/cm^2 Deposition time: 7 min 30 sec

Table 3.1: Optimized process parameters used for the preparation of the solar selective coating.

All the coatings were deposited at a substrate temperature of 300°C. The optimized process parameters for the deposition of tandem absorber are listed in Table. 3.1. A W interlayer of ~800 nm was deposited separately to reduce the emittance of the SS substrate.

3.3   RESULTS AND DISCUSSION

3.3.1   Design of the tandem absorber

The design of the tandem absorber, which consists of three absorber layers, a semi-transparent layer and an anti-reflection layer, is shown schematically in Fig. 3.1(a). Layers 1-5 represent TiAlC, TiAlCN, TiAlSiCN, TiAlSiCO and TiAlSiO, respectively. In order to achieve the high absorptance of the tandem absorber, the absorber layer was designed consisting of three layers (namely, TiAlC, TiAlCN, TiAlSiCN) with varying metal volume fractions. For example, the TiAlC layer was more metallic as compared to TiAlSiCN layer. This was confirmed by measuring the resistivity of the individual layers deposited on glass substrates with a thickness ~200 nm. Fig. 3.1(b) shows the resistivity values of individual layers of the tandem absorber. It is apparent from the figure that the resistivity of the each individual layer increases from first layer (i.e., $\rho_{TiAlC} = 5 \times 10^{-4}$ Ωcm) to the last layer (i.e., $\rho_{TiAlSiO} = 3.4 \times 10^4$ Ωcm). An increase in the resistivity means a decrease in the electrical conductivity. This result clearly indicates that metal volume fraction decreases from bottom (TiAlC) to top layer (TiAlSiO).
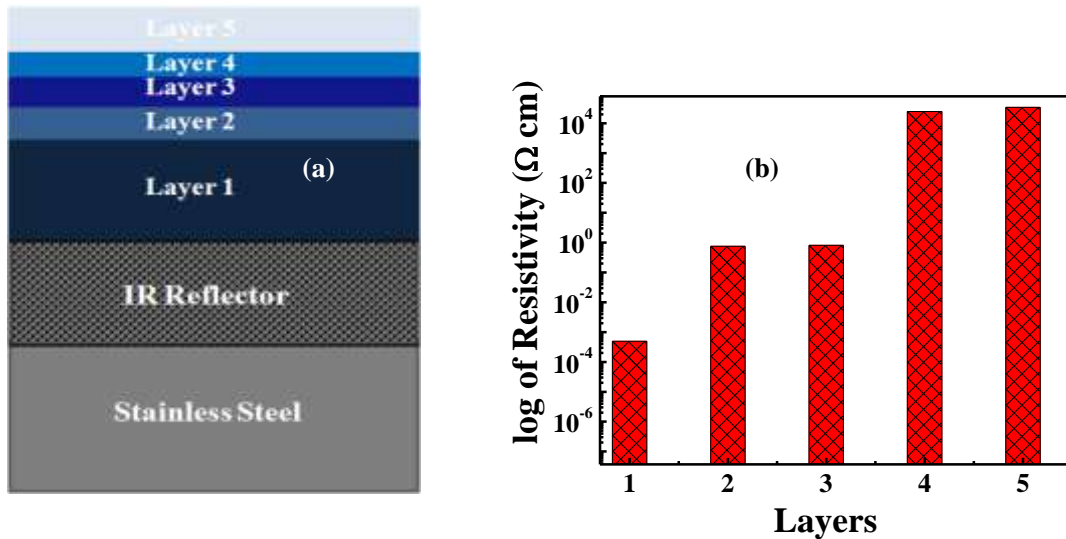
Figure 3.1: (a) Schematic representation of the tandem absorber. (b) Resistivity of various individual layers of the tandem absorber.

The tandem absorber designed in this manner exhibited a gradient refractive index (i.e., the refractive index of the bottom layer was highest and that of the top layer was lowest) (Barshilia et al., 2006). Table. 3.2 depicts the absorptance and the emittance values of the successive layers deposited on stainless steel substrate. The optimized tandem absorber deposited on stainless steel substrate shows high absorptance of 0.961 and emittance of 0.15. For solar thermal high temperature applications it is necessary to reduce the thermal emittance of the tandem absorber deposited on stainless steel substrate. This was achieved by incorporating an infrared reflector layer of tungsten with a thickness of ~800 nm (Sibin et al., 2015). With this infrared reflector layer the emittance of the tandem absorber could be reduced to 0.07.

Stack description	Absorptance	Emittance (82°C)
SS	0.387-0.380	0.12-0.13
SS/TiAlC	0.761	0.11
SS/TiAlC/TiAlCN	0.803	0.11
SS/TiAlC/TiAlCN/TiAlSiCN	0.882	0.13
SS/TiAlC/TiAlCN/TiAlSiCN/TiAlSiCO	0.912	0.14
SS/TiAlC/TiAlCN/TiAlSiCN/TiAlSiCO/ TiAlSiO	0.960	0.15
SS/W/TiAlC/TiAlCN/TiAlSiCN/TiAlSiCO/ TiAlSiO	0.960	0.07

Table 3.2: The absorptance and emittance values of individual layers of the tandem absorber coating deposited on stainless steel substrate.

3.3.2 Cross-sectional TEM and AFM analysis of the deposited tandem absorber

Fig. 3.2(a) shows a typical bright field XTEM image of the tandem absorber deposited on silicon substrate displaying a total thickness of 150 nm. Fig. 3.2(b) shows the 3-D AFM
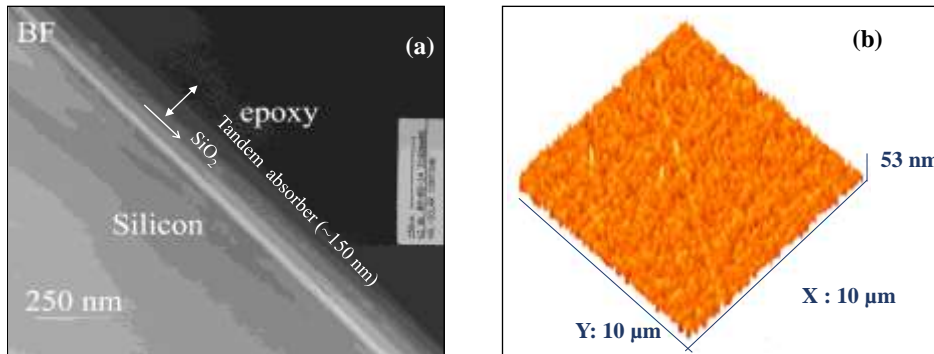
Figure 3.2: (a) Cross-sectional TEM micrograph. (b) Shows the AFM data of the tandem absorber.

image of the optimized tandem absorber deposited on SS substrate. These absorbers indicated an RMS roughness of ~3.5 nm.

3.3.3 Optical properties of each individual layer of the designed tandem absorber

With a view to understand the role of various layers of the tandem absorber, detailed reflectance studies were carried out using the UV-VIS-NIR spectrophotometer and the data is shown in Fig. 3.3(a). The total reflectance of the fabricated tandem absorber exhibits low reflectance in the visible region and high reflectance in the near infrared region. The reflectance spectra of single layer TiAlC and double layer TiAlC/TiAlCN show only one reflectance minimum (R_{min}) at λ = 613 nm and 653 nm, respectively, due to destructive interference and then reflectance increases with wavelength (Fig. 3.2(a)). In case of three layers (TiAlC/TiAlCN/TiAlSiCN), four layers (TiAlC/TiAlCN/TiAlSiCN/TiAlSiCO) and five layers (TiAlC/TiAlCN/TiAlSiCN/TiAlSiCO/TiAlSiO) tandem absorbers, two reflectance minima are observed due to destructive interference at 306 nm (2nd), 685 nm (1st), 317 nm (2nd), 710 nm (1st), 495 nm (2nd) and 810 nm (1st), respectively (Zhao et al., 2006). The tandem absorber maintains low reflectance for wavelength <1500 nm and there after the reflectance increases with wavelength. As shown in Fig. 3.3(b) the 1st reflectance minimum of the each successive layer shifts to higher wavelength. This clearly indicates that the metallic nature decreases with an increase in dielectric nature from the first layer

41

to the last layer, which leads to gradient refractive index of the tandem absorber (Barshilia et al., 2006; Zhao et al., 2006, Heavens, 1965). This data also shows that the overall reflectance in the UV-VIS-NIR was reduced by introducing each individual layers to the tandem absorber. This reduction in reflectance directly shows the increase of absorptance by incorporating each layer to the tandem absorber as confirmed independently by solar reflectometer measurements, the data of which are displayed in Table. 3.2.

In order to improve the performance of the tandem absorber, one needs to achieve low thermal emittance. Especially for solar thermal high temperature applications, the operating temperature is generally $> 450°C$. Accordingly, the re-radiation losses in the IR region will be at $\lambda > 3$ µm as per Wien's displacement law.

Therefore, the tandem absorber should have high reflectance in the IR region. The reflectance spectra of the successive layers of the tandem absorber were studied in the IR region using FTIR spectrometer.
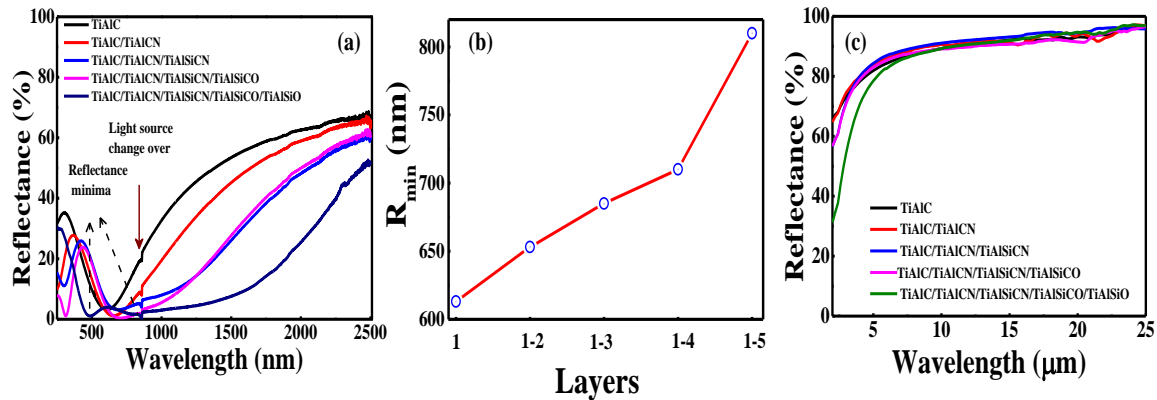
Figure 3.3: (a) Reflectance spectra of successive layers of the tandem absorber deposited on stainless steel substrate. (b) Indicates the position of reflectance minimum for successive layers. (c) FTIR spectra of the successive layers of the tandem absorber deposited on SS substrate.

Each successive layer of the tandem absorber deposited on stainless steel substrate exhibits high reflectance in IR region, the corresponding data is shown in Fig. 3.3(c). The

reflectance of the all individual layers of the tandem absorber shows almost 96% at $\lambda = 25$ μm. The overall reflectance values of the four layers and five layers of the tandem absorber are lower than reflectance values of single, double and three layers. Due to this reason the emittance of the tandem absorber increases from first layer to the last layer as shown in Table 3.2.

3.3.4 Color measurement studies of the tandem absorber

The obtained reflectance spectrum of each individual layer of the tandem absorber was used to study the colorimetry (International Commission on Illumination (CIE) color coordinates). The detailed effect of individual layer's reflectance spectrum of tandem absorber on color of the coating is shown in CIE chromaticity diagram (Fig. 3.4). Almost all the layers are almost blue in color, which represents the reflection of shorter wavelength. TiAlC layer shows a pale blue color (Fig. 3.4(a)), which indicates that the coating is not only reflecting the shorter wavelengths but also the longer wavelengths. Due to this reason the coating shows the absorptance of 0.762. The coating color improved from pale blue to darker pale blue by incorporating the second layer (TiAlCN) to the first layer (TiAlC) (Fig. 3.4(b)), which leads an increase in absorptance from 0.762 to 0.827. Further, by adding the third (TiAlSiCN) and the fourth layer (TiAlSiCO) to the tandem absorber, the sample turns to blue color and the absorptance of the coating increases to 0.912 (Fig. 3.4(c, d)). After depositing the anti-reflection layer to the tandem absorber the sample exhibits a dark blue color (Fig. 3.4(e)). This five layer coating exhibits the highest absorptance of 0.961. Overall, reflectance of the tandem absorber reduces by incorporating each layer, which directly enhances the color of the coating from pale blue color to blue color. This data confirms that the color of the coating is directly related to the reflectance spectrum of each layer and directly affects the selective properties of the tandem absorber (Atasi et al., 2016).
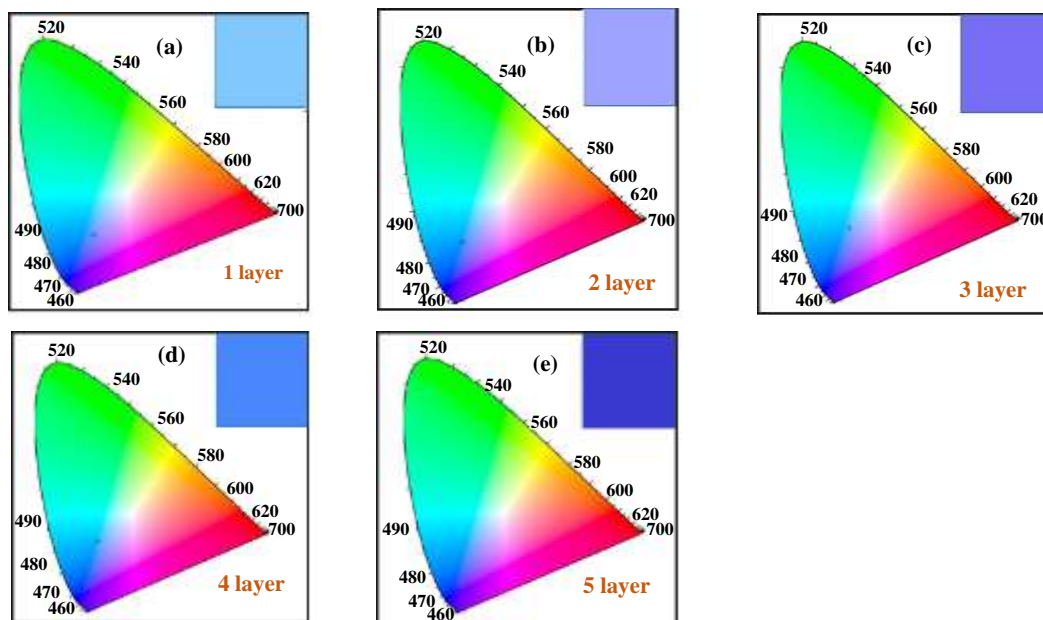
Figure 3.4: The chromaticity diagram of individual layers of the tandem absorber. Insets are the color appearances of the coating: (a) TiAlC (b) TiAlCN (C) TiAlSiCN (d) TiAlSiCO and (e) TiAlSiO.

3.3.5 Compositional and structural analysis of the tandem absorber

Fig. 3.5(a) shows the XRD data, recorded in thin film mode, of different layers (TiAlC, TiAlCN, TiAlSiCN, TiAlSiCO and TiAlSiO) of tandem absorber deposited for 2 h on stainless steel substrate along with the XRD pattern of SS substrate (reflections marked as '*'). The thicknesses of TiAlC, TiAlCN, TiAlSiCN, TiAlSiCO and TiAlSiO layers were 2.2 μm, 755 nm, 491 nm, 393 nm and 431 nm. The X-ray diffraction of the first absorber layer TiAlC shows a high intensity peak centered at $2\theta = 37.9°$, which corresponds to the (111) plane of cubic phase Ti_3AlC (*JCPDS*). Even though TiAlC exits in different phases (viz., Ti_2AlC, Ti_3AlC_2, Ti_4AlC_3, the MAX-phases), the only ternary phase formed at low substrate temperature (i.e., 300°C) is Ti_3AlC and cubic (TiAl)C (Wilhelmsson et al., 2006). The XRD of the second absorber layer (i.e., TiAlCN) shows a peak centered at $2\theta = 38.9°$, which corresponds to TiAlCN (111) (*JCPDS*). Incorporation of nitrogen into the TiAlC causes the peak to shift to higher angles. This suggests that partial carbon atoms were

replaced by nitrogen atoms (*JCPDS*). As for the second absorber layer, the aluminum target power used was higher (450 W) as compared to the first layer (300 W) the occurrence of AlCN (01 11) phase was observed and a low intensity peak of TiCN (220) was also observed (*JCPDS*). The XRD of TiAlSiCN layer shows a peak centered at $2\theta = 42.4°$, which corresponds to the formation of TiCN (200) along with the appearance of TiCN (200) reflection. The peak at $2\theta = 36.6°$ is assigned as AlCN (01 11) (*JCPDS*). For this layer, the X-ray data did not show any peak corresponding to either SiC or Si_3N_4 phases, indicating their amorphous nature. For the case of TiAlSiCO layer a very weak peak centered at $2\theta = 36.2°$ was observed, which is assigned to nano-crystalline TiO_2 (101) phase (*JCPDS*). As no other peaks pertaining to Al_2O_3, SiO_2, TiC or SiC were observed in the XRD data, this layer is believed to be a nanocomposite consisting of TiO_2 and
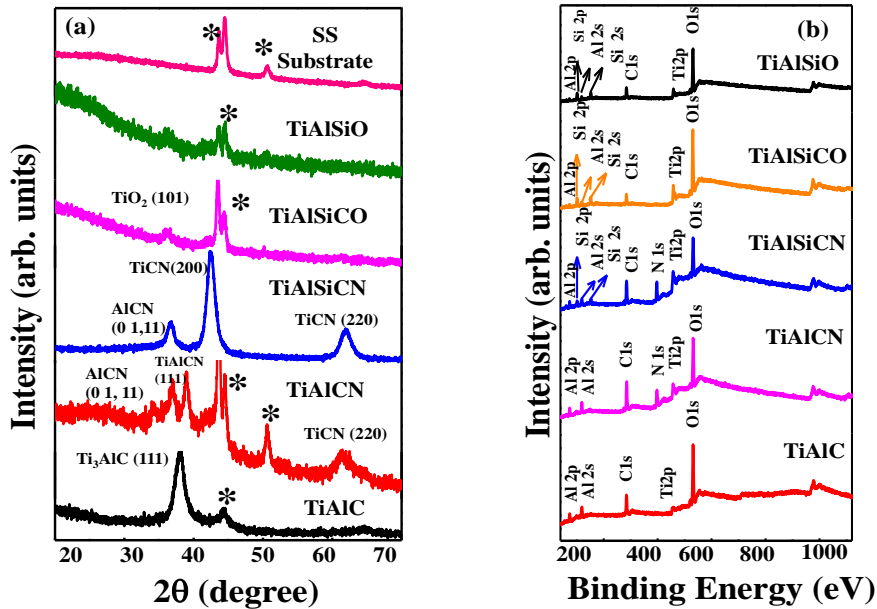
Figure 3.5(a) XRD diffraction patterns of TiAlC, TiAlCN, TiAlSiCN, TiAlSiCO, TiAlSiO layers deposited on stainless steel substrate for 2 h. Also shown is the XRD pattern of stainless steel substrate. (b) Survey level XPS spectra of TiAlC, TiAlCN, TiAlSiCN, TiAlSiCO, TiAlSiO layers.

amorphous phases of these compounds. Finally, for the anti-reflection layer (i.e., TiAlSiO) as the oxygen flow rate was 12 sccm (cf., 5 sccm for TiAlSiCO layer) no reflections in the XRD data were observed, indicating its X-ray amorphous nature.

To study the chemical composition and chemical state of various elements of the tandem absorber, individual layers were characterized by XPS. Fig. 3.5(b) shows the survey scan spectra of different layers of the tandem absorber deposited on silicon substrates, indicating the presence of various elements, as expected. The XPS data was further analyzed by recording the core-level spectra of all the layers. Typical core level spectra of various elements present in TiAlC layer are presented in Fig. 3.6. The carbon core level spectrum consists of three peaks centered at the binding energies of 282.6, 284.6 and 288.4 eV after deconvolution. The high intensity peak centered at 284.6 eV indicates carbon contamination in the film. The low intensity peaks centered at 282.6 and 288.4 eV correspond to Ti-C and C=O (Zhang et al., 1998; Wilhelmsson et al., 2006). The Al core level spectrum revealed the presence of Al-C and Al peaks centered at 74.8 and 72.6 eV, respectively. The Ti 2p core level spectrum could be resolved into four peaks centered at 454.6, 458.8, 460.4 and 464.8 eV. The peaks at 454.6 and 460.4 eV originate from $Ti2p_{3/2}$ and $Ti2p_{1/2}$ electrons in titanium carbide, respectively, while the peaks at 458.8 and 464.6 eV originate from $Ti2p_{3/2}$ and $Ti2p_{1/2}$ electrons in titanium oxide, respectively (Zhang et al., 1998; Wilhelmsson et al., 2006). This implies that carbon is attached to titanium. The oxygen attached to titanium may be due to presence of oxygen in the vacuum chamber.
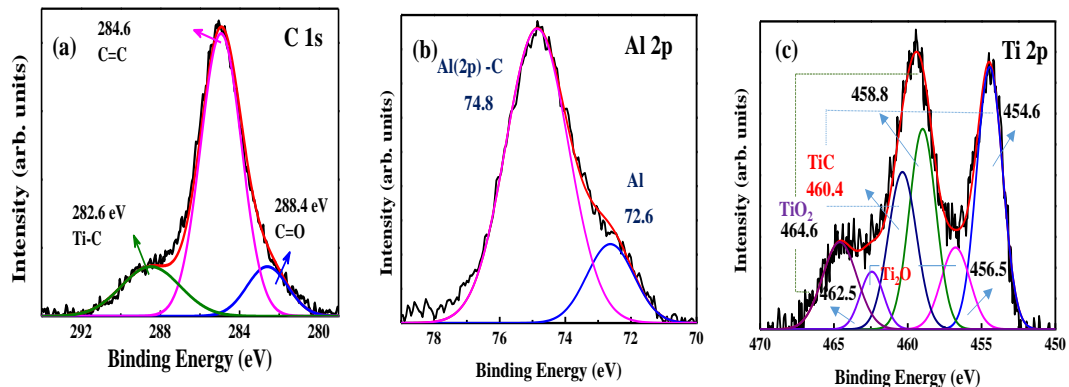
Figure 3.6. XPS core level spectra of the TiAlC layer: (a) C1s, (b) Al2p and (c) Ti2p.

46

The oxygen impurity is attributed to low vacuum and contamination in the chamber. The XPS core level spectra of different elements of the TiAlCN layer are shown in Fig. 3.7. Curve fitted Ti2p core level spectrum shows the Ti2p$_{3/2,½}$ peaks at 456.5, 458.5, 462.1 and 464.2 eV, indicating the presence of TiN and TiO$_2$ (Fig. 3.7(a)) (Restrepo et al., 2010, Gao et al., 2003). The aluminum core spectrum shows the peak centered at 74.1 and 75.4 eV corresponds to Al$_2$O$_3$ and AlO$_x$, respectively (Fig. 3.7(b)) (Beng et al., 1991; Chang et al., 1996). Nitrogen and carbon XPS core level spectra are shown in (Fig. 3.7(c) and (d)). The presence of AlN and TiN was further confirmed by deconvolution the nitrogen core level spectrum with the binding energy values of 396.9 and 399.2 eV (Restrepo et al., 2010). The carbon core level spectrum shows peaks at 284.6, 285.8 and 288.3 eV, which are attributed to C=C, C-C and C=O, respectively (Antonucci et al., 1994; Maksym et al., 2007).
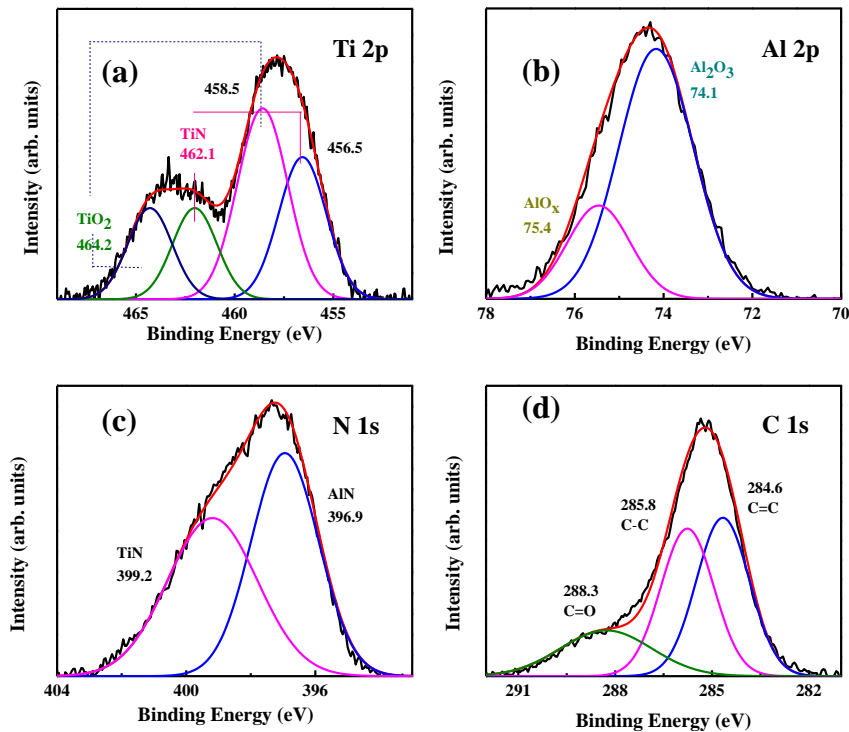
Figure 3.7. XPS core level spectra of the TiAlCN layer: (a) Ti2p, (b) Al2p (c) N1s and (d) C1s.

Fig. 3.8 shows the core level XPS spectra of a TiAlSiCN layer. Ti2p reveals the peaks at 456.5, 458.8, 462.2 and 464.2 eV, which originate from TiN and TiO_2 (Fig. 3.8(a)) (Restrepo et al., 2010, Gao et al., 2003). The fitted aluminum core spectrum shows the high intensity peak of Al_2O_3 with a low intensity of AlO_x with a binding energies of 74.1 and 75.3 eV, respectively. (Fig. 3.8(b)) (Beng et al., 1991; Chang et al., 1996). The deconvolution of N1s spectrum shown in Fig. 3.8(c) resulted in three peaks centered at 396.4, 397.6 and 399.5 eV, which belongs to AlN, Si_3N_4 and TiN, respectively (Restrepo et al., 2010). The nitrogen spectrum completely reveals the formation of nitrides of Ti, Al and Si. The silicon core level spectrum shows a broad peak, which is deconvoluted into two peaks at 101.2 and 102.3 eV, corresponding to SiC_XO_Y and SiO_x, respectively (Fig. 3.8(d)). The peak at 101.2 is due to intermediate state between the SiC and SiO_2 (Cao et al., 2016). Finally, the C1s spectrum shows three peaks at 284.6, 285.6 and 288.4 eV, which correspond to C=C, C-C and C=O, respectively (Fig. 3.8(e)) (Antonucci et al., 1994; Maksym et al., 2007).
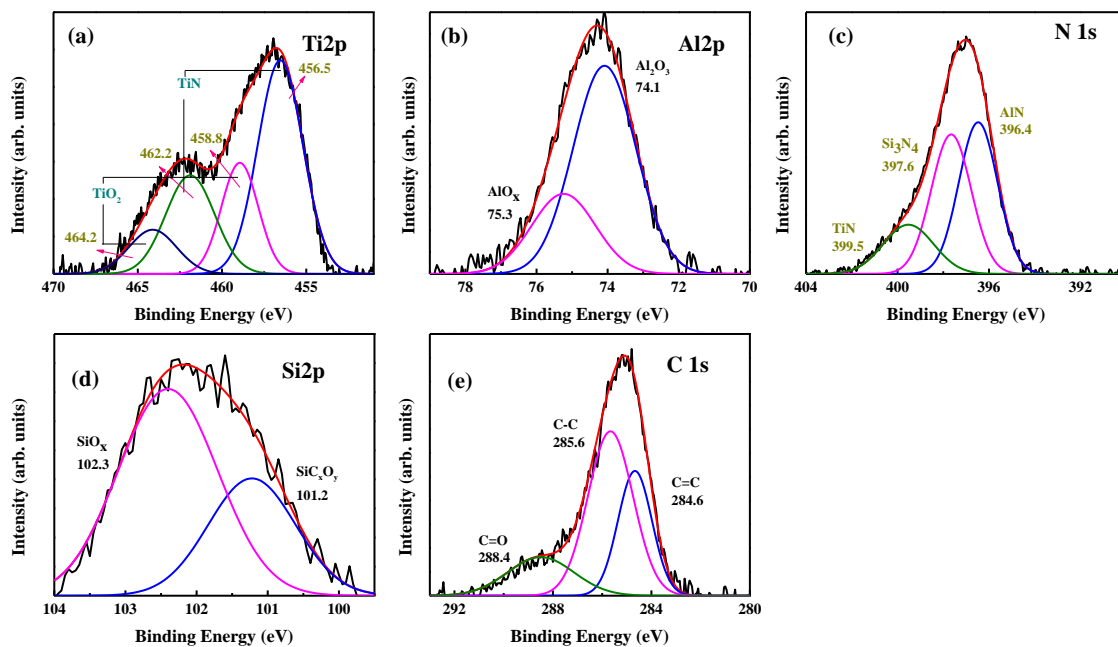
Figure 3.8: XPS core level spectra of TiAlSiCN layer: (a) Ti2p, (b) Al2p (c) N1s (d) Si2p and (e) C1s.

Fig. 3.9 shows the XPS core level spectra of TiAlSiCO layer. The titanium XPS spectrum shows $Ti2p_{3/2,1/2}$ core level peaks at 458.7 and 464.3 eV, which correspond to TiO_2 (Fig. 3.9(a)) (Gao et al., 2003). The presence of AlO_x and Al_2O_3 in the layer was confirmed by aluminum core level spectrum (Fig. 3.9(b)) (Beng et al., 1991; Chang et al., 1996). Fig. 3.9(c), silicon core level spectrum shows two high intensity peaks with one very low intensity peak at 99.6, 101.2 and 102.3 eV such as Si-Si, SiC_xO_y and SiO_x, respectively (Cao et al. 2016; Sirotti et al., 1993). Oxygen and carbon core level spectra show one strong and weak intensity peak. The high intense peak at 530.6 eV attributes to Al_2O_3, whereas one weak peak at 532.3 eV is associated to SiO_x (Fig. 3.9(d)). The high intense peak of C1s shows at 284.6 and 288.1 eV relates to carbon contamination as C=C and C=O, respectively (Fig. 3.9 (e)) (Antonucci et al., 1994; Maksym et al., 2007).
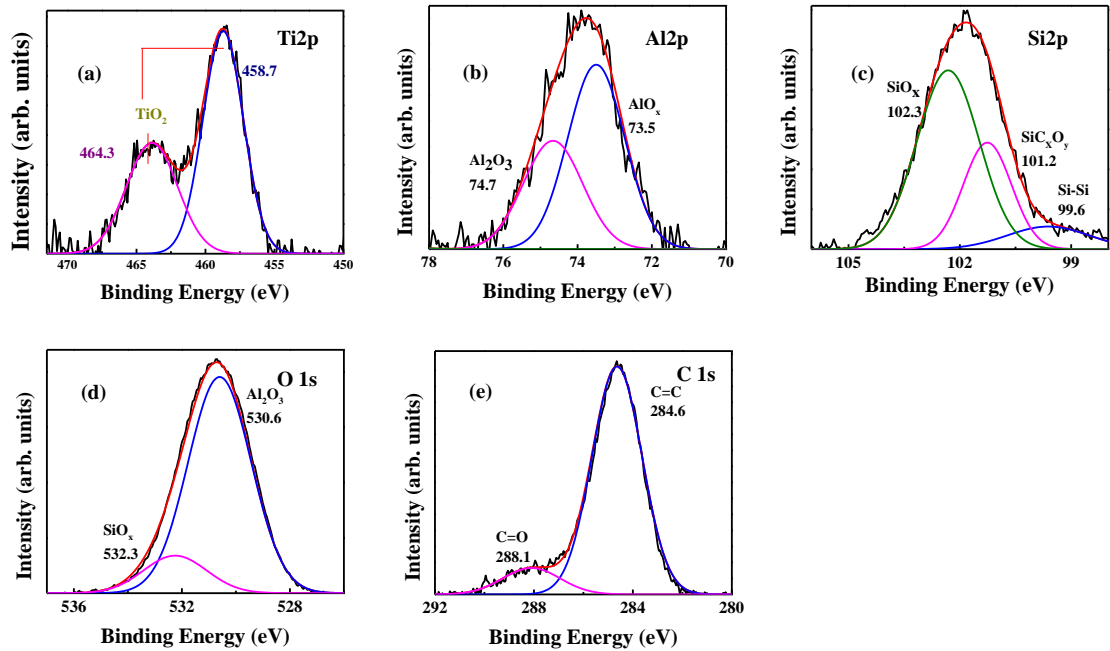
Figure 3.9: XPS core level spectra of the TiAlSiCO layer: (a) Ti2p, (b) Al2p (c) Si2p (d) O1s (e) C1s.

The presence of oxide formation in the anti-reflection layer (TiAlSiO) was studied by the core level XPS spectra, the data of which is shown in Fig. 3.10. The core level spectrum

of the Ti2p shows the couple of peaks centered at 458.8 and 464.3 eV corresponding to Ti2p$_{3/2}$ and Ti2p$_{1/2}$ of TiO$_2$ (Gao et al., 2003). The core level spectrum of Al2p shows the formation of AlO$_x$ and Al$_2$O$_3$ in the layer (Beng et al., 1991; Chang et al., 1996). The Si2p core level spectrum show the formation of SiO$_x$ with high intensity peak at 102.1 eV along with a weak peak at 99.5 eV, which originates from Si-Si (Morgan et al., 1992). The oxygen spectrum further confirms the formation of Al$_2$O$_3$ and SiO$_2$ with peaks corresponding to 530.8 and 532.3 eV, respectively (Sirotti et al., 1993, Dorninique et al., 1994). Table. 3.3 shows the summary of XPS peaks assignment of each individual layer of the tandem absorber. In conclusion, the XPS data corroborates the XRD data and also confirms the presence of elements in the respective layers. Further, the XPS data reveals the surface contamination along with the presence of dominant phases in the layers.
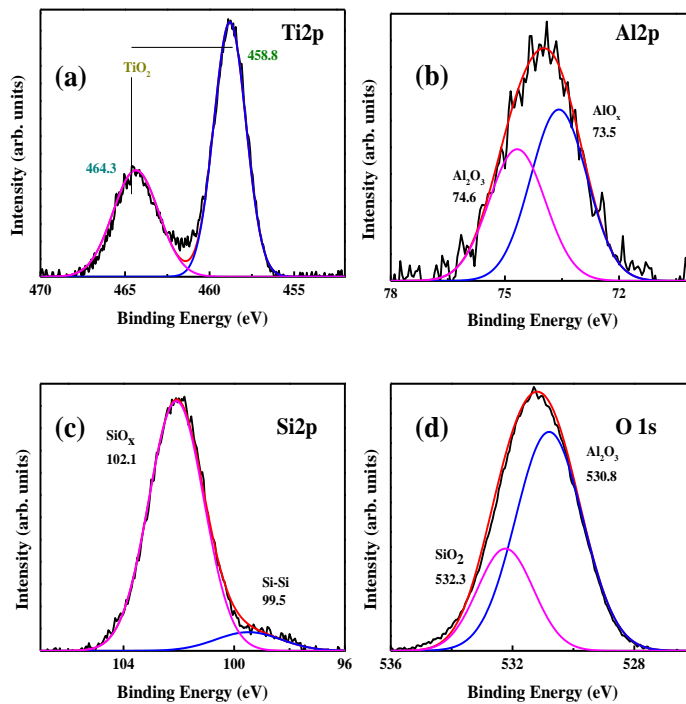
Figure 3.10: XPS core level spectra of the TiAlSiO layer: (a) Ti2p, (b) Al2p (c) Si2p (d) O1s.

Layer	Element	Binding Energy (eV)	Spectral line	Chemical bonding
TiAlC	Ti	454.6	$2p_{3/2}$	Ti-C
		456.5	$2p_{3/2}$	Ti_2O
		458.8	$2p_{3/2}$	TiO_2
		460.4	$2p_{1/2}$	Ti-C
		462.5	$2p_{1/2}$	Ti_2O
		464.6	$2p_{1/2}$	TiO_2
	Al	72.6	$2p$	Al
		74.3	$2p$	Al-C
	C	282.6	$1s$	C=C
		284.9	$1s$	Ti-C
		288.4	$1s$	C=O
TiAlCN	Ti	456.5	$2p_{3/2}$	Ti-N
		458.5	$2p_{3/2}$	$Ti-O_2$
		462.1	$2p_{1/2}$	Ti-N
		464.2	$2p_{1/2}$	TiO_2
	Al	74.1	$2p$	Al_2O_3
		75.4	$2p$	AlO_x
	N	399.2	$1s$	Ti-N
		396.9	$1s$	Al-N
	C	284.6	$1s$	C=C
		285.8	$1s$	C-C
		288.3	$1s$	C=O

TiAlSiCN	Ti	456.5	$2p_{3/2}$	Ti-N
		458.8	$2p_{3/2}$	TiO_2
		462.2	$2p_{1/2}$	Ti-N
		464.2	$2p_{1/2}$	TiO_2
	Al	74.1	$2p$	Al_2O_3
		75.3	$2p$	AlO_x
	Si	101.2	$2p$	SiC_XO_Y
		102.3	$2p$	SiO_x
	N	396.4	$1s$	Al-N
		397.6	$1s$	Si_3N_4
		399.5	$1s$	Ti-N
	C	284.6	$1s$	C=C
		285.6	$1s$	C-C
		288.4	$1s$	C=O
TiAlSiCO	Ti	458.7	$2p_{3/2}$	TiO_2
		464.3	$2p_{1/2}$	TiO_2
	Al	73.5	$2p$	AlO_x
		74.7	$2p$	Al_2O_3
	Si	99.6	$2p$	Si-Si
		101.2	$2p$	SiC_XO_Y
		102.3	$2p$	SiO_x
	O	530.6	$1s$	Al_2O_3
		532.3	$1s$	SiO_2
	C	284.6	$1s$	C=C
		288.1	$1s$	C=O
TiAlSiO	Ti	458.8	$2p_{3/2}$	TiO_2
		464.3	$2p_{1/2}$	TiO_2
	Al	73.5	$2p$	AlO_x
		74.6	$2p$	Al_2O_3

	Si	99.6	2p	Si-Si
		102.1	2p	SiO_x
	O	530.8	1s	Al_2O_3
		532.3	1s	SiO_2

Table 3.3: Summary of XPS analysis of each individual layer of the deposited tandem absorber.

3.3.6 Thermal stability of the tandem absorber in air and vacuum environments

Service life time of the solar absorber depends upon the thermal stability of the absorber. To study the thermal stability of the tandem absorber, coatings deposited on stainless steel were annealed in air for 2 h at different temperatures (300–550°C). Fig. 3.11(a) shows the reflectance spectra of the tandem absorber annealed at different temperatures for 2 h in air. These reflectance data show that the coating is stable up to 500°C for 2 h without any significant change in reflectance spectrum ($\Delta\alpha$ = 0.01 and $\Delta\varepsilon$ = 0.01). However, the change in reflectance spectrum of 550°C for 2 h shows degradation in the tandem absorber at 550°C ($\Delta\alpha$ = - 0.089 and $\Delta\varepsilon$ = +0.37). The changes in absorptance and emittance of the tandem absorber annealed in air at different temperatures are presented in Fig. 3.11(b). To further study the thermal stability of the coating in vacuum, the tandem absorber deposited on stainless steel substrate was heated in vacuum (6.0×10^{-4} Pa) for 2 h from 400–950°C.
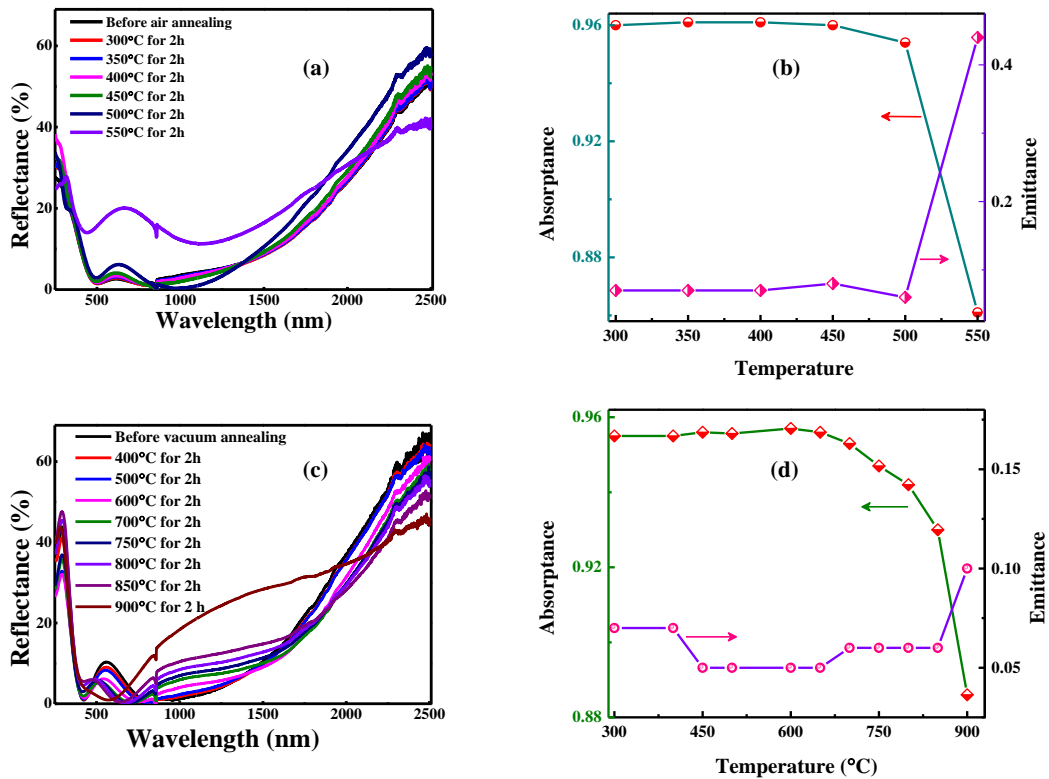
Figure 3.11: (a) Reflectance spectra of tandem absorber heat treated in air at 300, 350, 400, 450, 500, 550°C for 2 h. (b) The absorptance and emittance values of the tandem absorber measured after heat treatment in air at different temperatures. (c) Reflectance spectra of the tandem absorber heat treated in vacuum up to 900°C for 2 h. (d) The absorptance and emittance values of the tandem absorber measured after heat treatment in vacuum at different temperatures.

Fig. 3.11(c) shows the reflectance spectra of the tandem absorber vacuum annealed at different temperatures for 2 h. The reflectance spectrum of the tandem absorber annealed at 900°C for 2 h, clearly shows the overall increase in the reflectance in the range of 550 - 1930 nm, indicates the degradation of the tandem absorber. Fig. 3.11(d) clearly shows the variation of selective properties of the tandem absorber after annealing in vacuum environment at different temperatures. Absorptance of the tandem absorber is constant up to annealing temperature of 600°C and then decreases with the annealing temperature,

whereas the decrease in emittance value was observed at temperature 450°C, which is strongly attributed due to change in surface morphology such as: densification of the coating, decrease in porosity and increase in the grain boundaries (Vernoika et al., 2012). At higher annealing temperatures an increase in emittance is expected due to microstructural modifications such as: inter-diffusion of the layers or outward diffusion of the Fe, Cr from the SS substrate material, that reacts with the tandem layers of the coating and thus forming a new phase, which also leads to a decrease in the absorptance of the coating (Sibin et al., 2015). In the present experimental conditions, degradation of the coating due to oxidation is minimum because the annealing was carried out at a very high vacuum (6.0×10^{-4} Pa).

It is very important to study the long term thermal stability of the tandem absorber for solar thermal power generation applications. The tandem absorber was heated under cyclic heating conditions in air in a resistive furnace at a temperature of 300°C for 100 h. The reflectance spectra of the tandem absorber before and after annealing it at 300°C with different intervals were recorded as shown in Fig. 3.12. The reflectance data did not show any remarkable change in the reflectance after annealing for 100 h.
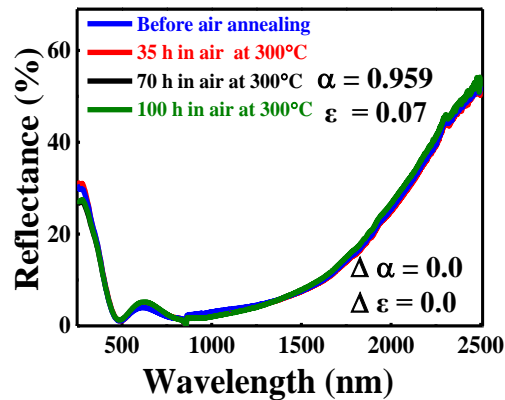
Figure 3.12: Reflectance spectra of tandem absorber heat treated in air at 300 °C up to 100 h.

After subjecting the tandem absorber at temperature of 300°C in air under cyclic heating conditions, there was negligible change in the intensity of the interference peak, indicating its stability up to 300°C for 100 h. To study the onset of the degradation of the

55

coating further cyclic heating in air was carried out at 325°C for up to 400 h and 350°C for 190 h. The corresponding reflectance spectra are shown in Fig. 3.13 (a) and (b). The data presented indicated the stability of the tandem absorber up to 325°C for 600 h. However, while heating the coating at 350°C in air for 190 h a marginal degradation in the optical properties was observed (Fig. 3.13(b)).
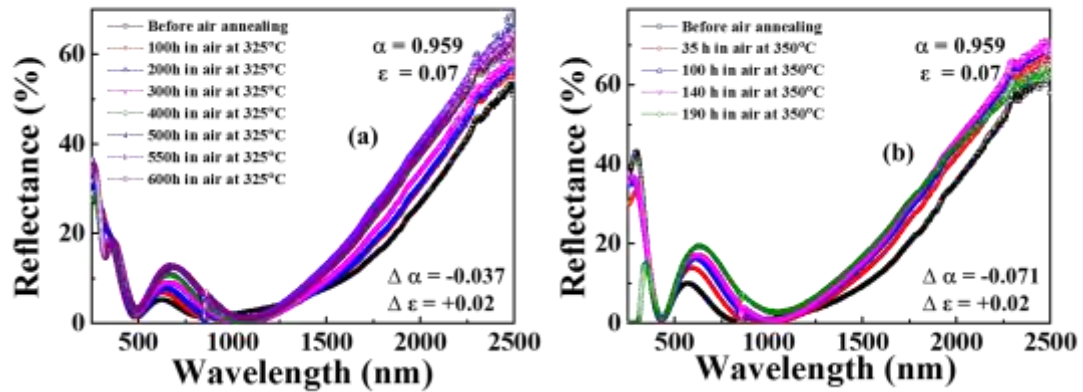
Figure 3.13: Reflectance spectra of tandem absorber heat treated in air at: (a) 325 °C for 600 h. (b) 350 °C for 190 h.

Long term thermal stability of the absorber coating in vacuum was also studied by subjecting the tandem absorber to annealing temperatures of 600°C and 650°C under cyclic heating conditions.
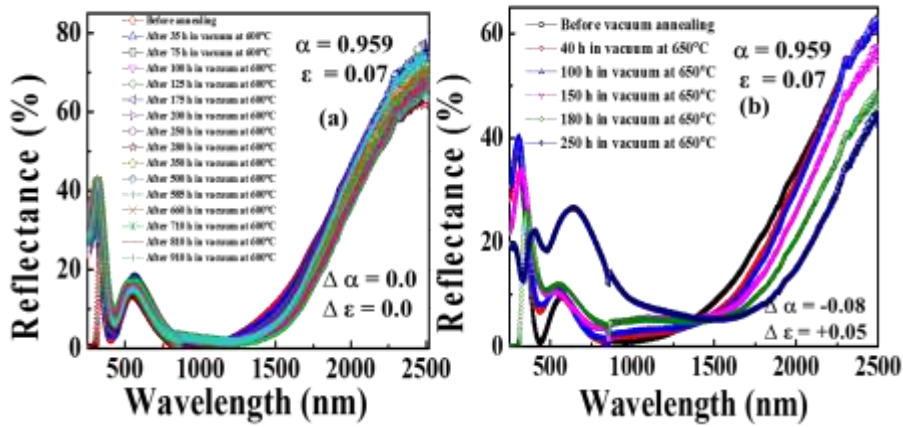
Figure 3.14: (a) and (b) Reflectance spectra of the tandem absorber heat treated in vacuum at: (a) 600°C for 190 h (b) 650°C for 250 h.

The corresponding reflectance spectra recorded after different intervals are displayed in Fig. 3.14(a) and (b). For the annealing temperature of 600°C no changes in the absorptance and emittance values were observed up to 910 h. However, at 650°C marginal changes in the absorptance ($\Delta\alpha = 0.08$) and the emittance ($\Delta\varepsilon = 0.05$) were observed.

The annealing experimental results were corroborated using the X-ray diffraction data as presented in Fig. 3.15. It is evident from the figure that the absorber coating is stable up to 325°C when heated in air for 600 h under cyclic heating conditions (Fig.
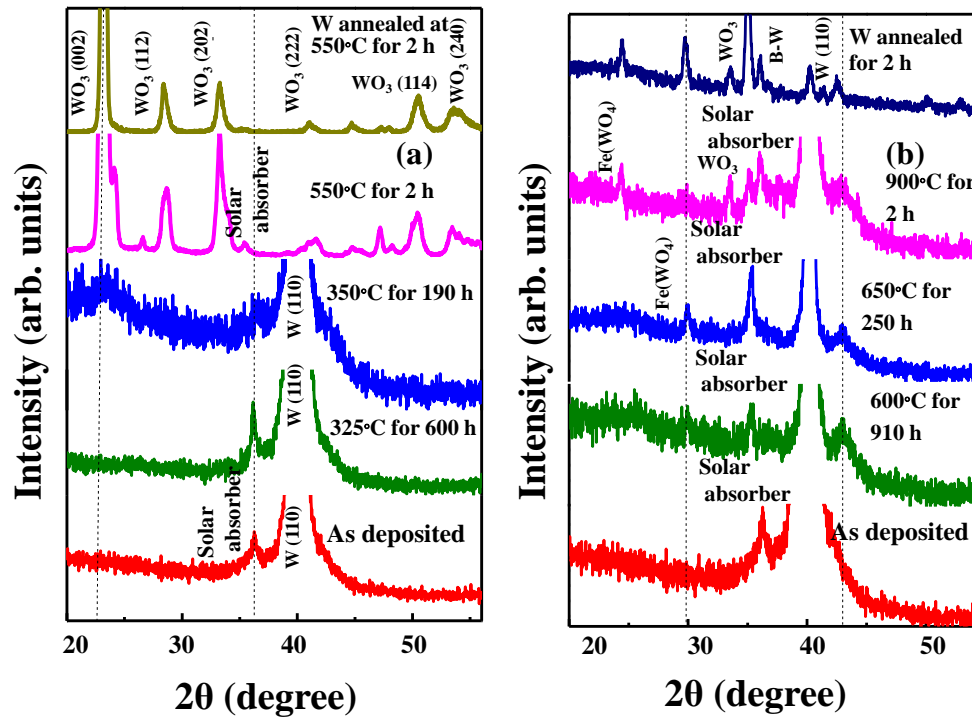
Figure 3.15: (a) X-ray diffraction data of the tandem absorber after heat treatment in air at different temperatures and durations. Also shown is the X-ray diffraction data of tungsten coated stainless steel heat treated in air at 550°C for 2h. (b) X-ray diffraction data of the tandem absorber heat treated in vacuum up to 900°C for different durations. See text for details. Also shown is the XRD data of tungsten coated stainless steel heat treated in vacuum at 900 °C, demonstrating the oxidation of W interlayer.

3.15(a)). Whereas, when coating was heated at 550°C in air even for 2 h there was a complete out-diffusion of tungsten and subsequent oxidation, thus deteriorating the optical properties of the tandem absorber as also seen in the UV-VIS-NIR spectra ((Fig. 3.11(a)). Annealing in vacuum, however, exhibited different behavior. Chemical composition of the vacuum annealed and air annealed samples was studied by using the XPS. Fig. 3.16 shows the XPS core level spectra of the tandem absorber of as-deposited, annealed in air and vacuum at 325°C and 650°C, respectively. There is no significant change in Ti2p and Al2p

core level spectra after annealing in air and vacuum. No major differences in absorptance and emittance properties of the vacuum annealed tandem absorber is observed (α_{AD} = 0.961; ε_{AD} = 0.15; α_{vac} = 0.959 ~ 0.960; ε_{vac}= 0.15).
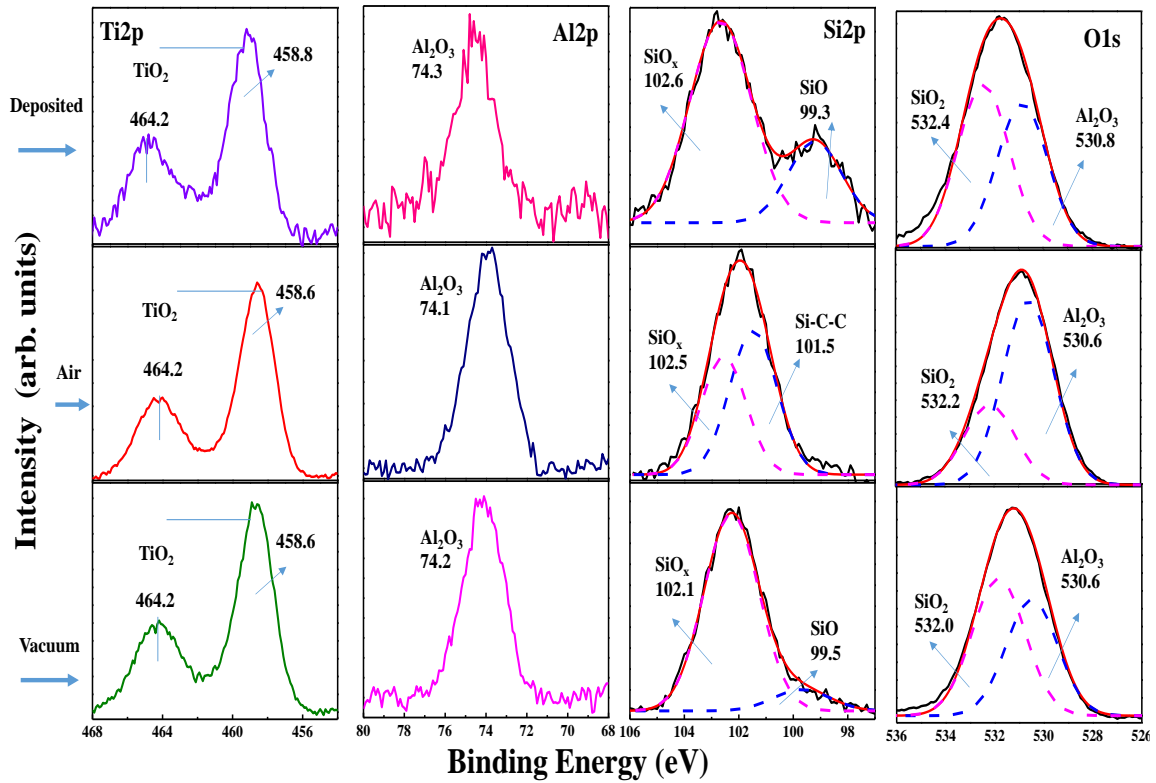
Figure 3.16: XPS core level spectra of the tandem absorber of as-deposited, annealed in air and vacuum at 325°C and 650°C for 600 h and 250 h, respectively.

However, a minor decrease in these properties is seen in the sample annealed in air (α_{AD} = 0.961; ε_{AD} = 0.15; α_{air} = 0.941; ε_{air}= 0.15). This degradation of optical properties is due to the formation of new phase SiC as observed in its Si2p spectrum that results due to outward diffusion of carbon to the top layer. O1s core level spectra of the air annealed tandem absorber show the increase in intensity of the Al_2O_3 with a decrease of the SiO_2 which is due to the less heat of formation of Al_2O_3 (-1675.7 kJ/mol) as compared to silicon oxide (-910 kJ/mol) (Robert et al., 1982).

The high thermal stability of the tandem absorber of the present work has been attributed to various factors, but primarily due to very high thermal stability of the

individual layers. The selection of the tandem absorber has been done by reviewing their properties at higher temperatures from the existing literature. For instance, the first four layers of the tandem absorber namely: TiAlC, TiAlCN, TiAlSiCN, TiAlSiCO have been widely used as high temperature materials with superior mechanical properties for various tribiological applications. Tallmann et al. have reported that Ti_2AlC exhibits cubic oxidation kinetics in air up to 1200°C, indicating its stability at higher temperatures (Tallmann et al., 2013). Similarly, high activation energy for oxidation in air of ~279 kJ/mol has been reported by Basu et al. (Basu et al., 2012) for Ti_2AlC. TiAlCN also shows the thermal stability up to 1200°C in air while maintaining its cubic structure at these temperatures (Shtansky et al., 2011). The addition of carbon in TiAlCN not only improves its thermal stability but also the toughness of the coating (Kuptsov et al., 2013). The oxidation behavior of TiAlSiCN has been studied extensively by Shtansky et al. (Shtansky et al., 2009; Shtansky et al., 2009; Kuptsov et al., 2013). Their studies indicate the formation of TiO_x and SiC underneath the alumina film, when TiAlSiCN was heated up to 1300°C in air (Shieh et al., 2005). Oxy-carbides such as Al_2OC, Al_4O_4C and TiAlSiCO have also been reported to exhibit high thermal stability up to 1400°C as they form Al_2O_3, SiC, SiO_2, TiC and Al_2OC compounds after annealing at high temperatures (Sitnikov et al., 2004). As for the anti-reflection coating (TiAlSiO) is concerned, it is believed that it is a mixture of amorphous phases (as evident from the XRD data (Fig. 3(c)) of Al_2O_3, TiO_2, SiO_2 and AlTiO, all of which are highly thermally stable materials (Mikhelashvili et al., 2006; Shi et al., 2007; Edlmayr et al., 2010). When TiAlSiO is exposed in air at high temperature it is believed that a thin layer consisting of Al_2O_3, TiO_2/Ti_2O_3 and SiO_2 forms as the heat of formation of these compounds is very low (ΔH_f = -400.5, -363.5, -217.3 and -124.2 kcal/mol, respectively for Al_2O_3, Ti_2O_3, SiO_2 and TiO_2) (Robert et al., 1982). This oxide surface layer protects the underlying layer(s) from further oxidation.

In general, annealing of the multilayer coatings may induce several microstructural modifications such as inter-diffusion between the layers, reaction between the individual layers to produce a new phase, transformation within one or all the layers and finally oxidation of the individual layers. The analysis presented above substantiates that because

of very high structural stability of the individual layers, the above mentioned microstructural modifications do not occur predominantly in the tandem absorber of the present work. So far as the out-diffusion of iron from SS substrate onto the tandem absorber is concerned, tungsten interlayer acts as a diffusion barrier between the stainless steel substrate and the tandem absorber (Cao et al., 2015; Sibin et al., 2015). Additionally, as there are 6 different layers in the multilayer tandem absorber of the present work (including W layer), presence of 6 interfaces improves the overall quality of thin film thus formed. These interfaces help in reducing the porosity of the coating and also help in blocking the formation of columnar microstructure of the coating, a common feature observed in the sputtered coatings. These in turn help in increasing the density of the of the tandem absorber and also obstruct the formation of through pin holes, thereby improving the performance of the absorber coating when subjected to thermal treatments.

3.3.7 Environmental stability of the coating

The coatings were also subjected to corrosion and salt spray tests to demonstrate the environmental stability of the coatings. Additionally, the water contact angle was measured on optimized solar absorber coating. These results are briefly discussed below:

Potentiodynamic polarization curve of tandem absorber deposited on stainless steel substrate obtained in a non-deaerated 3.5% NaCl solution is shown in Fig. 3.17(a). The behavior of a stainless steel substrate is also added for a comparison. The corrosion parameters calculated for both the tandem absorber deposited on stainless steel and the bare stainless steel using Tafel extrapolation method are given in Table 3.4. The shift in corrosion potential to the positive side was observed in tandem absorber coated on stainless steel as compared to that of the uncoated stainless steel substrate. This shift in corrosion potential indicates the better corrosion resistance of the tandem absorber coating.

Samples	E_{corr} (V)	I_{corr} (A/cm^2)	R_p (Ω cm^2)
SS	-0.200	5.18×10^{-7}	37.2 E+3
Coating	-0.094	3.35×10^{-10}	111.2 E+6

Table 3.4: Potentiodynamic polarization data of the tandem absorber coating on stainless steel substrate in 3.5% NaCl solution.

The tandem absorber deposited on stainless steel was also subjected to salt spray test in 3.5% NaCl solution as per ASTM B117 standard. The tests were carried out for 168 h. No significant changes in the absorptance and emittance were observed as a result of the salt spray test as shown in Table 3.5. Further, no corrosion pits were observed on the sample surface after slat spray test (Fig. 3.17(b)). The corrosion data was further supported by salt spray test. These results demonstrate that the deposited tandem absorber shows good chemical resistance.

Exposure duration (hours)	As-deposited (α)	After salt spray test (α)	As-deposited (ε)	After salt spray test (ε)
168	0.960	0.959~0.960	0.15	0.15

Table 3.5: Absorptance and emittance data of tandem absorber deposited on stainless steel substrate after salt spray tests.

The hydrophobic nature of the tandem absorber can be quantified by measuring the contact angle of water droplet with the surface. Fig. 3.17(c) shows image of water droplet on the tandem absorber deposited on the stainless steel. The contact angle of the tandem absorber was 92°, indicating its hydrophobic nature. This may be due to the less defects in the deposited tandem absorber and low roughness as displayed in Fig. 3.2(b).
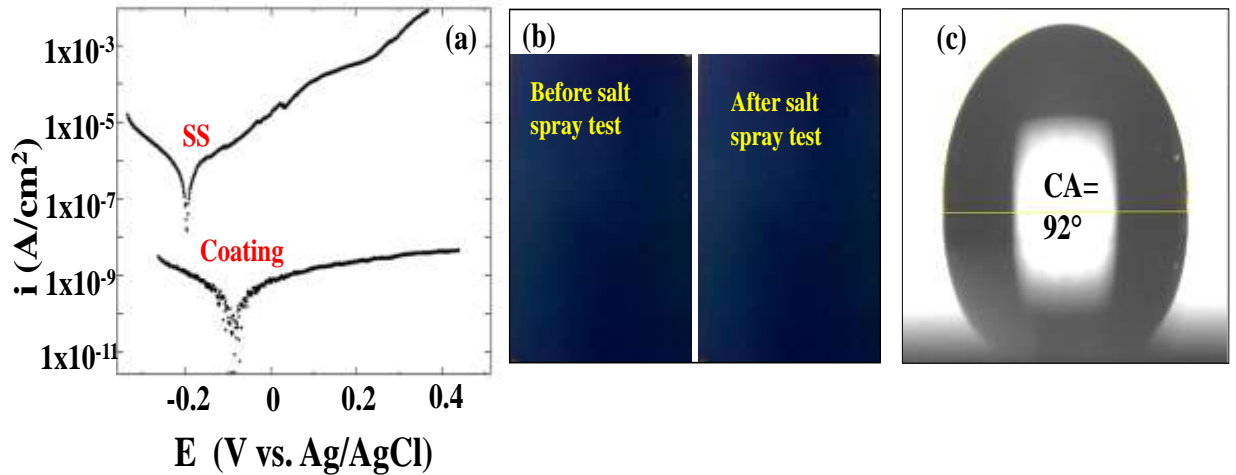
Figure 3.17: (a) Potentiodynamic polarization data of designed tandem absorber coating on stainless steel substrate in 3.5% NaCl solution. (b) Photographs of sample before and after salt spray test. (c) Water drop contact angle image of the tandem absorber deposited on stainless steel substrate.

In summary, the tandem absorber of the present work exhibits $\alpha = 0.961$, $\varepsilon_{82°C} = 0.07$ and thermal stability in air and vacuum up to 325°C and 650°C for long durations. These findings are significant for the solar thermal power generation applications considering the fact that the state-of-the-art absorber coating exhibits thermal stability up to 580°C under vacuum for 14 days (Esposito et al., 2009).

3.4 SUMMARY

➢ Spectrally selective surfaces of W/TiAlC/TiAlCN/TiAlSiCN/TiAlSiCO/TiAlSiO were deposited on stainless steel substrates using unbalanced magnetron sputtering system with absorptance of 0.961 and emittance of 0.07 at 82°C.

➢ The design of the coating has been achieved by controlling the electrical resistivity and the thicknesses of the individual layers.

➢ The thickness of the deposited tandem absorber was analyzed using cross–sectional TEM images and roughness of the tandem absorber shows RMS ~3.5 nm studied by AFM.

- ➢ The measured resistivity and reflectance data confirmed the decrease of metallic nature from bottom to the top layer of the tandem absorber.

- ➢ Detailed characterization such as structural and compositional analysis of the tandem absorber was carried out by the XRD and XPS.

- ➢ The performance evaluation of the tandem absorber was studied by heating it in air and vacuum at different temperatures.

- ➢ The tandem absorber shows the high thermal stability in air up to 500°C for 2 h whereas, the tandem absorber shows the high thermal stability in vacuum up to 850°C for 2 h

- ➢ The designed tandem absorber shows the long term thermal stability in air up to 350° C for 190 h, in vacuum up to 600°C for 910 h and 650°C for 250 h

- ➢ The tandem absorber of the present work is, thus, highly stable and suitable for high temperature solar thermal power generation applications.

- ➢ The coating also passed environmental tests.

Chapter 4

Effect of Composition on Selective Properties of the TiAlC/ TiAlCN/ TiAlSiCN/ TiAlSiCO/ TiAlSiO Tandem Absorber

The present work reveals the dependence of optical properties on composition and thicknesses of each individual layer of the tandem absorber to achieve spectrally selective properties.

4.1 INTRODUCTION

Recent progress in the solar selective coatings for solar thermal high temperature applications shows that a large number of Ti, Al, Si, Hf, etc., based coatings and their combination have been reported by the researchers. Diu et al. reported the design of TiAlN/TiAlN/AlN coating with a high absorptance of 0.945 and emittance of 0.04 (Du et al., 2011). Feng et al. prepared the selective absorbing coatings on stainless steel and copper substrates, which show a high absorptance of 0.950. The coating was stable up to 700°C in vacuum (Feng et al., 2015). Yongxin et al. studied the thermal stability of Al/NbTiSiN/NbTiSiON/SiO$_2$ multilayer solar selective absorber coating which shows the thermal stability up to 550°C in vacuum for 100 h (Yongxin et al., 2015). Liu et al. have designed a new spectral selective coating of SS/ (Fe$_3$O$_4$)/Mo/TiZrN/TiZrON/SiON for high temperature application (Liu et al., 2014). The functional multilayer nitride coatings of Cu/TiAlCrN/TiAlN/AlSiN on SS and Cu substrates were studied by Krishna et al., which showed an absorptance of 0.910 and emittance of 0.07 (Krishna et al., 2014). Barshilia et al., have also developed a large number of selective coatings and their performance evaluation at high temperatures for solar thermal power applications has been studied in detail. These include: TiAlN/TiAlON/Si$_3$N$_4$ (Barshilia et al., 2006, 2007, 2008; Biswas et

al., 2008), TiAlN/AlON (Barshilia et al., 2008), HfO$_x$/Mo/HfO$_2$ (Selvakumar et al., 2010), HfMoN/HfON/Al$_2$O$_3$ (Selvakumar et al., 2012), Ti/AlTiN/AlTiON/AlTiO (Barshilia, 2014), W/AlHfN(H)/AlHfN(L) (Selvakumar et al., 2015) and HfMoN/HfON/Al$_2$O$_3$ (Selvakumar et al., 2015). All these coatings have been prepared using a magnetron sputtering process and exhibit high absorptance > 0.940 and emittance < 0.10 with very high temperature stability.

The carbides and carbonitrides of Ti, Al and Si are used for hard coating applications due to their unique properties of high hardness, better resistance of oxidation, etc. (Siow et al., 2012). It might be possible to achieve the selective properties of the transition metal carbides, carbo-nitrides, oxy-nitrides, oxides by controlling their stoichiometry, which affects the density of 'd' band free electrons (Selvakumar et al., 2015). In Chapter 3, the design of a tandem absorber consisting of TiAlC/TiAlCN/TiAlSiCN/TiAlSiCO/TiAlSiO is studied. The designed tandem absorber shows an absorptance of 0.961 and an emittance of 0.07 on W coated SS substrates.

This chapter presents mainly the detailed optimization of the TiAlC/TiAlCN/ TiAlSiCN/TiAlSiCO/TiAlSiO tandem absorber. The effects of composition and thicknesses of the individual layers of the coating on the optical properties are studied in detail.

4.2 EXPERIMENTAL PROCEDURE

Optimization of the process parameters plays a major role in achieving selective properties of the tandem absorber. Especially, sputtering has so many process parameters, which need to be optimized. In order to study the detailed effect of thicknesses of the individual layers and reactive gas flow rates on the optical properties of the tandem absorber, the target power, substrate bias, operating pressure and substrate temperature were kept as constant. The tandem absorber (TiAlC/TiAlCN/TiAlSiCN/ TiAlSiCO/TiAlSiO) was deposited on stainless steel substrate (35 mm x 35 mm). ENI make power supply (Model No.: RPG - 50) with a frequency of 100 kHz, pulse width of 2976 ns, duty cycle of 30%, reverse bias of +37 V and power of 5 kW was used for the experiments. Before placing the substrate into the vacuum chamber, they were polished

and chemically cleaned. The samples were loaded into the vacuum chamber and evacuated up to a base pressure of 8.0×10^{-4} Pa. High purity (>99.9%) titanium (2 No.), one silicon and one aluminum targets were used for the deposition. Firstly, plasma cleaning (Ar ion bombardment with a bias voltage of -1000 V) was done for 15 min to remove the impurities from the substrate surface. The designed tandem absorber of five layers was deposited by reactive sputtering of four targets in the $Ar+C_2H_2$, $Ar+C_2H_2+N_2$, $Ar+ C_2H_2+O_2$, $Ar+O_2$ plasmas, respectively. In order to optimize the composition of TiAlC, target power (Ti: 300 W, Al: 350 W), substrate bias (-100 V), operating pressure (0.15 Pa) and deposition time (3 min 20 s) were kept constant while varying the C_2H_2 flow rate from 1.5 sccm – 3.5 sccm. Reflectance data were studied for all the varied flow rates. The optimized flow rate was selected at which reflectance spectrum shows low reflectance (i.e., high absorptance). The next step was the optimization of deposition time (in other words thickness) which was varied from 2 min to 5 min 30 sec by keeping all the process parameters constant. The deposition time at which reflectance spectrum shows a low reflectance was selected as the optimized deposition time. Further, the composition and the thicknesses of each individual layers (TiAlCN, TiAlSiCN, TiAlSiCO, TiAlSiO) were optimized as discussed before. In order to densify the coating, deposition of the tandem absorber was carried out at a substrate temperature of 300°C. A DC bias of -100 V was given to the substrate while depositing the absorber layers (expect for the antireflection layer) to improve the adhesion and mechanical properties of the coating.

4.3 RESULTS AND DISCUSSION

The first aim of this study was to optimize the process parameters like sputtering power, flow rates of reactive gases (C_2H_2, N_2 and O_2) and thicknesses of individual layers. The flow rate of reactive gases controls the composition of the deposited layers, which coupled with thickness determines the optical properties of the solar selective coatings. The effects of various parameters on the optical properties of the tandem stack are presented below.

4.3.1 Optimization of TiAlC layer

In the tandem absorber, thickness and composition of the layer affect the selective properties (i.e., α and ε) of the coating. In order to achieve the maximum absorptance of

67

the first layer, the composition of the first layer (TiAlC) was optimized by varying the C_2H_2 flow rate from 1.5 to 3.5 sccm, while maintaining the target power Al (300 W) and Ti (350 W), substrate temperature (300°C) and substrate bias (-100 V) constant. Fig. 4.1(a) shows the reflectance data of TiAlC layer prepared at different C_2H_2 flow rates while keeping deposition time constant (3 min 30 sec). Initially, the reflectance minimum shifts to higher wavelength for films prepared with C_2H_2 flow rate of 1.5 – 2.5 sccm. The shift in the reflectance minimum towards higher wavelength indicates an increase in the dielectric nature or thickness of the film (Shuxi et al., 2006). Fig. 4.1(b) clearly shows that the film thickness decreases with an increase in C_2H_2 flow rate. The effect of the shift in the reflectance minimum towards higher wavelength for the films prepared at C_2H_2 flow rate of 1.5- 2.5 sccm is, therefore, due to increase of dielectric nature of the film. However, on further increase in the C_2H_2 flow rate (i.e., 3 - 3.5 sccm), the reflectance minimum shifts towards shorter wavelength, which is attributed to a decrease in the layer thickness. With increase in C_2H_2 flow rate the thickness of the layer decreases as shown in Fig. 4.1(b), this is due to target poisoning (Berg et al., 1991). Fig. 4.1(c) shows that an increase in the flow rate of C_2H_2 from 1.5 - 3.5 sccm gradually decreases the titanium and aluminum target voltages. This data confirms that an increase in the flow rate of C_2H_2 causes target poisoning. Due to the target poisoning (formation of Al_2O_3, SiO_2 and TiO_2 insulting layers on the targets) the film growth rate decreases which results in a decrease in the thickness of the film. Pulsed DC power sources were used to minimize this effect. The reflectance curves show that for the film prepared at C_2H_2 flow rate of 2.5 sccm, the reflectance was minimum (i.e., high absorptance, 0.761) as compared to all other C_2H_2 flow rates. Therefore, the optimized C_2H_2 flow rate was kept constant at 2.5 sccm for the subsequent experiments.
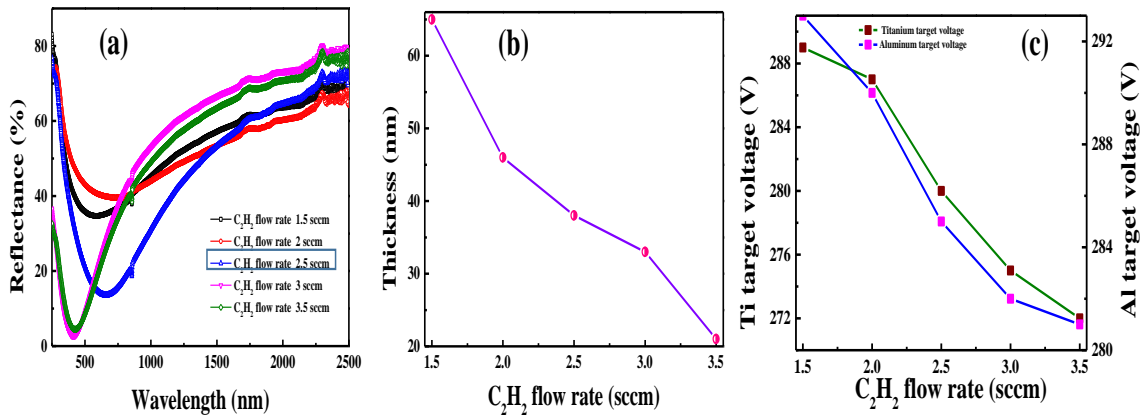
Figure 4.1: (a) Reflectance spectra of the TiAlC deposited at various C_2H_2 flow rates. (b) Variation of TiAlC layer thickness as a function of C_2H_2 flow rate. (c) C_2H_2 flow rate versus the titanium and aluminum target voltages.

Next the effect of coating thickness on the optical properties was studied. In order to optimize the thickness of the TiAlC layer, all the process parameters were kept constant and C_2H_2 flow rate at 2.5 sccm, while varying the deposition time from 2 min to 4 min 30 sec. Fig. 4.2(a) shows the reflectance spectra of the films prepared at different deposition times. An increase in thickness of the film influences the position of the first interference minimum (Shuxi et al., 2006). Fig. 4.2(a) shows that the first reflectance minimum shifts towards higher wavelength due to an increase in the thickness of the film, which is confirmed by the thickness data for films prepared at different deposition times (Fig. 4.2(b)). The reflectance spectra of the TiAlC films prepared at different deposition times indicate that the coating prepared with a deposition time from 2 min to 3 min 30 sec show only one reflectance minimum, while the TiAlC layers prepared at 4 min and 5 min 30 sec show two reflectance minima due to destructive interference. The reflectance spectrum of the TiAlC prepared for 3 min 30 sec shows low reflectance in overall wavelength range. The absorptance for this optimized layer was 0.761 ($\varepsilon = 0.11$). So, overall optimized parameters for the first layer are: Ti target power: 350 W, Al target power: 300 W, substrate temperature: 300°C, substrate bias: -100 V, C_2H_2 flow rate: 2.5 sccm and deposition time: 3 min 30 sec.
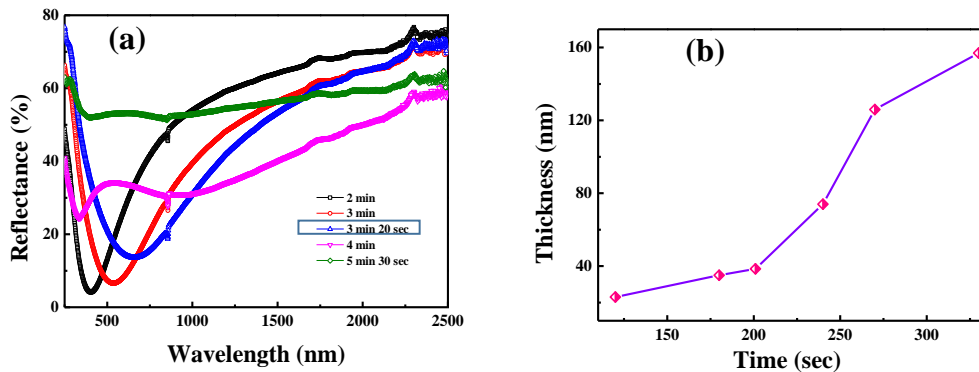
Figure 4.2: (a) Reflectance spectra of the TiAlC layer at different deposition times. (b) The variation of the thickness of TiAlC layer with different deposition times.

4.3.2 Optimization of TiAlCN layer

In order to increase the absorptance of the tandem absorber, the second layer (i.e., TiAlCN) was incorporated on top of the TiAlC layer. TiAlCN was optimized in a similar way as was the first layer. The only extra variable for this layer was the N_2 flow rate. First, the effect of C_2H_2 flow rate on the TiAlCN layer and target voltages was studied while keeping the N_2 flow rate constant (i.e., 8 sccm). Fig. 4.3(a) and Fig. 4.3(b) show the reflectance spectra as well as Ti and Al target voltages as a function of C_2H_2 flow rate. It may be noted that R values as well as target voltages and thicknesses of the TiAlCN layer follow similar trend as has been discussed for the first layer. It is clear from the Fig. 4.3(a) that for TiAlCN layer prepared with C_2H_2 flow rate of 3 sccm shows the lowest reflectance (i.e., high absorptance) in the overall wavelength range and thus, the C_2H_2 flow rate of 3 sccm was taken as the optimized flow rate for this layer. The detailed study of effect of nitrogen flow rate on the optical properties of TiAlCN is also presented while keeping the C_2H_2 flow rate constant at 3 sccm and varying the nitrogen flow rate from 6-10 sccm. Fig. 4.3(c) shows the reflectance spectra of TiAlCN layer at different nitrogen flow rates. Sample prepared with nitrogen flow rate at 8 sccm shows overall low reflectance and thus high absorptance (0.803). It is worthwhile to note that the addition of N_2 in the sputtering chamber also leads target poisoning as indicated in Fig. 4.3(d), which leads to a decrease in the thickness of the TiAlCN (see inset of Fig. 4.2(d)). Reflectance studies (Fig. 4.4(a)) for the TiAlCN films

70

prepared at different thicknesses indicated that for TiAlCN coating prepared at a thickness of 79 nm (Fig. 4.4(b)) yielded the highest absorptance for TiAlC/TiAlCN tandem absorber (i.e., $\alpha = 0.803$, $\varepsilon = 0.11$).
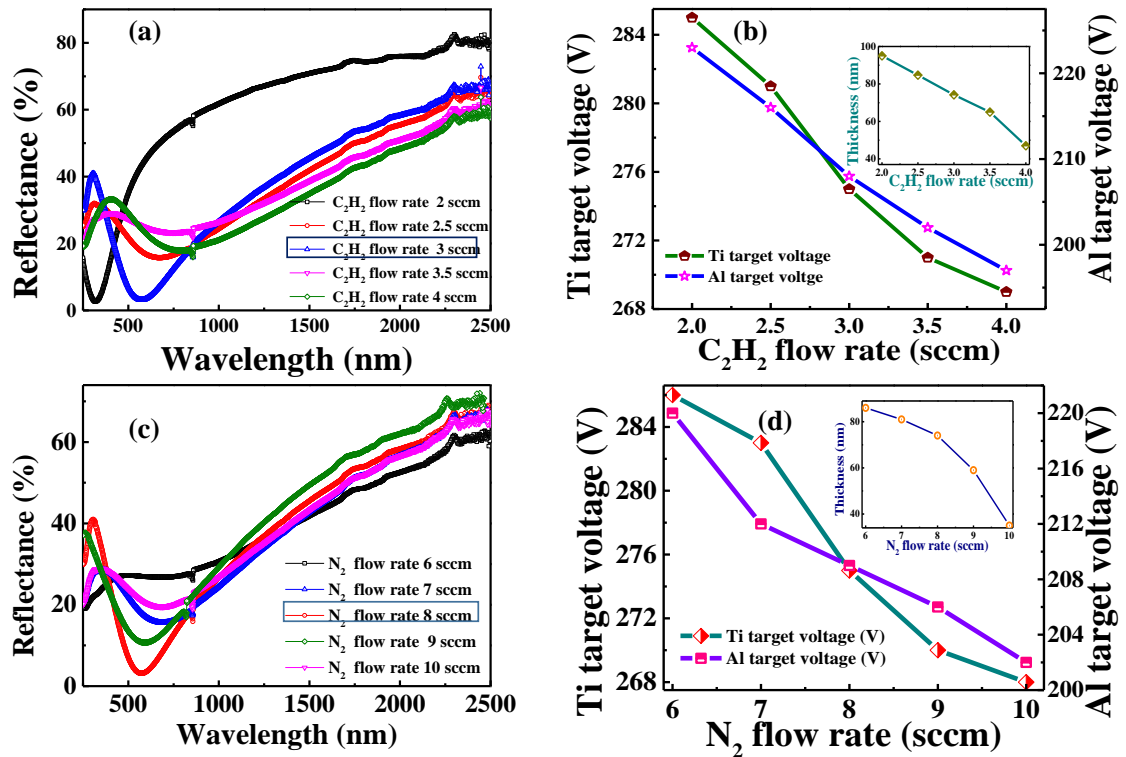
Figure 4.3: (a) The reflectance spectra of the TiAlCN layer deposited with different C_2H_2 flow rates at constant deposition time and process parameters. (b) Titanium and aluminum target voltages versus C_2H_2 flow rate. (c) Reflectance spectra of the TiAlCN layer at different N_2 flow rates. (d) N_2 flow rate versus titanium and aluminum target voltages
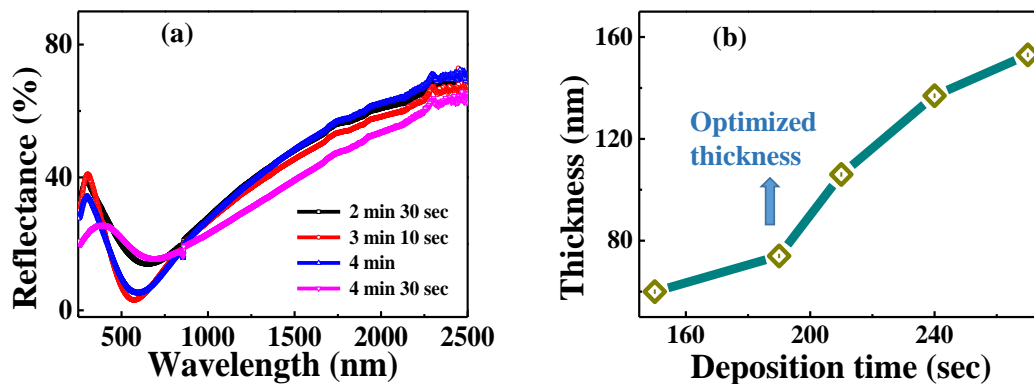
Figure 4.4: (a) Reflectance spectra of the TiAlCN layer with varied deposition time. (b) Variation of thickness of TiAlCN layer with deposition time.

The third absorbing layer (TiAlSiCN) was incorporated on top of TiAlC and TiAlCN layers to further enhance the absorptance of the tandem absorber. Silicon was added to this layer to improve the overall thermal stability and to control the electrical properties. The influence of flow rates such as C_2H_2, N_2 and thickness on the optical properties of TiAlSiCN showed a similar trend as discussed above for TiAlC and TiAlCN layers. With this layer, the absorptance of the tandem absorber was increased to 0.882 (ε = 0.13).

4.3.3 Optimization of TiAlSiCO and TiAlSiO layers

Now the optimization of the fourth layer, i.e., TiAlSiCO will be discussed, which acts as a semitransparent layer. For this layer only the oxygen flow rate was optimized and the layer thickness of the TiAlSiCO. Fig. 4.5(a) shows the influence of oxygen flow rate on the reflectance spectra of the TiAlSiCO layer. It is seen from the figure that reflectance spectra show two minima due to destructive interference along with one maximum. The reflectance spectrum for TiAlSiCO layer prepared at oxygen flow rate at 2 sccm shows more increase of reflectance in NIR region.
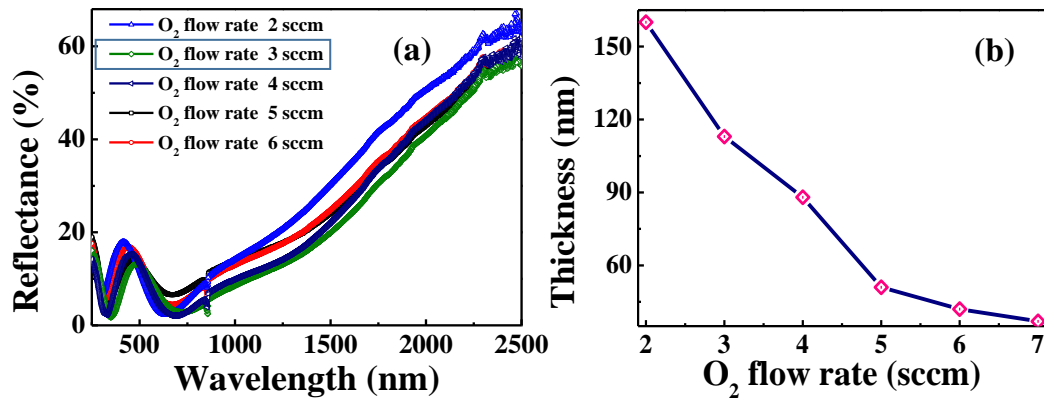
Figure 4.5: (a) The reflectance spectra of the TiAlSiCO layer deposited with different O_2 flow rates at constant deposition time and process parameters. (b) The thickness of the TiAlSiCO layer with varied O_2 flow rates.

It is clear from Fig. 4.5(a) that the oxygen flow rate at 3 sccm shows a decrease of reflectance in the overall wavelength range. Further increase of oxygen flow rate shows a gradual increase of reflectance. So, the optimized oxygen flow rate for TiAlSiCO layer was found to be 3 sccm, which corresponds to an overall absorptance of tandem absorber consisting of four layers to 0.912 ($\varepsilon = 0.14$).

As we know that the oxygen is a highly reactive gas, increase of oxygen flow rate leads to a decrease of growth rate as depicted in Fig. 4.5(b), which is attributed to target poisoning (Waite et al., 2007). These results were further corroborated by decrease in target voltage values for Ti, Al, Si cathodes (Fig. 4.6(a-c)).
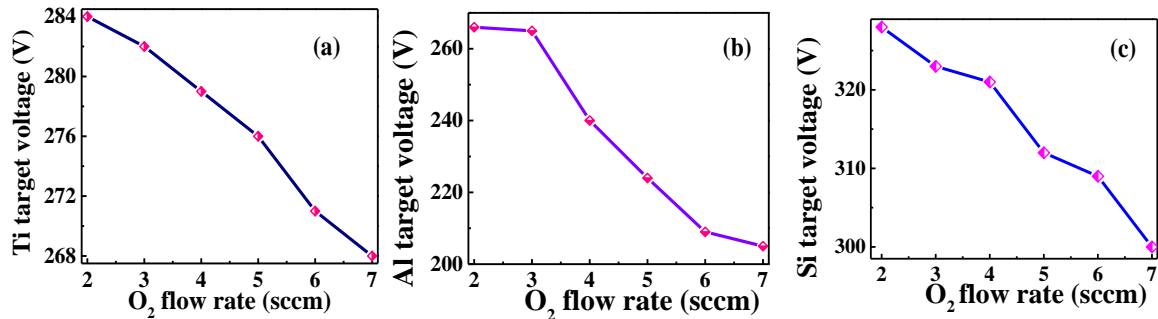
Figure 4.6: (a) Variation of titanium target voltage with O_2 flow rate. (b) Effect of O_2 flow rate on aluminum target voltage. (c) O_2 flow rate versus silicon target voltage.

It must be noted that in order to minimize the target poisoning, bipolar pulsed DC power supplies was used for the reactive sputtering of Ti, Al and Si targets. The pulsed sputtering technology is capable of preparing non-conducting high quality films along with high growth rate and density (Barshilia et al., 2006). In the next set of experiments, the thickness of TiAlSiCO layer was optimized. The increase of deposition time increases the thickness of the coating as shown in the Fig. 4.7(a). The corresponding effect of coating thickness on the optical properties was studied by measuring the reflectance spectra. Fig. 4.7(b) shows the reflectance spectra of the TiAlSiCO layer deposited at different deposition times and film prepared for 7 min yielded the highest absorptance (0.912).
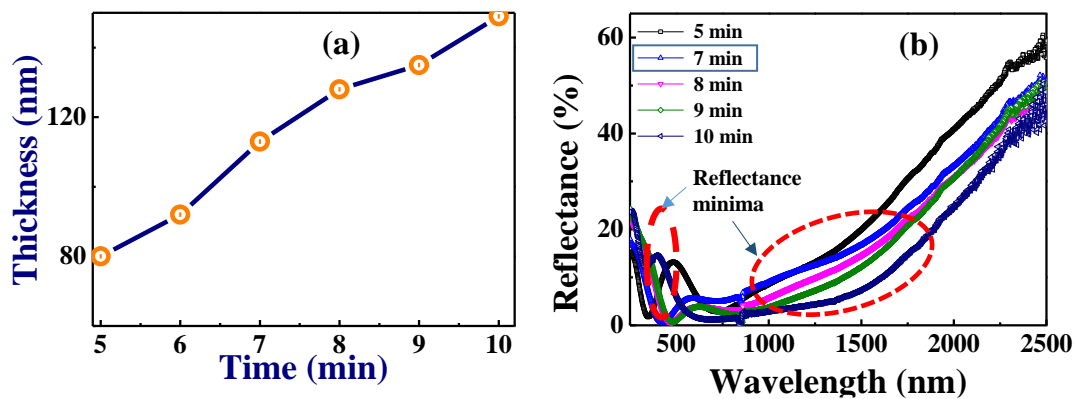
Figure 4.7: (a) The thickness of the TiAlSiCO layer with deposition time. (b) Reflectance spectra of the TiAlSiCO layer at different deposition times.

74

From the figure it is clear that first reflectance minimum shift towards higher wavelength and also the reflectance decreases in the NIR region.

   As the thermal stability of the absorber coating is very important from the application point of view (Barshilia et al., 2008), a very thin (10-30 nm) layer of TiAlSiO, which is completely transparent was introduced.
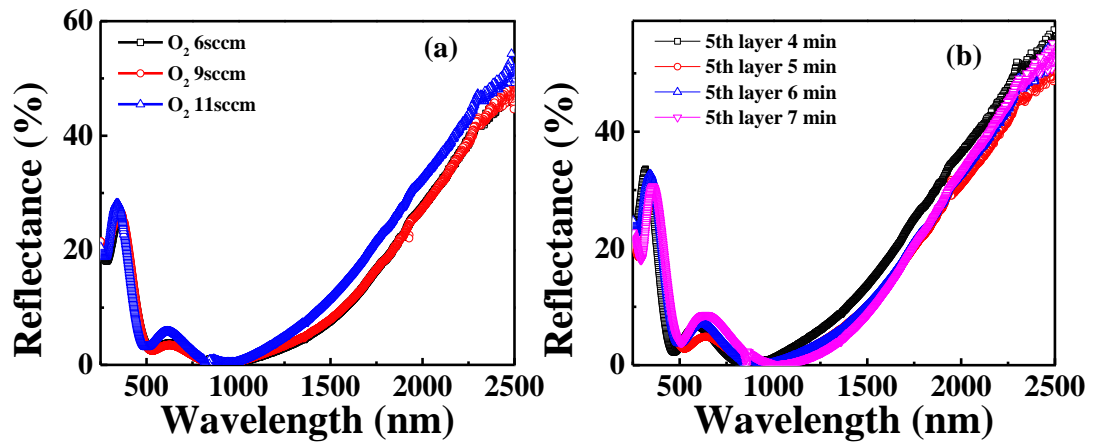
Figure 4.8: (a) Reflectance spectra of the TiAlSiO layer at different O_2 flow rates. (b) The change in reflectance spectra of TiAlSiO layer with different deposition times.

Again the oxygen flow rate and the thickness of this layer were varied to study the optical properties.

   Fig. 4.8(a) indicates that the absorptance did not change significantly ($\alpha \sim 0.960$) when the oxygen flow rate was in the range of 6-9 sccm. On the other hand, a slight decrease in the absorptance (Fig. 4.8(a)) was observed at oxygen flow rate of 11 sccm. Fig. 4.8(b) shows the reflectance spectra of the TiAlSiO layer at different deposition times. It is clear from the figure that deposition time at 5 min shows the low reflectance, further increase in the deposition time did not show any substantial change in the reflectance spectra. So, deposition time of 5 min for TiAlSiO coating resulted in absorptance of 0.960 ($\varepsilon = 0.15$).

   The positive effect of addition of 5th layer on the thermal stability of the tandem absorber was demonstrated by heating four layer and five layer tandem absorbers in air at

450°C and 550°C for 2h. The corresponding reflectance spectra are presented in Fig. 4.9(a) and Fig. 4.9(b). When the coatings were heat treated at 450°C, both the four and five layer coatings exhibited marginal decrease in the absorptance. However, when they were heat treated at 550°C for 2h, the four layer coating degraded faster ($\Delta\alpha = 0.199$) when compared to 5 layer coating ($\Delta\alpha = 0.166$). Further, the deposited tandem absorber shows a high reflectance (> 95% at 25 μm) in the IR region, which was studied using the FTIR (Fig. 4.9(c)), again confirming low thermal emittance of the deposited coating.
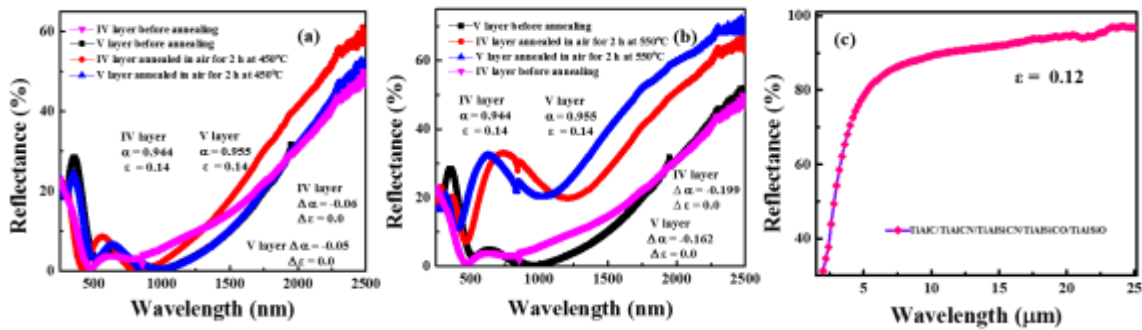
Figure 4.9: (a) Reflectance spectra of the heat treated tandem absorber with and without antireflection layer in air at 450°C for 2h. (b) Reflectance spectra of the heat treated tandem absorber with and without antireflection layer in air at 550°C for 2h. (c) FTIR spectrum of the tandem absorber deposited on stainless steel substrate.

In summary, the experimental reflectance data presented in Figs. 4.1 – 4.9 clearly indicate that single layer thin coating (i.e., TiAlC) with thickness < 80 nm exhibits one minimum only with very high reflectance in the visible region. Whereas, the multilayer system exhibited two minima and one maximum. Further, with an increase in thickness of the coating, in general, the reflectance maximum shifts to higher wavelength and its intensity decreases, which is consistent with the reported literature (Heavens et al., 1965). Therefore, by adjusting the individual layer thicknesses and their refractive indices (that is the composition) it is possible to achieve almost zero reflectance at two wavelengths, viz., at 1050 and 490 nm for the optimized absorber coating of the present work. This enable reducing the reflectance of the multilayer coating in the solar spectrum, thus increasing the absorptance of the coating.

4.3.4 XPS studies of change in composition of the tandem absorber with reactive gas flow rates

The effect of reactive gas flow rates on the composition and the chemical state of the each individual layer of the tandem absorber has been further studied by XPS. As observed spectral envelops of Ti2p, Al2p and C1s were broad in nature they were curve fitted into several component species. Fig. 4.10 shows curve-fitted Ti2p, Al2p and C1s core level spectra of the TiAlC layer deposited at C_2H_2 flow rates of 1.5 sccm and 3.5 sccm. It is observed that $Ti2p_{3/2}$ and $Ti2p_{1/2}$ core level peaks at 458.8 and 464.2 eV along with very low intense peaks at 454.9 and 460.9 eV were observed in the layer deposited with low C_2H_2 flow rate, which corresponds to TiO_2 and TiC, respectively (Dorninique et al., 1994; Restrepo et al., 2010). Further increase in flow rate of C_2H_2 to 3.5 sccm shows the increase in concentration of TiC peak along with decreased intensities of TiO_2 peaks and appearance of very weak Ti_2O_3 peaks. Al2p core level spectra of TiAlC layer deposited with different C_2H_2 flow rates are displayed in Fig. 4.10(b). Intensity of Al_4C_3 peak at 73.7 eV is observed to increase with an increase in C_2H_2 flow rate (Beng et al., 1991; Chang et al., 1996). The C1s core level spectrum of the layer deposited at C_2H_2 flow rate of 1.5 sccm shows two peaks centered at 284.6 and 285.8 eV, which represent carbon contamination in the layer and a weak peak centered at 289.1 eV, which indicates O−C=O bonds on the surface of the layer (Antonucci et al., 1994; Maksym et al., 2007). The C1s core level spectrum of the layer, deposited at 3.5 sccm flow rate shows three peaks similar to film deposited at C_2H_2 flow rate of 1.5 sccm along with one extra peak centered at 282.3 eV, indicating the presence of TiC in the layer as shown in Fig. 4.10(c) (Restrepo et al., 2010). It is clear from the XPS studies that increase of C_2H_2 flow rate increases the carbon concentration in the layer. These observations are further confirmed by XPS chemical composition data, which show an increase in carbon concentration from 38 at.% to 46 at.% with C_2H_2 flow rate (1.5 sccm and 3.5 sccm). It is known that change in the carbon concentration affects the electrical properties of the layer (Gulbinski et al., 2005). In order to confirm the effect of carbon concentration on the layer, the resistance of the layer was

measured by using two probe method. The layers deposited at C_2H_2 flow rates of 1.5 sccm and 3.5 sccm show the electrical resistance of ~89 Ω and 47 KΩ, respectively.
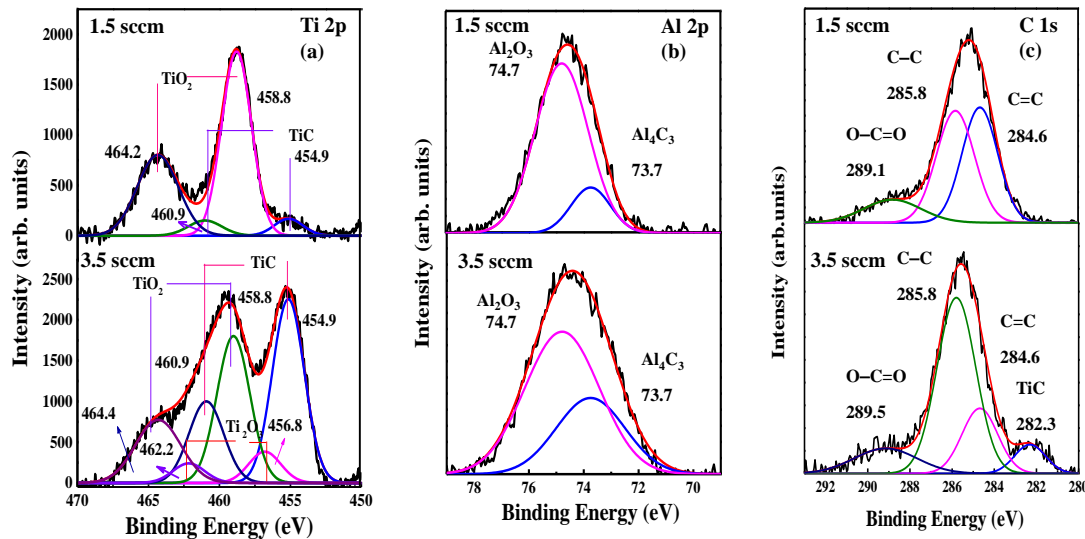
Figure 4.10: XPS of: (a) Ti2p, (b) Al2p and (c) C1s core level spectra of the TiAlC layer with different C_2H_2 flow rates.

Gulbinski et al. also have reported that increase of carbon concentration increases the resistivity of the TiC layer, which indicates the formation of over stoichiometry layer from under-stoichiometry layer (Gulbinski et al., 2005). In the present study also, the XPS data further confirm the increase of carbon concentration with excess of C_2H_2 flow rate. The change in layer from under-stoichiometry to over-stoichiometry also affects the optical properties of the layer (see Fig. 4.1(a)). A shift in the reflectance minimum towards higher wavelength with increased C_2H_2 flow rate indicates a decrease of metallic nature, which is consistent with the XPS data.

The XPS of TiAlCN layer have been studied in order to know the effect of N_2 flow rate on the layer. Curve fitted Ti2p, Al2p and N1s core level spectra of TiAlCN layer with N_2 flow rates of 6 to 10 sccm are displayed in Fig. 4.11. The spectra show the presence of TiC, TiN and TiO_2 species in both layers (Fig. 4.11(a)). Increase of N_2 flow rate shows the increase in concentration of TiN species in the layer that agrees well with the literature (Restrepo et al., 2010). It may be noted that the intensity of TiC decreases significantly

with increase of N_2 flow rate (Fig. 4.11(a)). This can be attributed to high heat of formation of TiC (−44.1 kcal/mol) as compared to TiN (−80.8 kcal/mol) (Robert et al., 1982). Figs. 4.11(b and c) show Al2p and N1s core level spectra of the TiAlCN layer. The data reconfirm the increase in intensities of TiN and AlN peaks with an increase in nitrogen flow rate.
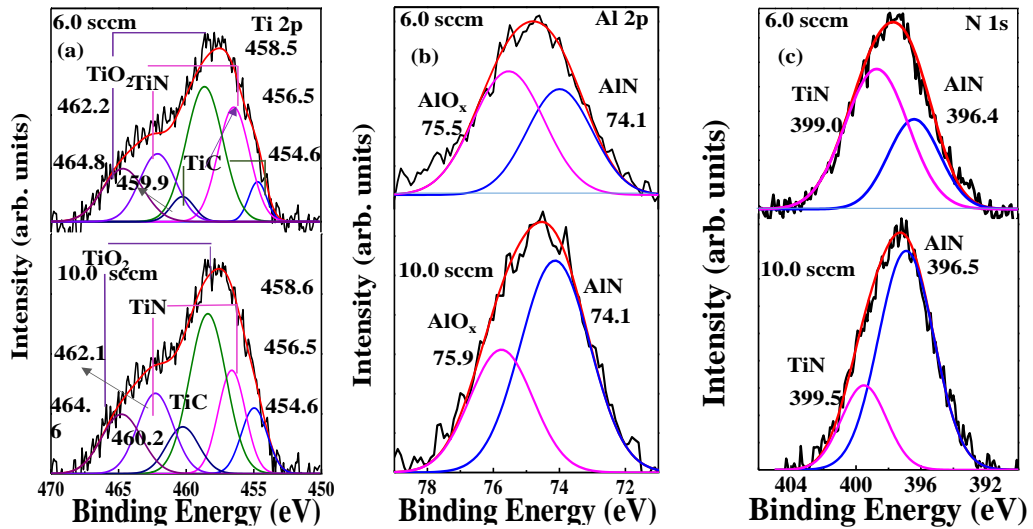
Figure 4.11: XPS of: (a) Ti2p, (b) Al2p and (c) N1s core level spectra of the TiAlCN layer with different N_2 flow rates.

It is important to note that increase in concentration of nitrogen species in the coating decreases the thickness (inset Fig. 4.3(d)) because of target poisoning which is evident from the XPS studies (i.e., increase in the intensity of dielectric AlN layer). Similar XPS studies have been carried out for TiAlSiCN layer (data not presented).

The effect of oxygen flow rate on TiAlSiCO layer has been studied by varying the flow rates from 2 to 6 sccm. Curve-fitted Ti2p, Al2p, O1s and Si2p core level spectrum of TiAlSiCO layer are presented in Fig. 4.12. The Ti2p core level spectrum of the layer deposited at oxygen flow rate of 2 sccm shows the TiC and TiO_2 related peaks (Dorninique et al., 1994; Gao et al., 2003). At higher oxygen flow rate of 6 sccm, the Ti2p core level spectrum does not show any peak corresponding to TiC as shown in Fig. 4.12(a). Increase of oxygen flow rate leads to the formation of TiO_2 because the heat of formation of TiO_2

(-210 kcal/mol) is very low as compared to TiC (-44.1 kcal/mol) (Robert et al., 1982). Al2p core level spectra show peaks corresponding to AlO_x and Al_2O_3 as shown in Fig. 4.12(b) (Beng et al., 1991; Chang et al., 1996). The O1s core level spectra show the increase in intensity of TiO phase with an increase of oxygen flow rate as shown in Fig. 4.12(c).
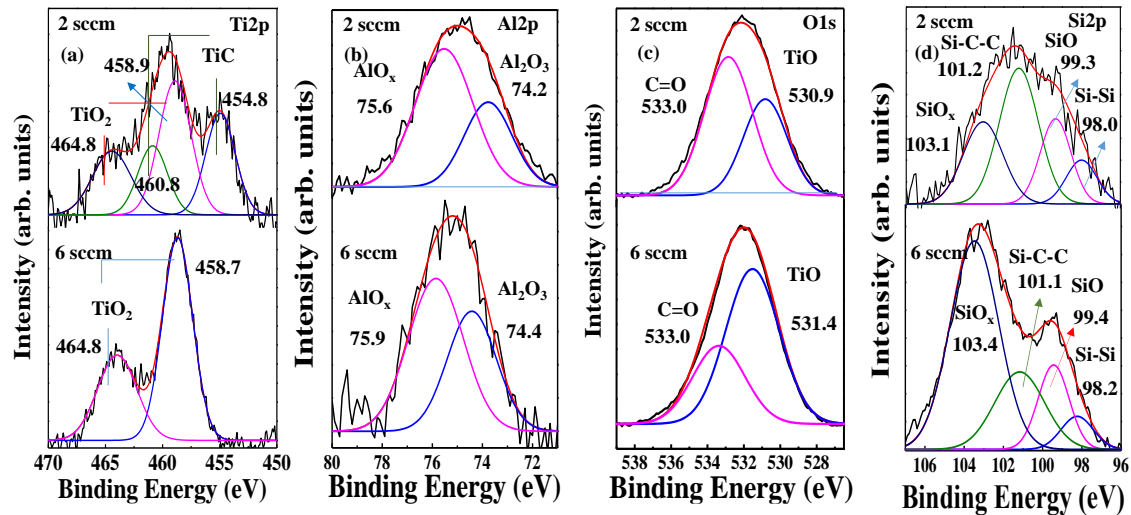
Figure 4.12: XPS of: (a) Ti2p, (b) Al2p, (c) O1s and (d) Si2p core level spectra of the TiAlSiCO layer with different O_2 flow rates.

At low oxygen flow rate of 2 sccm, Si2p core level spectrum clearly shows a broad peak, which is deconvoluted into Si−Si, SiO, SiC_xO_y and SiO_2 (Bell et al., 1988; Morgan et al., 1992; Sirotti et al., 1993; Alfonsetti et al., 1994).

This broad peak splits into two peaks with an increase of oxygen content (Fig. 4.12(d)), indicating that the intensity of un-reactive silicon decreases in the layer with an increase of oxygen flow rate. The XPS data of the 5th layer (TiAlSiO) shown in Fig. 4.13(a-d) for two different oxygen flow rates (6 and 11 sccm) confirm the formation of TiO_2, Al_2O_3 and SiO_2 species as observed from Ti2p, Al2p, Si2p and O1s core level spectra (Beng et al., 1991; Morgan et al., 1992; Dorninique et al., 1994). The presence of oxides helps to increase the thermal stability of the tandem absorber, which is an essential property for solar thermal power applications.
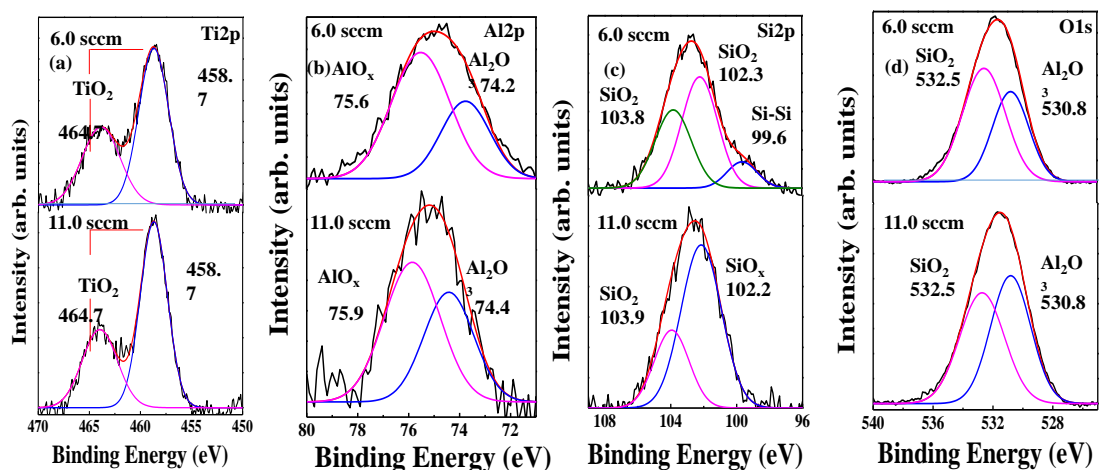
Figure 4.13: XPS core level spectra of: (a) Ti2p, (b) Al2p, (c) Si2p and (d) O1s of the TiAlSiO layer with different O_2 flow rates.

Layer	Element	Binding energy (eV)	Spectral line	Chemical bonding
TiAlC	Ti	454.9	$2p_{3/2}$	Ti-C
		456.8	$2p_{3/2}$	Ti_2O
		458.8	$2p_{3/2}$	TiO_2
		460.9	$2p_{1/2}$	Ti-C
		462.5	$2p_{1/2}$	Ti_2O
		464.4	$2p_{1/2}$	TiO_2
	Al	73.7	2p	Al_4C_3
		74.7	2p	Al_2O_3
	C	282.3	1s	Ti-C
		284.6	1s	C=C
		285.8	1s	C–C
		289.1	1s	O–C=O

TiAlCN	Ti	454.6	$2p_{3/2}$	Ti-C
		456.5	$2p_{3/2}$	Ti-N
		458.5	$2p_{3/2}$	$Ti-O_2$
		460.2	$2p_{1/2}$	Ti-C
		462.1	$2p_{1/2}$	Ti-N
		464.6	$2p_{1/2}$	TiO_2
	Al	74.1	2p	AlN
		75.5	2p	AlO_x
	N	399.2	1s	Ti-N
		396.4	1s	Al-N
TiAlSiCO	Ti	454.8	$2p_{3/2}$	Ti-C
		458.8	$2p_{3/2}$	TiO_2
		460.8	$2p_{1/2}$	Ti-C
		464.8	$2p_{1/2}$	TiO_2
	Al	74.2	2p	Al_2O_3
		75.6	2p	AlO_x
	Si	98.0	2p	Si-Si
		99.3	2p	SiO
		101.2	2p	SiC_XO_Y
		103.1	2p	SiO_x
	O	530.9	1s	Ti-O
		533.0	1s	C=O
TiAlSiO	Ti	458.7	$2p_{3/2}$	TiO_2
		464.7	$2p_{1/2}$	TiO_2
	Al	74.7	2p	Al_2O_3
		75.6	2p	AlO_x
	Si	99.6	2p	Si-Si

		102.2	2p	SiO_x
		103.8	2p	SiO_2
	O	530.8	1s	Al_2O_3
		532.5	1s	SiO_2

Table 4.1: XPS peak assignment of: (i) TiAlC layer deposited at 1.5 sccm and 3.5 sccm C_2H_2 sccm flow rates (Fig. 4.10). (ii) TiAlCN layer deposited at 6.0 sccm and 10.0 N_2 flow rates (Fig. 4.11). (iii) TiAlSiCO layer deposited at 2.0 sccm and 6.0 O_2 flow rates (Fig. 4.12). (iv) TiAlSiO layer deposited at 6.0 sccm and 11.0 O_2 flow rates (Fig. 4.13).

4.4 SUMMARY

➢ TiAlC/TiAlCN/TiAlSiCN/TiAlSiCO/TiAlSiO tandem absorber was designed in such a way that metal volume fraction decreases from bottom layer to the top layer.

➢ The design of the coating has been achieved by controlling the flow rates of the reactive gases and thicknesses (deposition time) of the individual layers. The optimized TiAlC shows the absorptance of 0.761 and emittance of 0.11. Incorporation of TiAlCN and TiAlSiCN layers shows an increase in absorptance to 0.881 at optimized parameters. Adding the semitransparent and antireflection layers (TiAlSiCO, TiAlSiO) to the tandem absorber increases the absorptance from 0.881 to 0.960 ($\varepsilon = 0.15$).

➢ The importance of antireflection layer was studied by annealing the tandem absorber with and without antireflection layer in air at 500°C for 2 h. The results indicate the increase in thermal stability of the coating with antireflection layer.

➢ The overall design of the tandem absorber shows the selective properties of $\alpha =$ 0.960 and $\varepsilon = 0.15$ by careful optimization of the reactive gas flow rates (C_2H_2, N_2, O_2) and thicknesses of each individual layer of the tandem absorber.

➢ The reflectance spectra of the absorber coating prepared at different flow rates indicate a shift in reflectance minima towards higher wavelength with an increase in flow rates of C_2H_2, N_2 and O_2, indicating dielectric nature of the coating prepared at higher concentration.

➢ From XPS studies, increase in concentrations of TiC and Al_4C_3 species is observed, when C_2H_2 flow rate increases from 1.5 sccm and 3.5 sccm in TiAlC layer. Similarly, the concentrations of TiN and AlN increase with an increase in N_2 flow rate from 6 to 10 sccm in TiAlCN layer. TiO_2 is the predominant species when O_2 flow rate is increased from 2 to 6 sccm in TiAlSiCO layer, indicating the oxidation of the layer. TiO_2, Al_2O_3 and SiO_2 intensities increase in TiAlSiO layer with an increase in O_2 flow rate.

➢ This data further confirms the decrease of metallic nature with an increase of reactive gas flow rates. The increase in reactive gas flow rate also leads to a decrease in thickness of the coating due to the target poisoning.

Chapter 5

Optical Properties of TiAlC/ TiAlCN/ TiAlSiCN/ TiAlSiCO /TiAlSiO Tandem Absorber Coatings by Phase Modulated Spectroscopic Ellipsometry

This Chapter is mainly concentrated on the significance of refractive index and extinction coefficient of individual layers of the tandem absorber to achieve selective properties. The angular dependence of the tandem absorber on the selective properties is also studied in detail.

5.1 INTRODUCTION

Recent literature on solar absorbing coatings shows that the selective coatings are prepared by varying the metal volume fraction in a dielectric matrix or multilayers with metal and dielectric alternative layers in the stack, which directly relates to the refractive index of the material (Feng et al., 2015; Wu et al., 2015; Yang et al., 2016). It is worthwhile to note that most of the carbides, oxides, nitrides and silicides have very high melting points, high hardness, improved wear resistance and improved oxidation resistance. The combination of nitrides, carbides and oxides, thus makes an ideal choice to fabricate a high temperature solar absorber coating. In Chapter 3 the design and fabrication of TiAlC/TiAlCN/TiAlSiCN/TiAlSiCO/TiAlSiO tandem absorber with high absorptance and low emittance was discussed. One of the important aspects which needs to be investigated is the optical properties of the component layers of this tandem absorber. This Chapter is majorly concentrated on the study of the refractive indices and extinction coefficients of TiAlC, TiAlCN, TiAlSiCN, TiAlSiCO and TiAlSiO layers by spectroscopic ellipsometry. The phase modulated ellipsometry is used to avoid the slow data acquisition by conventional ellipsometry techniques (Bhattacharyya et al., 2001). In this technique the reflected light is modulated with a frequency of 50 kHz by a photo-elastic modulator and the data acquisition is done by measuring signal over 200 msec. So, it offers accurate and fast data acquisition over a wide wavelength range (300-1200 nm). Moreover, SCOUT

software was used to simulate the reflectance spectra of each successive layers of the tandem absorber deposited on stainless steel substrate, which were compared with the experimental reflectance spectra obtained by spectrophotometry. The change in selective properties of the tandem absorber with different incident angles was also studied.

5.2   EXPERIMENTAL PROCEDURE

To study the refractive indices and extinction coefficients of the TiAlC, TiAlCN, TiAlSiCN, TiAlSiCO and TiAlSiO layers they were deposited on a stainless steel 304 substrate (35 mm × 35 mm) by a semi-industrial four cathode reactive direct current unbalanced magnetron sputtering system. Silicon and glass substrates were also coated for the cross-sectional thickness measurements and electrical resistivity measurements, respectively. The system consists of four high purity (> 99.9%) cathodes such as 2×Ti, 1×Al and 1×Si. Before introducing them inside the sputtering chamber, the stainless steel substrates were polished and thoroughly cleaned with isopropyl alcohol and acetone. The chamber was evacuated up to 8.0×10^{-6} mbar by using a turbomolecular pump and a rotary pump. The deposition of the coatings such as TiAlC, TiAlCN, TiAlSiCN, TiAlSiCO, TiAlSiO takes place in the environment of $Ar+C_2H_2$, $Ar+C_2H_2+N_2$, $Ar+C_2H_2+N_2$ and $Ar+C_2H_2+O_2$, $Ar+O_2$ plasmas, respectively. All layers were deposited at a substrate temperature of 300°C for 2 hrs. The cross-sectional Field Emission Scanning Electron Microscopy (FESEM) was used to calculate the thicknesses of TiAlC, TiAlCN, TiAlSiCN, TiAlSiCO and TiAlSiO layers on silicon substrates and the thicknesses were 2.2 µm, 755 nm, 491 nm, 393 nm, 431 nm, respectively, resulting in growth rates of 18, 6.3, 4.1, 3.3 and 3.5 nm/min. Subsequently, a tandem absorber of TiAlC/TiAlCN/TiAlSiCN/ TiAlSiCO/TiAlSiO with layer thicknesses of 62, 20, 18, 16 and 27 nm, respectively was deposited on stainless steel substrate for the measurement of absorptance and emittance and also to study the angular dependence of the reflectance in both UV-Vis-NIR and IR regions. Solar spectrum reflectometer (Model SSR) of M/s. Devices and Services and Emissometer (model AE) of M/s. Devices and Services were used to measure absorptance and emittance of the coatings. The accuracies of the measured α values are ±2% with a

drift of $\pm1\%$ + 0.003/h and the emissometer has a repeatability of ±0.01 units. For simulation studies, successive layers were deposited on stainless steel substrate.

The reflectance spectra of the tandem absorber and the change in reflectance with the incident angle were studied by varying the incident angle ranging from 8°-68° by UV-Vis-NIR spectrometer (PerkinElmer, Lambda 950) in the wavelength range of 0.3-2.5 µm, with an illumination spot size of 5 mm × 5 mm. A 150 mm Spectralon integrating sphere was used to measure the total reflectance in the UV-Vis-NIR region. SCOUT software was used to simulate the measured reflectance spectra of each layer of the tandem absorber in this wavelength range. Hemispherical directional reflectance spectra in the IR region (1.2-25 µm), at room temperature and in different directions (detection angles θ) from 8° to 70° were acquired using a SOC-100 HDR (Surface Optics Corp.) coupled with a Nicolet 6700 FTIR. The reflected light was polarized before it was sent to the FTIR, to measure the parallel and perpendicular components separately and to avoid polarization bias, as recommended by the manufacturer above 20°.

5.3   RESULTS AND DISCUSSION

5.3.1 Cross-sectional FESEM and EDS studies of individual layers of the tandem absorber

In order to calculate the thickness of the tandem absorber, each layer was deposited on silicon substrates for 2 h under optimized conditions as discussed above.
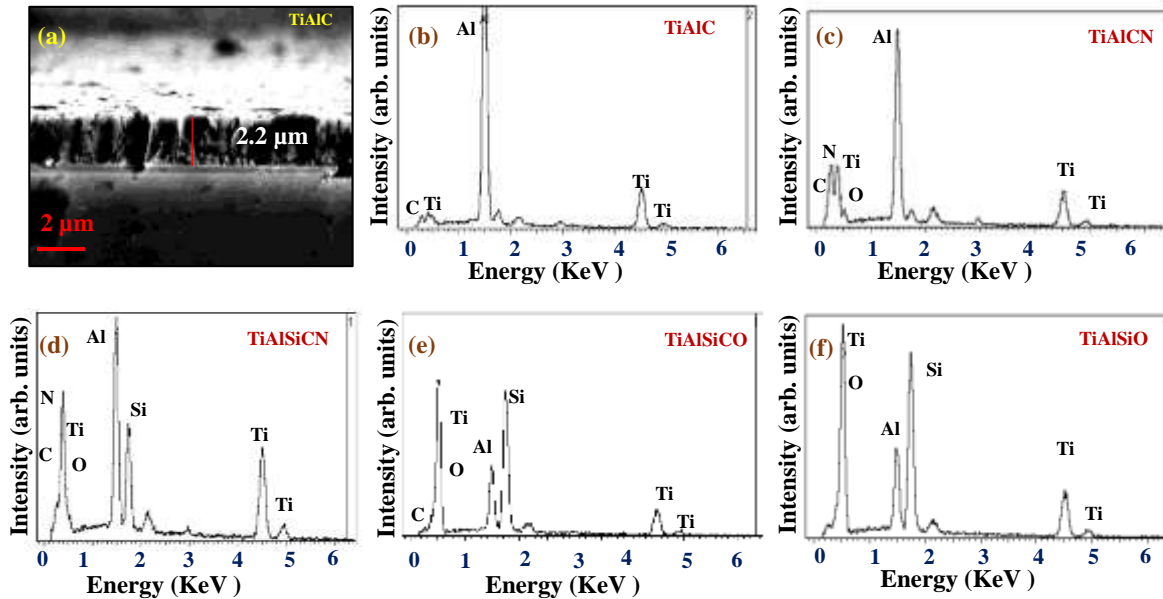
Figure 5.1(a) Cross-sectional FESEM image of the TiAlC layer deposited on Si substrate; and EDS spectra of each individual layer of the tandem absorber deposited on Si substrate: (b) TiAlC (c) TiAlCN (d) TiAlSiCN (e) TiAlSiCO and (f) TiAlSiO.

These samples were fractured and the thicknesses of the each layer were calculated from the cross-sectional FESEM images. A typical cross-sectional FESEM image of the TiAlC layer is shown in Fig. 5.1(a). FESEM data of TiAlC coating shows predominantly columnar microstructure, which diminishes for TiAlCN, TiAlSiCN, TiAlSiCO and TiAlSiO layers (the FESEM images of other layers are not shown). These results indirectly indicate a transition from nanocrystalline to an amorphous phase from first layer to the last layer. The thicknesses of TiAlC, TiAlCN, TiAlSiCN, TiAlSiCO, TiAlSiO layers were 2.2 μm, 755 nm, 491 nm, 393 nm, 431 nm, respectively, resulting in growth rates of 18, 6.3, 4.1, 3.3 and 3.5 nm/min. The thicknesses of the each individual layer decreases from TiAlC layer to TiAlSiO layer deposited for same duration. This is attributed to target poisoning due to reactive sputtering in N_2 and O_2 atmospheres. Especially, when the O_2 is added to the sputtering system the growth rate decreases significantly, which is consistent with the literature (Waite et al., 2007). Elemental analysis of individual layers of the tandem

absorber was carried by the Energy Dispersive Spectroscopy (EDS). The EDS spectra of each individual layers (Figs. 5.1b-f) did not show significant impurities in the deposited layers. EDS data shows high aluminum content for the first two layers, indicating that the coatings are expected to have high oxidation resistance. At higher temperatures aluminum gets oxidized and forms Al_2O_3, which acts as passivation for the coating. The fourth and fifth layers show high silicon content. The presence of silicon in the layers increases the thermal stability of the coating. The detailed elemental composition of each individual layer of the tandem absorber coating is shown in Table 5.1.

Layer	Ti (at. %)	Al (at. %)	Si (at. %)	C (at. %)	N (at. %)	O (at. %)	Total (at. %)
TiAlC	20.53	40.22	--	35.27	--	3.99	100.0
TiAlCN	6.98	10.47	--	33.88	42.31	6.35	99.99
TiAlSiCN	14.02	8.98	4.95	12.64	53.25	6.16	100.0
TiAlSiCO	7.71	4.90	12.77	4.96	--	69.66	100.0
TiAlSiO	9.85	5.05	12.01	--	--	73.08	99.99

Table 5.1: Detailed elemental composition of each individual layers of the tandem absorber coatings deposited on silicon substrates for 2 h.

5.3.2 AFM studies of each individual layers of the tandem absorber

As discussed in Chapter 3 that the resistivity of the coating increases from TiAlC to TiAlSiO layer due to a decrease in the metal volume fraction from first to the last layer. This decrease in metal volume fraction decreases the refractive indices and thicknesses from layer 1 to layer 5. Crystalline structure shows higher refractive index than the amorphous nature (Pearce et al., 2012). Fig. 5.2. shows the surface roughness of individual layers of the tandem absorber deposited on Si substrate for 2 h. It is apparent from Fig. 5.2(a) that the TiAlC layer shows the highest Rms value of 2.4 nm due to its columnar structure. A decrease in the surface roughness from TiAlC to TiAlSiO layer was observed. This decrease in surface roughness of the each individual layer is attributed to diminishing

of crystalline nature to amorphous (Fig. 5.2(b-f)). The smooth surface of the TiAlSiO layer clearly exhibits its amorphous nature (Fig. 5.2(e)). This data is consistent with the XRD data of the layers presented in Chapter 3 (Fig. 3.5(a)).
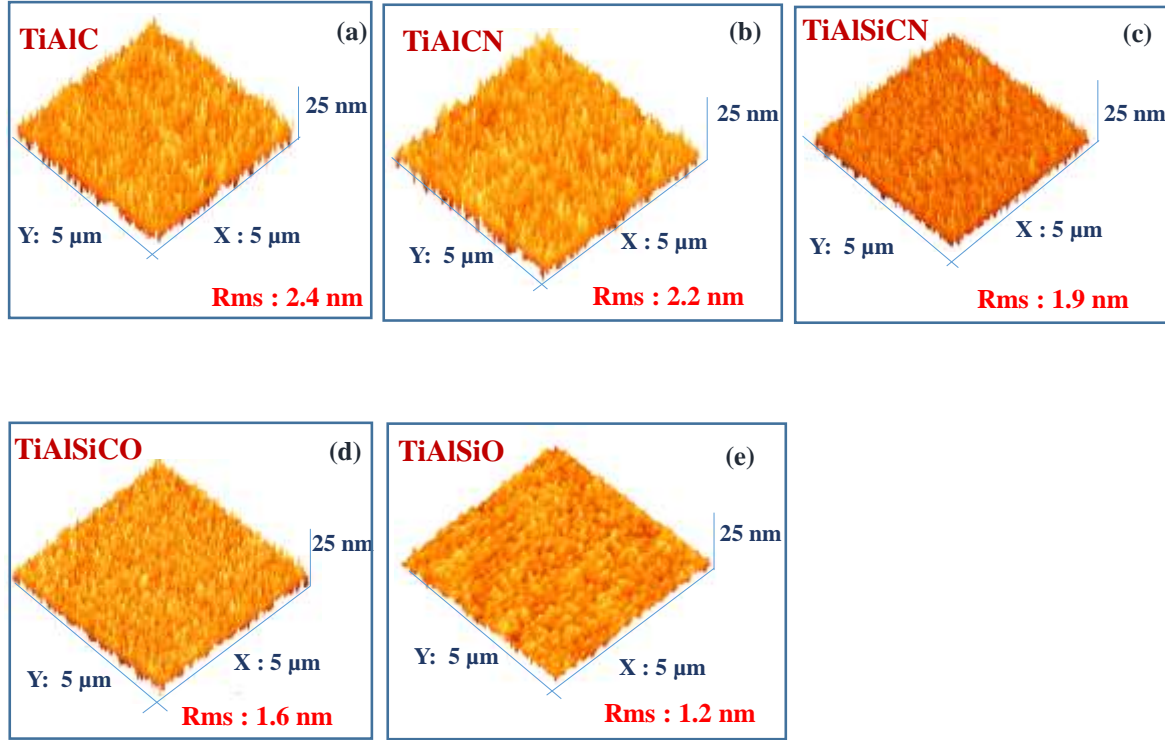
Figure 5.2: AFM images of each individual layers of the tandem absorber: (a) TiAlC, (b) TiAlCN, (c) TiAlSiCN, (d) TiAlSiCO and (e) TiAlSiO.

5.3.3 Optical properties of individual layers of the tandem absorber

The resistivity of the individual layers deposited on glass substrate was measured using a four probe method. A significant difference was indeed observed in the resistivity of the first three layers ($\rho_{TiAlC} = 5 \times 10^{-4}\,\Omega$ cm, $\rho_{TiAlCN} = 7527.2 \times 10^{-4}\,\Omega$ cm, $\rho_{TiAlSiCN} = 80909 \times 10^{-4}\,\Omega$ cm) as compared with the fourth ($\rho_{TiAlSiCO} = 2.4690 \times 10^{4}\,\Omega$ cm) and fifth layers ($\rho_{TiAlSiO} = 3.4 \times 10^{4}\,\Omega$ cm). This change in resistivity of each individual layer plays a major role to achieve the selective properties of TiAlC/TiAlCN/TiAlSiCN/ TiAlSiCO/TiAlSiO (62/20/18/16/27 nm) the tandem absorber (viz., high absorptance of 0.961 and low emittance of 0.15 at 82°C on stainless steel substrate), as discussed in the

Chapter 3. The increase in the resistivity indicates that the metallic nature decreases from the first to the fifth layer.

The phase modulated spectroscopic ellipsometry measures the change in polarization state of the reflected light from a sample surface such as (Bhattacharyya et al., 2004; Azzam et al., 1977; Sahoo et al., 2003; Biswas et al., 2008)

$$\rho = \frac{r_p}{r_s} = \tan\psi \, \exp(i\Delta) \qquad (5.1)$$

where r_p: reflection coefficient of the 'p' component of the electric field

$\quad\quad$ r_s: reflection coefficient of the 's' component of the electric field.

The measured ψ and Δ spectra from ellipsometry were fitted with theoretically generated spectra considering an appropriate dispersion formula of the material.
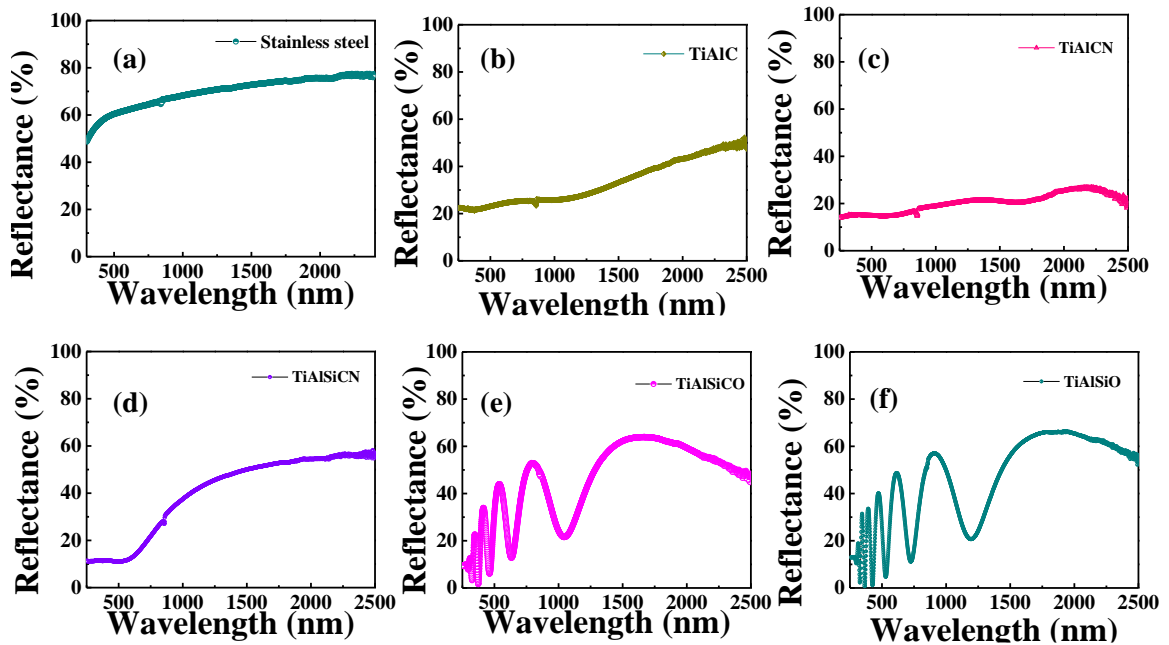
Figure 5.3: UV-Vis-NIR reflectance spectra of: (a) stainless steel substrate; (b) TiAlC layer; (c) TiAlCN layer; (d) TiAlSiCN layer; (e) TiAlSiCO layer; (f) TiAlSiO layer.

In order to achieve more realistic results, the optical constants of stainless steel substrate were measured and these data were used for ellipsometric data fitting.

Fig. 5.3. shows the UV-Vis-NIR reflectance spectra of TiAlC, TiAlCN, TiAlSiCN, TiAlSiCO and TiAlSiO layers along with the reflectance data of stainless steel. The SS

substrate shows high reflectance in the whole solar spectrum region as displayed in Fig. 5.3(a). Compared to bare SS reflectance data, the reflectance spectrum of TiAlC layer (Fig. 5.3(b)) shows the overall decrease in reflectance, indicating its absorbing nature. Decrease in reflectance spectrum was observed in TiAlCN layer, especially at wavelengths ranging from 1000-2500 nm as shown in Fig. 5.3(c), demonstrating that the layer is also absorbing. The TiAlSiCN layer shows a constant reflectance up to a wavelength of 545 nm, after which a drastic increase in reflectance with wavelength was observed as shown in Fig. 5.3(d), indicating its semi-absorbing nature. In the case of TiAlSiCO and TiAlSiO layers (Fig. 5.3(e and f)) the reflectance spectra show the high reflectance in the whole wavelength range, which implies that these layers are not absorbing in nature and act as intermediate and antireflection layers. It may be noted that as the coating thickness for TiAlSiCO and TiAlSiO layers was smaller (hence more transmitting in nature) compared to TiAlC layer, the reflectance spectra were affected by the substrate as the light could be partially reflected back from the substrate. These data clearly indicate that the first three layers (viz., TiAlC, TiAlCN and TiAlSiCN) act as absorbing layers, and TiAlSiCO and TiAlSiO are intermediate and antireflection layers. The first three layers' ellipsometric experimental data were fitted with the Cauchy's absorbent dispersion relation given by (Sahoo et al., 2003; Biswas et al., 2008)

$$n(\lambda) = A + \frac{10^4 \times B}{\lambda^2} + \frac{10^9 \times C}{\lambda^4} \qquad (5.2)$$

$$k(\lambda) = D + \frac{10^4 \times E}{\lambda^2} + \frac{10^9 \times F}{\lambda^4} \qquad (5.3)$$

where A, B, C, D, E and F are coefficients for fitting parameters

λ is the wavelength in nm.

Parameter	TiAlC layer	TiAlCN layer	TiAlSiCN layer
A	2.282	2.432	1.822
B	7.289	-9.092*	-7.909*
C	-3.567*	8.256	2.584
D	2.627	1.619	0.682
E	-38.999*	-30.665*	0.778
F	35.940	23.052	0.198

The asterisk * shows the negative value which has no physical meaning but indicates the good values to perform fit on the material.

Table 5.2: Best fit parameters of TiAlC, TiAlCN and TiAlSiCN layers obtained by Cauchy's model.

Figs. 5.4(a-c) show ψ and Δ versus wavelength (ellipsometric spectra) of the TiAlC, TiAlCN and TiAlSiCN layers, respectively, in the wavelength range of 300-1200 nm. These spectra were fitted with the Cauchy's absorbent dispersion relation and the best fit parameters A, B, C, D, E and F of these layers are displayed in Table 5.2. The TiAlSiCO and TiAlSiO layers are insulating in nature. The importance of TiAlSiCO and TiAlSiO layers is discussed in Chapter 4. The experimental data of ψ and Δ for the TiAlSiCO and TiAlSiO layers were fitted with the Tauc-Lorentz model.
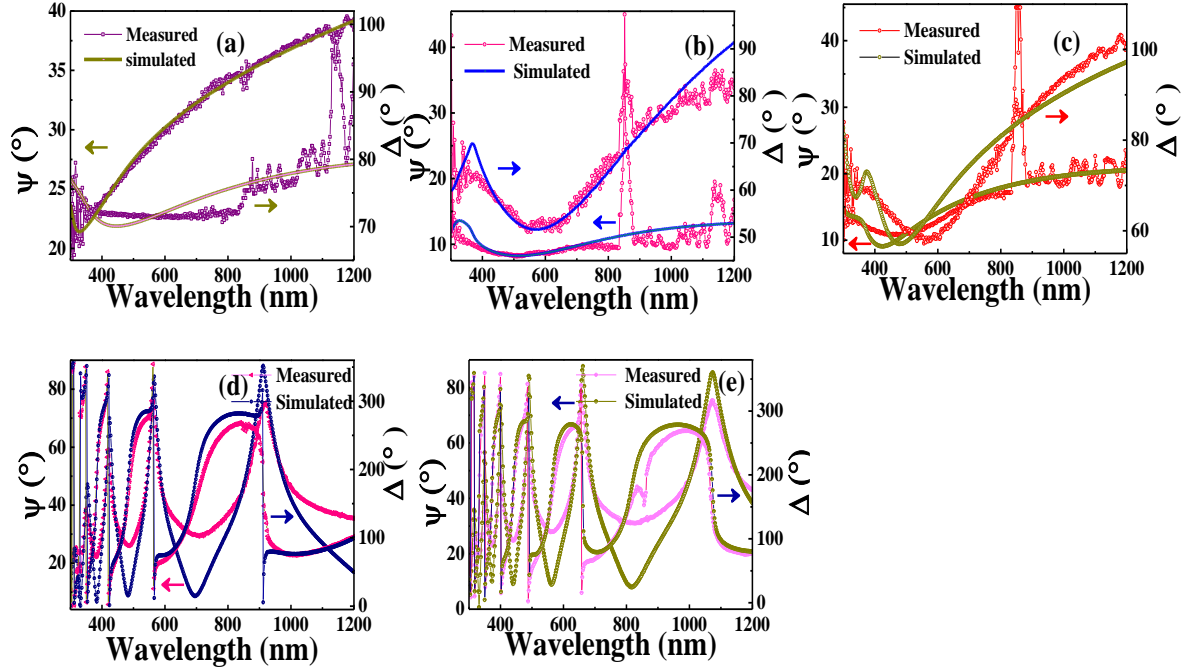
Figure 5.4: Experimental ψ and Δ values obtained by ellipsometry along with the best fitted theoretical curves for: (a) TiAlC; (b) TiAlCN; (c) TiAlSiCN; (d) TiAlSiCO and; (e) TiAlSiO layers.

In 1966, Jellison and Modine developed the Tauc-Lorentz dispersion model by using the Tauc's joint density of states and Lorentz's oscillator. Dielectric function is (Jellison et al., 1996):

$$\tilde{\varepsilon}_{TL} = \varepsilon_{r,TL} + i.\varepsilon_{i,TL} = \varepsilon_{r,TL} + i(\varepsilon_{i,T} \times \varepsilon_{i,L}) \qquad (5.4)$$

$\varepsilon_{i,TL}$ gives the product of the Tauc's imaginary part of the dielectric function $\varepsilon_{i,T}$ with Lorentz $\varepsilon_{i,L}$. Interband transition of Tauc's dielectric function stated above was used to evaluate the band edge as (Jellison et al., 1996):

$$\varepsilon_{i,T}(E > E_g) = A_T.\left[\frac{E-E_g}{E}\right]^2 \qquad (5.5)$$

where A_T is the Tauc coefficient, E is the photon energy and E_g is the optical band gap.

Materials response caused by interband mechanism is given by the imaginary part of the Tauc dielectric function $\varepsilon_{i,T}(E \le E_g) = 0$. Imaginary part of the Lorentz oscillator is (Jellison et al., 1996)

$$\varepsilon_{i,L}(E) = \frac{A_L.E_0.C.E}{(E^2-E_0^2)^2+C^2.E^2} \qquad (5.6)$$

where A_L and C are the strength and broadening terms of the peak, respectively. E_0 is the peak central energy.

Jellison set up a new expression by multiplying equation (5.5) by equation (5.6) (Jellison et al., 1996)

$$\varepsilon_{i,TL}(E) = \varepsilon_{i,L} \times \varepsilon_{i,T} = \begin{cases} \frac{1}{E}\frac{AE_0C(E-E_g)^2}{(E^2-E_0^2)^2+C^2E^2} & for\ E > E_g \\ 0 & for\ E \leq E_g \end{cases} \qquad (5.7)$$

where $A = A_T \times A_L$

The real part of the dielectric function is derived from the Kramers-Kronig integration (Jellison et al., 1996)

$$\varepsilon_r(E) = \varepsilon_r(\infty) + \frac{2}{\pi}.P.\int_{E_g}^{\infty}\frac{\xi.\varepsilon_i(\xi)}{\xi^2-E^2}\ d\xi \qquad (5.8)$$

where P is the Cauchy principal value.

The derivation of previous integrals yields equation (5.9).

$$\varepsilon_{r,TL}(E) = \varepsilon_\infty + \frac{A.\ C.\ a_{ln}}{2\pi\xi^4.\alpha.E_0}.\ln\left[\frac{E_0^2+E_g^2+\alpha.E_g}{E_0^2+E_g^2-\alpha.E_g}\right] - \frac{A}{\pi}.\frac{a_{atan}}{\xi^4.E_0}.\left[\pi - a\tan\left(\frac{2.E_g+\alpha}{C}\right) + \right.$$

$$\left. a\tan\left(\frac{\alpha-2.E_g}{C}\right)\right] + \frac{4.A.E_0E_g(E^2+\gamma^2)}{\pi\xi^4.\ \alpha}\times\left[a\tan\left(\frac{\alpha+2.E_g}{C}\right) + a\tan\left(\frac{\alpha-2.E_g}{C}\right)\right] -$$

$$\frac{A.E_0.C.(E^2+E_g)}{\pi.\xi^4.E}.\ ln\left(\frac{|E-E_g|}{E+E_g}\right) + \frac{2.A.E_0.C}{0\pi.\xi^4}\times E_g.ln\left[\frac{|E-E_g|.(E+E_g)}{\sqrt{(E_0-E_g)+E_g^2.C^2}}\right] \qquad (5.9)$$

where
$$\begin{cases} a_{ln} = (E_g^2 - E_0^2).E^2 + E_g^2.C^2 - E_0^2.(E_0^2 + 3.E_g^2) \\ a_{atan} = (E^2 - E_0^2)(E_0^2 + E_g^2) + E_g^2.C^2 \\ \alpha = \sqrt{4.E_0^2 - C^2} \\ \gamma = \sqrt{E_0^2 - C^2/2} \\ \xi^4 = (E^2 - \gamma^2)^2 + \alpha^2.C^2/4 \end{cases}$$

The optical properties such as refractive index and extinction coefficient of these insulating layers were obtained by the best fit of the ellipsometric spectra by the Tauc-Lorentz model as shown in Fig. 5.4(d and e). Table 5.3 illustrates the best fit parameters obtained by Tauc-Lorentz model for TiAlSiCO and TiAlSiO layers.

Parameter	TiAlSiCO layer	TiAlSiO layer
E_g (eV)	1.315	1.056
ε (Inf)	1.545	1.325
A (eV)	4.973	5.047
C (eV)	5.412	0.401

Table 5.3: Best fit parameters of TiAlSiCO and TiAlSiO layers obtained by Tauc-Lorentz model.

The refractive indices and extinction coefficients of all the individual layers were then calculated by applying the aforementioned dispersion formulae with the parameters in Tables 5.2 and 5.3 deduced from the best fit between experimental and simulated spectra. The refractive index of the stainless steel substrate is displayed in Fig. 5.5(a). Fig. 5.5(b) shows the refractive index of each layer. It is clear from the figure that the refractive index of the individual layers decreases from TiAlC layer to TiAlSiO layer (above 450 nm). For example, the refractive indices were 2.517, 2.155, 1.547, 1.485 and 1.442 at λ = 500 nm for TiAlC, TiAlCN, TiAlSiCN, TiAlSiCO and TiAlSiO, respectively (Fig. 5.5(c)). The decrease in refractive index with wavelength was observed for TiAlSiCO and TiAlSiO layers, indicating that these layers are dielectric in nature (Fig. 5.5(b)). The extinction coefficients of TiAlC, TiAlCN, TiAlSiCN, TiAlSiCO and TiAlSiO layers are shown in Fig. 5.5(d).
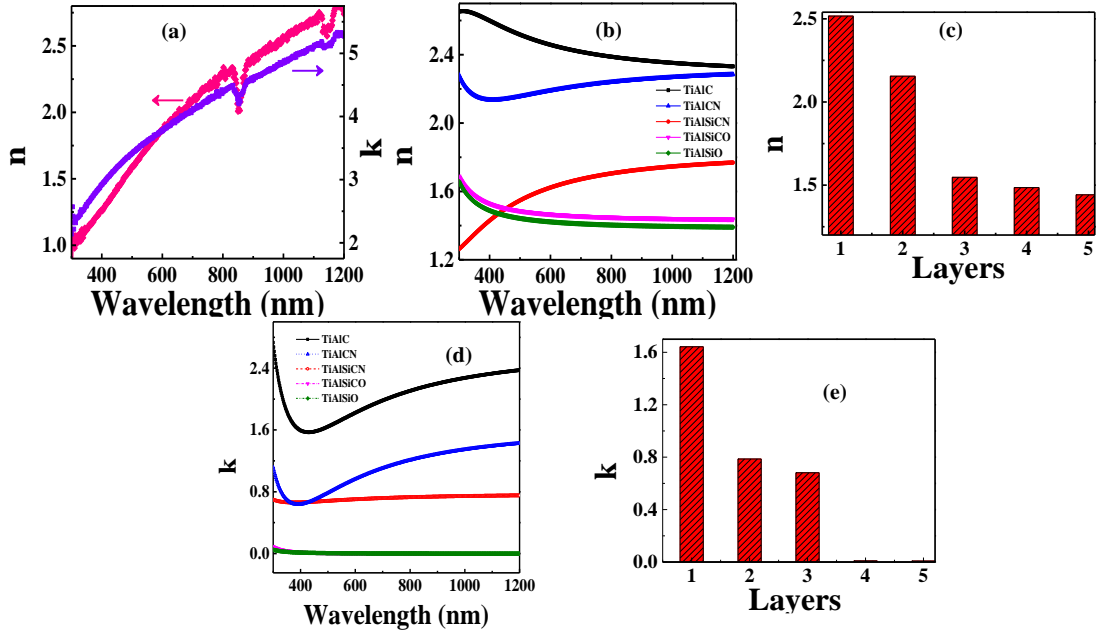
Figure 5.5: (a) Refractive index and extinction coefficient of stainless steel substrate as a function of wavelength; (b) refractive indices of TiAlC, TiAlCN, TiAlSiCN, TiAlSiCO and TiAlSiO layers as a function of wavelength and (c) '*n*' at 500 nm; (d) extinction coefficients of each layer as a function of wavelength and (e) '*k*' at 500 nm.

The TiAlC layer shows the highest extinction coefficient of 1.642 at a wavelength of 500 nm, whereas TiAlCN and TiAlSiCN layers show an extinction coefficient of 0.786 and 0.681, respectively. The extinction coefficient was almost zero for TiAlSiCO and TiAlSiO layers, representing that these layers are non-absorbing layers and act an intermediate and antireflection layers. The extinction coefficients of the five layers at 500 nm are displayed in Fig. 5.5(e).

As we know that extinction coefficient is directly proportional to the absorption coefficient, that is (Heavens et al., 1965; Barshilia et al., 2008)

$$\propto = \frac{4\pi k}{\lambda} \qquad (5.10)$$

where α is the absorption coefficient, k is the extinction coefficient and λ is the wavelength. The absorption coefficients of TiAlC, TiAlCN, TiAlSiCN layers were also calculated by

using the above formula and the data is shown in Fig. 5.6. TiAlC layer shows the highest absorption coefficient compared to the other two layers, thus confirming that TiAlC layer is the major absorbing layer (Fig. 5.6(a)). The absorption coefficient decreases for TiAlCN and TiAlSiCN layers as shown in Fig. 5.6(b and c). The absorption coefficients of the TiAlSiCO and TiAlSiO layers have not been plotted because the extinction coefficients of these layers were almost zero. It directly indicates that these layers are not absorbing in nature. This data further proves that TiAlSiCO and TiAlSiO layers act as an intermediate and antireflection layers, respectively.
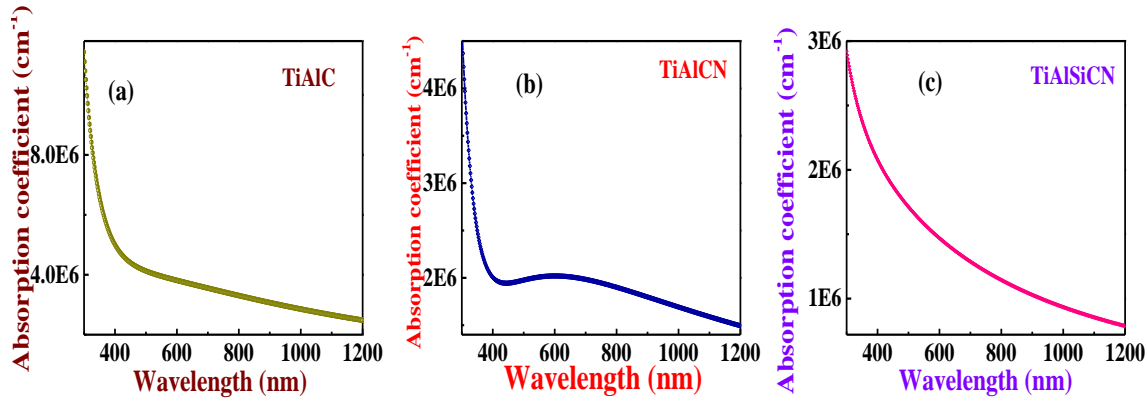
Figure 5.6: Absorption coefficients of: (a) TiAlC; (b) TiAlCN; and (c) TiAlSiCN layers.

5.3.4 Comparison of simulated and experimentally obtained reflectance spectra by SCOUT software

Once the optical constants of TiAlC, TiAlCN, TiAlSiCN, TiAlSiCO and TiAlSiO layers were known, a tandem absorber of TiAlC/TiAlCN/TiAlSiCN/TiAlSiCO/TiAlSiO (62/20/18/16/27 nm) was deposited on stainless steel substrate, the absorptance and emittance of which were 0.961 and 0.15, respectively. Further, successive layers of TiAlC, TiAlCN, TiAlSiCN, TiAlSiCO and TiAlSiO were also deposited on stainless substrate as shown schematically in insets of Fig. 5.7 to study the reflectance spectra. In order to corroborate the experimental results, SCOUT software was used to simulate the reflectance spectra (Wu et al., 2015; Theiss et al., 2015). For this, refractive index (n) and extinction coefficient (k) of each individual layer, as discussed above, were used for the simulation.

98

Fig. 5.7 shows the simulated and experimentally measured reflectance spectra of the stainless steel substrate and their evolution with adding consecutively each of the five individual layers of the tandem absorber. In SCOUT data, the agreement between the simulated and measured spectra was studied by the fit deviation value. If the fit deviation values are less than 0.1, 0.01, 0.001, 0.0001 and 0.00001 they indicate the fit as rejected, bad, acceptable, good and excellent, respectively (Theiss et al., 2015). All simulated reflectance spectra show a low deviation value with the measured ones (Table 5.4).

Stack description	Layer Thickness (nm)*		n	k	R minima (nm)				Deviation
	Exp.	Sim.	λ_{500m}	λ_{500nm}	Sim		Exp.		
					1st	2nd	1st	2nd	
SS	3 mm	3.5 mm	1.580	3.413	-	-	-	-	0.0005695
SS/TiAlC	62	70	2.517	1.642	354	-	307	-	0.0006542
SS/TiAlC/TiAlCN	62/20	70/20	2.155	0.786	365	-	376	-	0.0006381
SS/TiAlC/TiAlCN/TiAlSiCN	62/20/18	70/20/23	1.542	0.681	691	-	584	-	0.0008376
SS/TiAlC/TiAlCN/TiAlSiCN/ TiAlSiCO	62/20/18/16	70/20/23/27	1.485	0	722	-	709	-	0.0007163
SS/TiAlC/TiAlCN/TiAlSiCN/ TiAlSiCO/TiAlSiO	62/20/18/16/ 27	70/20/23/27/32	1.442	0	1464	735	1404	514	0.0008129

Table 5.4: Thicknesses of the individual layers of the tandem absorber used to generate the simulated reflectance spectra in SCOUT, positions of reflectance minima and fit deviation with experimentally measured spectra.

*There are some differences in layer thicknesses deduced from the experimental and the simulated data. This difference may be attributed to various reasons such as fluctuations in the deposition rates and also the differences in the 'n' and 'k' values of the thicker and thinner layers as the thin films will contain more of defects and pinholes compared to their bulk counterparts.

The simulated reflectance spectrum of stainless steel shows the best agreement with the measured spectrum (Fig. 5.7(a)). Fig. 5.7(b) shows reflectance spectra of the TiAlC layer of the tandem absorber. The obtained simulated spectrum of the layer shows good agreement with the measured spectrum.
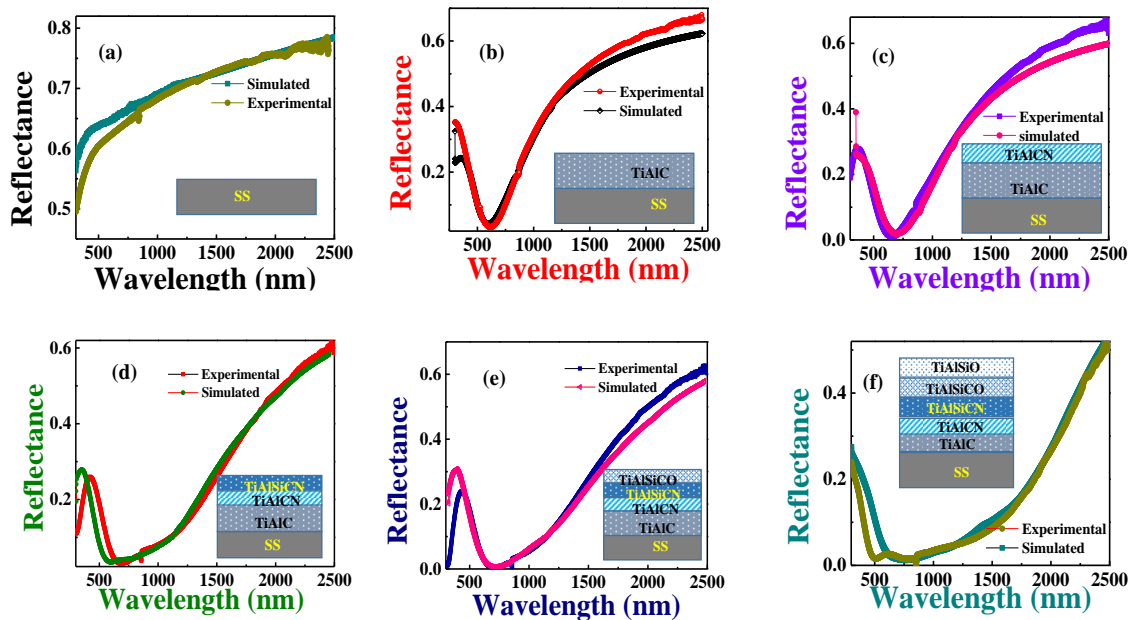
Figure 5.7: Experimentally obtained reflectance spectra of the tandem absorber fitted with the simulated spectra obtained by SCOUT software: (a) stainless steel substrate; (b) TiAlC; (c) TiAlC/TiAlCN; (d) TiAlC/TiAlCN/TiAlSiCN; (e) TiAlC/TiAlCN/TiAlSiCN/ TiAlSiCO; and (f) TiAlC/TiAlCN/TiAlSiCN/TiAlSiCO/TiAlSiO tandem absorber. The thicknesses were: 62, 20, 18, 16 and 27 nm, respectively for TiAlC, TiAlCN, TiAlSiCN, TiAlSiCO, TiAlSiO layers.

In case of TiAlC/TiAlCN and TiAlC/TiAlCN/TiAlSiCN multilayers, the simulated reflectance spectra also show a good agreement with the position of interference maxima and minima in the measured reflectance spectra, as shown in Fig. 5.7(c and d). When

incorporating the intermediate and antireflection layers to the tandem absorber, the simulated reflectance spectra are also well fitted with the measured spectra, as shown in Fig. 5.7(e and f). The detailed parameters used to simulate the measured reflectance spectra with SCOUT are shown in Table 5.4.

5.3.5 Angular absolute reflectance studies of the tandem absorber in solar and IR regions

The change in incidence angle of the incident light affects the absorptance of the selective coatings, which directly impacts their efficiency (Dan et al., 2016). The effect of change in incident angle on selective properties of the tandem absorber was therefore studied by UV-Vis-NIR and FTIR spectroscopy. The TE (*s*) polarization and TM (*p*) polarization reflectance of the tandem absorber were measured at different incidence angles (8° − 68°) as a function of wavelength. The TM reflectance spectra (R_p) shown in Fig. 5.8(a) decrease in the visible region with incident angles from 8° to 58°. The reflectance is less than 10% at wavelength ranging from 350-1500 nm. Further increase in the incident angle to 68° causes the overall reflectance spectrum to increase for TM polarization. Figs. 5.8(b and c) show that the TE (R_s) and average ($R_{avg} = (R_p+R_s)/2$) spectral reflectance values of the tandem absorber are almost constant up to 38° and then increase with the incident angle.
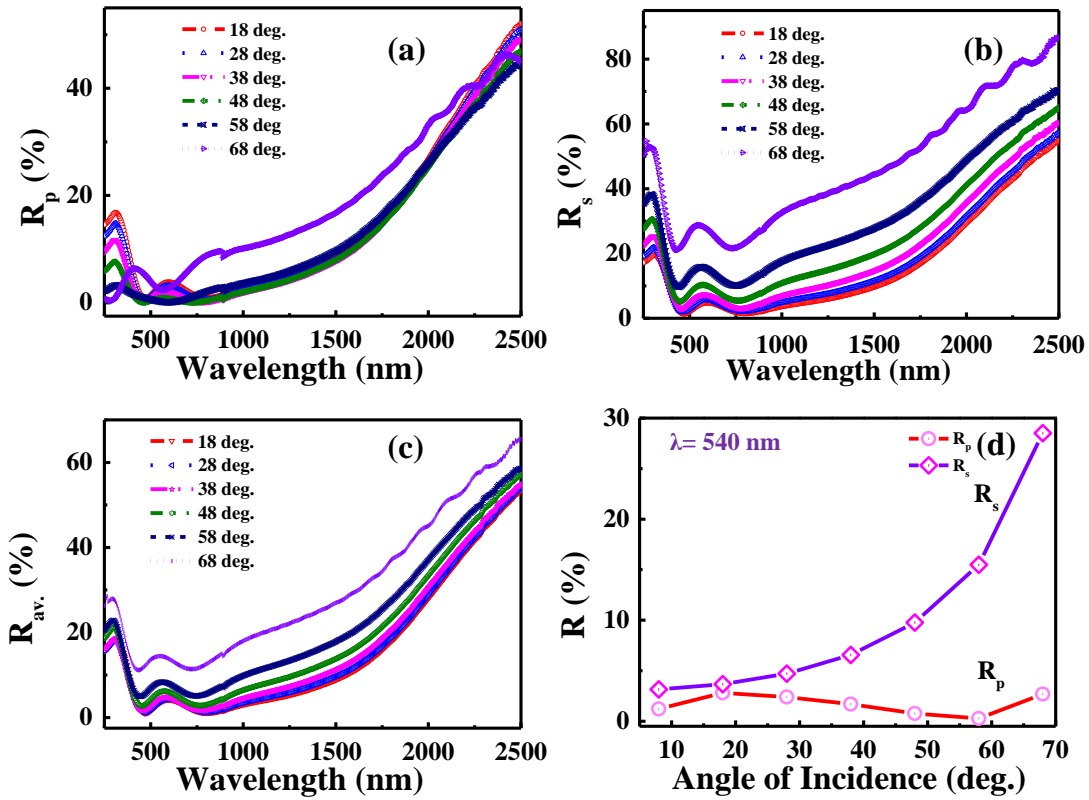
Figure 5.8: Angular absolute reflectance studies of the tandem absorber in the UV-Vis-NIR region for: (a) TM polarization (R_p); (b) TE polarization (R_s); (c) Average reflectance R = (R_p+R_s)/2; (d) change in reflectance at 540 nm with incident angle.

The average reflectance spectra of the tandem absorber, (Fig. 5.8(c)) confirm that the designed tandem absorber shows the wide angle of solar absorption with different incident angles ranging from 8° to 58°. The change in reflectance at 540 nm with incident angle for the two polarizations is shown in Fig. 5.8(d), which more clearly demonstrates almost constant solar absorption up to 58°.
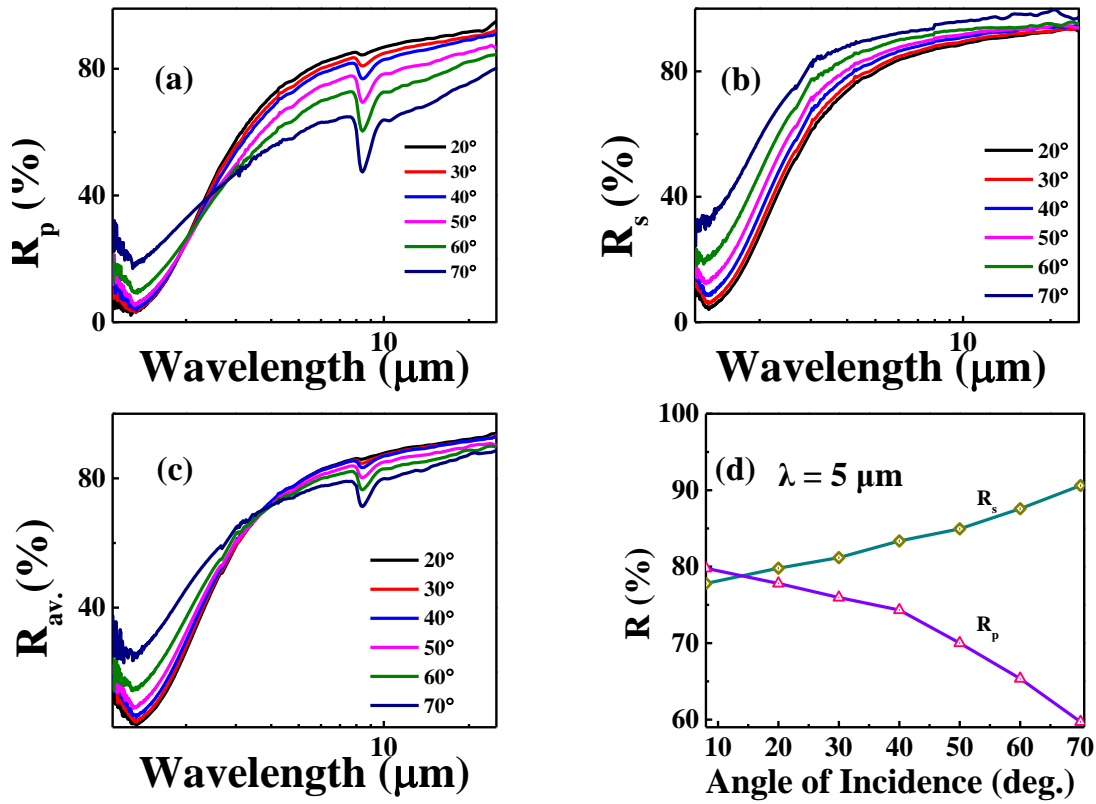
Figure 5.9: Angular reflectance studies of the tandem absorber in the IR region: (a) TM polarization (R_p); (b) TE polarization (R_s); (c) Average reflectance $R_{avg} = (R_p+R_s)/2$; (d) change in reflectance with incident angles at 5.0 μm.

As a complement, hemispherical directional reflectance spectra were also acquired in the IR region (1.2 to 25 µm), in different directions (detection angles θ) from 8° to 70°. Fig. 5.9(a) illustrates the parallel polarized reflection only (R_p). An increase in reflectance with the angle was observed up to 3 µm. Above this wavelength, it decreases with increasing angle. A peak of lower reflectance was observed at 8.5 µm, due to the Berreman effect, which is usually attributed to the LO-mode of Al-O bonds of Al_2O_3 (Berreman et al., 1963; Kaltchev et al., 1999). In the perpendicular polarization signal (R_s, Fig. 5.9(b)), the reflectance increases with increasing the angle. Consequently, the average reflectance ((parallel + perpendicular)/2, (Fig. 5.9(c)) shows an increase with the angle up to $\lambda < 3$ µm and then it decreases with increasing angle. Overall, no drastic change in reflectance was observed up to an angle of 40°. The change in parallel and perpendicular reflectance signals at 5 µm with the detection angle is shown in Fig. 5.9(d). This data clearly supports that there is no significant change in emittance with the incident angle.

In summary, we have studied in detail the optical properties of the TiAlC, TiAlCN, TiAlSiCN, TiAlSiCO and TiAlSiO layers for high temperature spectrally selective application. The roles of refractive index and extinction coefficient of each individual layers have been studied to design and develop a tandem absorber with selective properties. Further, it has been shown that gradient of refractive index from the substrate to the top layer helps in achieving very high absorptance. The results of the present work have further been corroborated with the simulation data achieved using SCOUT software. The experimental and simulated data match well, thus, confirming our strategy for the design of the solar absorber coating.

5.4. SUMMARY

> Thick layers of TiAlC, TiAlCN, TiAlSiCN, TiAlSiCO and TiAlSiO were deposited on stainless steel substrate and their refractive indices and extinction coefficients were studied by spectroscopic ellipsometry technique.

> Cauchy's absorbent model was used to fit TiAlC, TiAlCN, TiAlSiCN layers, whereas Tauc-Lorentz model was employed for TiAlSiCO and TiAlSiO layers.

> At 500 nm, the refractive indices of TiAlC, TiAlCN, TiAlSiCN, TiAlSiCO and TiAlSiO layers were 2.51, 2.15, 1.54, 1.48 and 1.44, respectively.

> The TiAlC layer shows the highest extinction coefficient value, indicating that the TiAlC plays a major role as an absorbing layer.

> The extinction coefficient values decrease from TiAlC (bottom) to TiAlSiO (top) layers. The k values of TiAlSiCO and TiAlSiO were almost zero, confirming that these layers are intermediate and antireflective in nature.

> A solar selective tandem absorber of TiAlC/TiAlCN/TiAlSiCN /TiAlSiCO/TiAlSiO (62/20/18/16/27 nm) deposited on stainless steel substrate shows an absorptance of 0.961 with an emittance of 0.15 at 82°C.

> SCOUT software was utilized to simulate the experimental reflectance spectra by using the appropriate thickness, refractive index and extinction coefficient of each layer of the tandem absorber.

> The simulated spectra were in good accordance with the experimental spectra. Furthermore, the average reflectance spectra of the tandem absorber show a low reflectance in the solar spectrum region over a wide range of angles from 8° to 58°.

> No significant change in emittance of the tandem absorber was observed for angles below 50° in the infrared range either. The tandem absorber therefore keeps its selective properties at a wide range of incidence angles.

Chapter 6

Measurement of High Temperature Emissivity and Photothermal Conversion Efficiency of TiAlC/TiAlCN/TiAlSiCN/TiAlSiCO/TiAlSiO Spectrally Selective Coating

The thermal emittance of the tandem absorber at higher temperatures (80°C–500°C) was studied in detail. Adhesion of the coating and effect of annealing temperature on roughness of the tandem absorber was also analyzed in this Chapter.

6.1   INTRODUCTION

As has been discussed previous Chapters the spectrally selective coatings are used for efficient photo-thermal conversion. The high absorptance of the coating increases the temperature of the substrate significantly when exposed to concentrated solar radiation and as per Wien's displacement law ($\lambda_{max} =$ b/T, where T is the absolute temperature in K and 'b' is a constant) the substrate must start emitting thermally after reaching at an equilibrium. Radiation in the region of the electromagnetic spectrum from 0.2-100 µm is called thermal re-radiation and is emitted by all the substances by virtue of their temperature. The thermal re-radiation losses are determined by the thermal emissivity (ε) of the substrate surface.

The amount of radiation emitted by the object depends upon its emissivity (Moghaddam et al., 2005; Campo et al., 2008). Emissivity is a dimensionless property (number between 0 and 1), which is defined as an amount of radiation emitted from an object to that radiated from a blackbody at the same temperature. Stefan – Boltzmann law states that the amount of thermal energy radiated by a blackbody radiator per second per

unit area is proportional to the fourth power of the absolute temperature (DeWitt et al., 1988; Modest et al., 2003; Moghaddam et al., 2005).

$$J = \sigma T^4 \qquad (6.1)$$

where σ is a constant.

For objects other than ideal blackbody radiators, the law is expressed as:

$$J = \varepsilon \sigma T^4 \qquad (6.2)$$

where ε is the emissivity of the object.

The emittance considerably changes with a film of impurities or surface roughness or the presence of oxide layer on the surface. Thick oxide layers show higher emittance compared to polished fresh surface (Incropera et al., 2002). Emittance also depends upon the roughness of the substrate, which affects the reflectance as described below:

$$R_r = R_p \exp\left(\frac{-4\pi\sigma}{\lambda}\right) \qquad (6.3)$$

where R_r and R_p are the reflectances for a rough and polished surfaces, respectively, σ is the root-mean-square roughness and λ is the wavelength (Sibin et al., 2015).

As per the Kirchhoff's law, for a body in thermal equilibrium:

$$\alpha_\lambda = \varepsilon_\lambda \qquad (6.4)$$

The conservation of energy requires:

$$\alpha_\lambda + R_\lambda + T_\lambda = 1 \qquad (6.5)$$

For an opaque surface, $T_\lambda = 0$ and hence:

$$\alpha_\lambda = 1 - R_\lambda \qquad (6.6)$$

Using the above Kirchhoff's law:

$$\alpha_\lambda = \varepsilon_\lambda = 1 - R_\lambda \qquad (6.7)$$

where R_λ is the total (spectral + diffuse) spectral reflectance at wavelength λ. Therefore, Eqs. (6.3) and (6.7) clearly show that emittance increases with an increase in surface roughness. This indicates that emittance not only depends on materials property but also strongly depends on surface conditions (Brandt et al., 2008). Further, if the reflectance of the substrate is high in the IR region then its effective thermal emissivity will be low. In

general, metals are poor emitters of thermal infra-red radiation. In other words, by minimizing the emissivity of the metal substrate one can increase the efficiency of the photo-thermal conversion. The seemingly contradictory requirement of having a good absorber that is simultaneously a poor emitter requires the design of a spectrally selective coating.

In this Chapter, the detailed studies was carried out on the directional thermal emittance of the tandem absorber deposited on stainless steel, calculated from the spectral reflectance measured in the spectral range of 1.2 - 25 μm at different temperatures, on samples heated up to 500°C, instead of the more classical room temperature reflectance measurements.

6.2 EXPERIMENTAL DETAILS

The tandem absorber (TiAlC (62 nm)/TiAlCN (20 nm)/TiAlSiCN (18 nm) /TiAlSiCO (16 nm) /TiAlSiO (27 nm)) was deposited on stainless steel substrates (25 mm diameter) by an unbalanced magnetron sputtering system as discussed in Chapter 2. Stainless steel is usually used in parabolic trough and Fresnel receiver tubes.

Solar absorptance α_S and thermal emittance $\varepsilon(T)$ at temperature T were calculated according to the following expressions, from spectral reflectance measured at room temperature in the 0.25 – 25 μm range or at temperature T in the 1.2 – 25 μm range, and linearly extrapolated in the 25 – 30 μm range. These are directional (depending on angle) total (integrated over wavelength) values.

Solar absorptance
$$\alpha_s = \frac{\int_{0.25\mu m}^{4\mu m}[1-R(\lambda,T_a)].G(\lambda).d\lambda}{\int_{0.25\mu m}^{4\mu m} G(\lambda).d\lambda}$$
(6.8)

As the necessary spectral reflectance data was available in this case, solar absorptance was calculated considering the complete solar range of 0.25 – 4 μm, instead of the usual restricted range of 0.25 – 2.5 μm (for which only one spectrophotometer is needed), giving rise to more accurate values.

Directional thermal emittance

- from room temperature (T_a) reflectance

$$\varepsilon_\theta(\theta, T) = \frac{\int_{0.25\mu m}^{30\mu m}[1-R(\lambda, \boldsymbol{T_a}, \theta)].P(\lambda, T).d\lambda}{\int_{0.25\mu m}^{30\mu m} P(\lambda, T).d\lambda} \qquad (6.9)$$

- from reflectance at temperature T

$$\varepsilon_\theta(\theta, T) = \frac{\int_{0.25\mu m}^{30\mu m}[1-R(\lambda, \boldsymbol{T}, \theta)].P(\lambda, T).d\lambda}{\int_{0.25\mu m}^{30\mu m} P(\lambda, T).d\lambda} \qquad (6.10)$$

where

- $R(\lambda, T)$ is the sample spectral reflectance measured at temperature T;

- $G(\lambda)$ is the solar spectrum (ASTM-G173 AM 1.5 direct + circumsolar);

- $P(\lambda, T)$ is the blackbody emission spectrum at T, given by Planck's law.

The spectral reflectance of the tandem absorber was measured in the UV to mid-IR range (0.25 – 25 µm) by two spectrophotometers: in the 0.25 – 2.5 µm range, a PerkinElmer Lambda 950 equipped with 150 mm Spectralon-coated integrating sphere and small spot kit (measured area reduced to 10 mm in diameter); and in the 1.2-25 µm range, a SOC100-HDR coupled with Nicolet 6700 FTIR and equipped with a heated sample holder up to 500°C. UV-Vis-NIR and IR spectra were joined at 2.4 µm. With the UV-Vis-NIR spectrophotometer, the directional hemispherical reflectance (DHR) was measured (directional incidence angle of 8° and hemispherical reflection from the sample surface). With the SOC100-HDR, the hemispherical directional reflectance (HDR) was measured instead (hemispherical incidence from a semi-ellipsoidal gold-coated mirror reflecting the light from a blackbody at 700°C, and directional reflection from the sample detected by a movable mirror, at a variable angle from 8 to 70°, reflecting towards the FTIR). DHR and HDR are mathematically equivalent. Further description of the experimental procedure and equipment can be found in (Mercatelli et al., 2016).

Coatings were also subjected to thermal annealing in air up to 800°C for 2 h to study the degradation. The heating rate was 5°C/min. The adhesion failure of the tandem absorber was assessed by performing adhesive tape test for samples heat treated at 500 and 600°C for 8 h as per ASTM D903 standards. The adhesion test was also carried after the samples were subjected to thermal shock tests at 300, 350 and 400°C up to 100 cycles.

6.3   RESULTS AND DISCUSSION

6.3.1. Reflectance measurements at room temperature

In order to validate the selective behavior of the tandem absorbers on one hand, and the reproducibility of the deposition technique to provide similar samples when applying the same synthesis parameters on the other hand, reflectance data was acquired at room temperature (RT) from 0.25 to 25 µm for two equivalent as-deposited samples (denoted as Sample 1 and 2 hereafter, Fig. 6.1). Only a very slight difference in the reflectance was observed between the
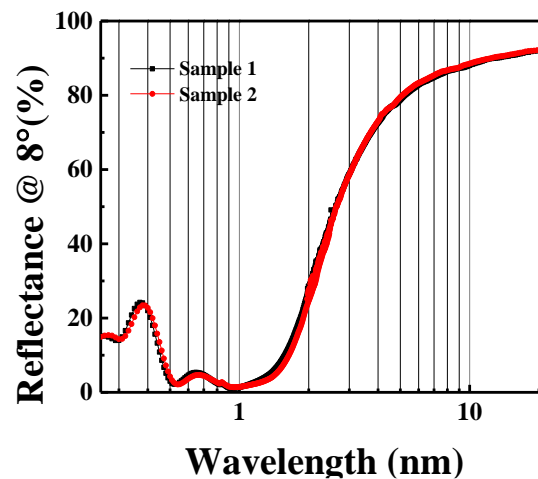
Figure 6.1: Near-normal (directional at θ = 8°) spectral reflectance of the two equivalent samples.

two samples, ensuring the aforementioned reproducibility. The selective behavior was also clearly observed, with low reflectance from 0.5 to 1.5 µm and increasing beyond 1.5 µm. The corresponding solar absorptance and thermal emittance at 400°C and 500°C (from Eq. 6.9) were calculated and are reported in Table 6.1. Their solar absorptance is high, around 0.93, while their thermal emittance is around 0.21 at 400°C and around 0.25 at 500°C, which is an acceptable value for selective coatings able to operate in air. As a comparison,

Archimede receivers with selective coatings able to operate in vacuum only have $\varepsilon\,(400°C)$ < 0.08 and $\varepsilon\,(550°C)$ < 0.11 (Giostri et al., 2012).

	Sample 1	Sample 2
α_S	0.929	0.927
ε_θ ($\theta = 8°$, T = 400°C) from %R measured @ RT	0.214	0.209
ε_θ ($\theta = 8°$, T = 500°C) from %R measured @ RT	0.251	0.244

Table 6.1: Solar absorptance and thermal emittance of two equivalent samples, calculated from reflectance (%R) measurements at room temperature (RT) in the 0.25 – 25 μm range.

6.3.2 IR reflectance measurements in temperature

The IR reflectance of Sample 1 was measured in temperature up to 500°C, which is the maximum PID regulation set-point of the heated sample holder. Reflectance spectra at room temperature (as-dep), 80°C, 100°C, 200°C, 300°C, 400°C and 500°C were recorded (PID
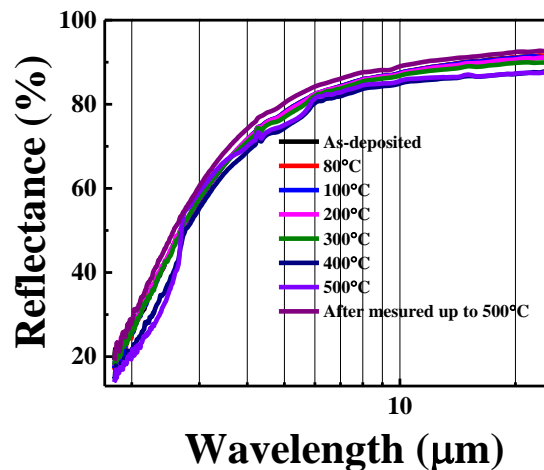
Figure 6.2: Reflectance measurements in temperature for Sample 1 (PID regulation set point temperatures).

regulation set-point temperatures) and are shown in Fig. 6.2. No change in reflectance was observed up to 200°C and only a slight evolution was visible at 300°C. Above 400°C, the IR reflectance decreases. At 500°C the sample holder and the sample visibly glow (Fig. 6.3). The sample reflectance at room temperature was again measured after the heat treatment measurements and was found to have increased (Fig. 6.2), indicating some degree of aging of the sample due to heating, thus, leading to lower thermal emittance (Table 6.2).

	Before	**After (1)**	**After (2)**
α_S	0.929	0.890	0.907
ε_θ ($\theta = 8°$, T = 500°C) from %R measured @ RT	0.251	0.231	

Table 6.2: Optical properties of Sample 1 before and after high temperature measurements (after, reflectance measurements in the 0.25 – 25 μm range were acquired on two different areas of the sample, labeled (1) and (2)).

Figure 6.3: Photograph of the measurement set up. From left to right, blackbody IR source at 700°C with chopper, reference sample (specular gold), heated sample holder with Sample 1 at set-point of 500°C. The movable detecting mirror is also visible in the back.

It may be noted that the temperature read by the thermocouple at the surface of the sample was used for PID regulation. This thermocouple is only in contact with the edge of the sample (to allow for reflectance measurements in the center of it). Only a small area of the thermocouple was therefore in contact with the surface and the temperature of the sample was underestimated, especially at high temperature, therefore, the temperature regulation was not optimal. In consequence, at high temperature the sample real temperature exceeded the set-point temperature (Fig. 6.4). The former was measured independently by an external thermocouple and was found to be 100°C above set-point at high temperature (for instance at set-point 500°C, the surface of the sample was actually at 610°C).
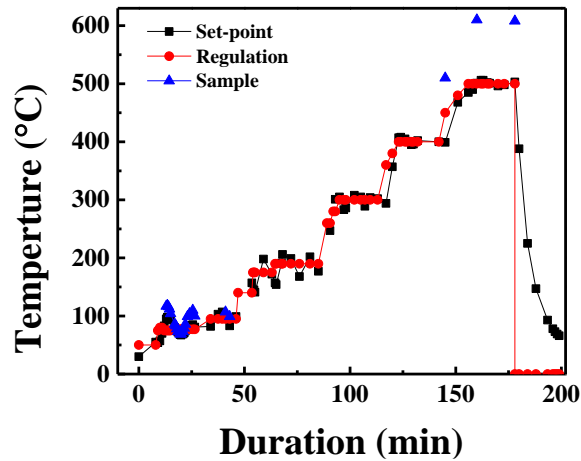
Figure 6.4: Temperature of heated sample holder: PID regulation temperature set-point (rectangles), temperature read by the PID regulation thermocouple at the surface of the sample (circles), and real sample surface temperature read by an external thermocouple (triangles).

This fact explains the aspect and property change of the sample after HT measurements, as seen in Figs. 6.5 and 6.6. A surface non-uniformity clearly appears on the sample surface after HT tests (photo in Fig. 6.5).
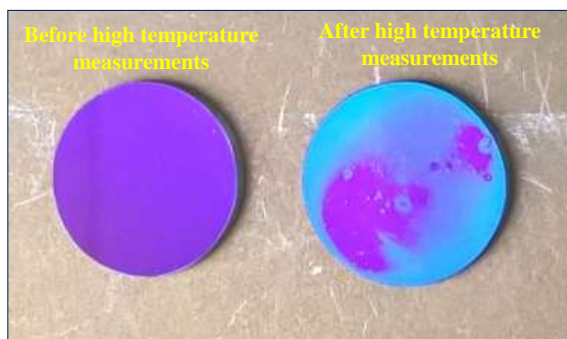
Figure 6.5: As-deposited sample (Sample 2, on the left) and sample after HT measurements up to 500°C (Sample 1, on the right).

This non-uniformity is also visible on the UV-Vis-NIR reflectance spectra of the sample after HT tests, which are different when acquired on two different areas of the sample (Fig. 6.6, "after (1)" and "after (2)", where the sample position was randomly changed between the two measurements). Fig. 6.6 also shows the evolution in reflectance before and after HT measurements up to 500°C, with an increased UV-Vis-NIR reflectance after the tests and its shift towards higher wavelengths. This change could be due to the degradation of the antireflective coating and leads to lower solar absorptance, as seen in Table 2 which depicts α_S and $\varepsilon(500°C)$ (calculated from RT measurements in Fig. 6.6) of Sample 1 before and after HT measurements. Reflectance in the NIR-IR region is also decreased (Fig. 6.6), leading to higher thermal emittance (Table 2), perhaps due to diffusion phenomena between the IR-reflective layer and the SS substrate. In any case, it reveals a certain amount of aging of the sample, however, this aging occurred above the so far established thermal stability temperature (610°C).
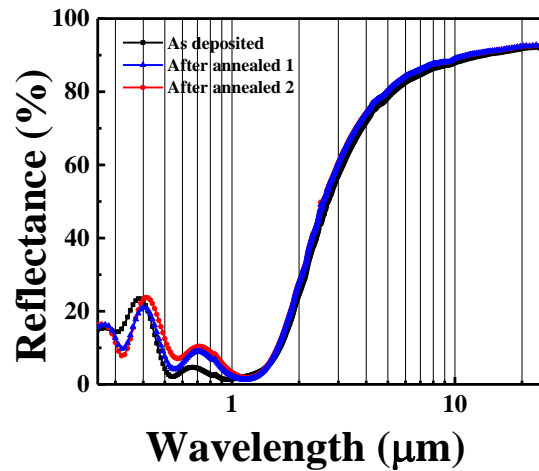
Figure 6.6: Reflectance of Sample 1 before and after HT measurements up to 500°C. Two different areas of the sample (randomly selected) after HT tests were measured in the UV-Vis-NIR region.

Table 6.3 shows the results of thermal emittance at different temperatures T in the 200°C-500°C range (set point temperature). The first two lines of ε_θ values were calculated in two different wavelength ranges from the same room temperature reflectance measurements in the $0.25 - 25$ μm range, according to expression (6.9). The last line was

calculated from reflectance measurements at temperature *T*, according to expression (6.10). Measurements in temperature were carried out in the 1.2 – 25 µm range only (SOC100-HDR with FTIR spectrophotometer). Therefore, two wavelength ranges were considered for the calculation of the first two lines of ε_θ values in Table 6.3: the complete accessible wavelength range, i.e., 0.25 – 30 µm, and the truncated range of 1.2 – 30 µm (both with linear extrapolation from 25 to 30 µm).

Temperature: Set-point		200°C	300°C	400°C	500°C
Measured on sample		_	_	**510°C**	**610°C**
Line 1	ε_θ ($\theta = 8°$, T) from %R @RT in 0.25 – 30 µm range	0.152	0.181	0.214	0.251
Line 2	ε_θ ($\theta = 8°$, T) from %R @RT in 1.2 – 30 µm range	0.152	0.181	0.214	**0.251**
Line 3	ε_θ ($\theta = 8°$, T) from %R @ T in 1.2 – 30 µm range	0.157	0.191	**0.246**	0.275
	Relative error (%) for line 2 compared to line 3	-3.2%	-5.2%	-13.0%	-8.7%
				2.0%	

Table 6.3: Solar absorptance and thermal emittance of Sample 1 calculated from reflectance (%R) measurements in the 0.25 – 25 µm range at room temperature (RT), and in the 1.2 – 25 µm range at temperature *T*. Either the whole measured range (lines 1 and 3) or a truncated range (line 2) was considered for calculation and %R was extrapolated to 30 µm in all cases.

The comparison of lines 1 and 2 shows the validity of considering the truncated wavelength interval only, as ε_θ values in (1.2 – 30 µm) and (0.25 – 30 µm) ranges are equal. Indeed, the blackbody emission below 1.2 µm is very low at these temperatures. When comparing lines 2 and 3, one can also conclude on the validity of the classical "non-dependence of reflectance with temperature" hypothesis to estimate thermal emittance from RT measurements (line 2). Calculation from RT measurements, however, leads to underestimated values. The relative error made with this hypothesis as compared to "real" values measured at temperature *T* (line 3) is reported in Table 3 (relative error = (line 2 – line 3) / line 3). This error reaches rather high values at high temperature (non-negligible values, up to 13%). However, when considering that the set-point temperature is lower than the real temperature of the sample, i.e., at set-point "400°C" the sample is in fact at 510°C,

one should use the values in bold red for the relative error calculation, leading to a slight overestimation of ε_θ with a much lower relative error of 2% instead. This fact is even better illustrated in Fig. 6.7 where the values of thermal emittance in temperature from Table 3 are plotted. The red squares represent the values of $\varepsilon(T)$ calculated at T = 200, 300, 400 and 500°C from room temperature reflectance measurements in the 1.2 – 25 µm range (line 2 of Table 3). The green triangles are thermal emittance values calculated from reflectance measurements in temperature, considering the actual temperature measured on the sample (510 and 610°C) instead of the set-point temperature. The agreement between thermal emittance values estimated from room temperature measurements (red squares) and from measurements in temperature (green triangles) is rather good as both follow a similar
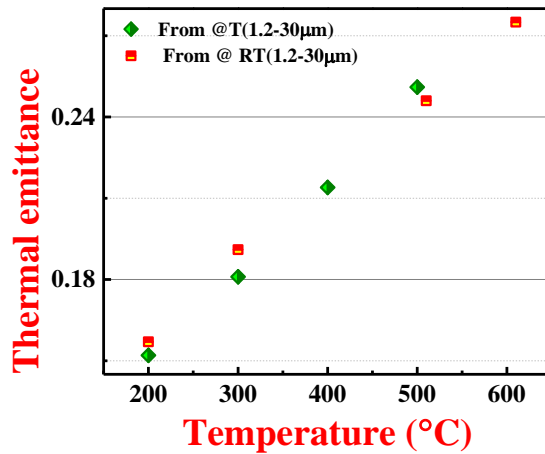
Figure 6.7: Thermal emittance as a function of temperature, calculated from room temperature reflectance measurements (red squares) and from reflectance measurements in temperature, considering the temperature actually measured on the sample instead of the set-point temperature (green triangles).

evolution with temperature. The approximation made in the former case is therefore acceptable for this materials.

In summary, the emissivity of the spectrally selective coating measured from RT measurements is little underestimated to that measured using the high temperature measurements. Out results are in agreement with these reported by Echaniz et al. (Echaniz et al., 2015) and Setien-Fernandez et al. (Setien-Fernandez et al., 2013).

6.3.3 Annealing studies in air

In order to study the change in emittance value after annealing, the tandem absorber deposited on stainless steel substrate was annealed at different temperatures (300°C - 850°C) for 2 h in air environment and also to see the microstructural changes and subsequent failure of the coating at high temperatures. The corresponding reflectance spectra are shown in Fig. 6.8(a). Fig. 6.8(b) shows the solar absorptance and emittance values of the tandem absorber at different temperatures, measured ex-situ using solar reflectometer and emissometer.
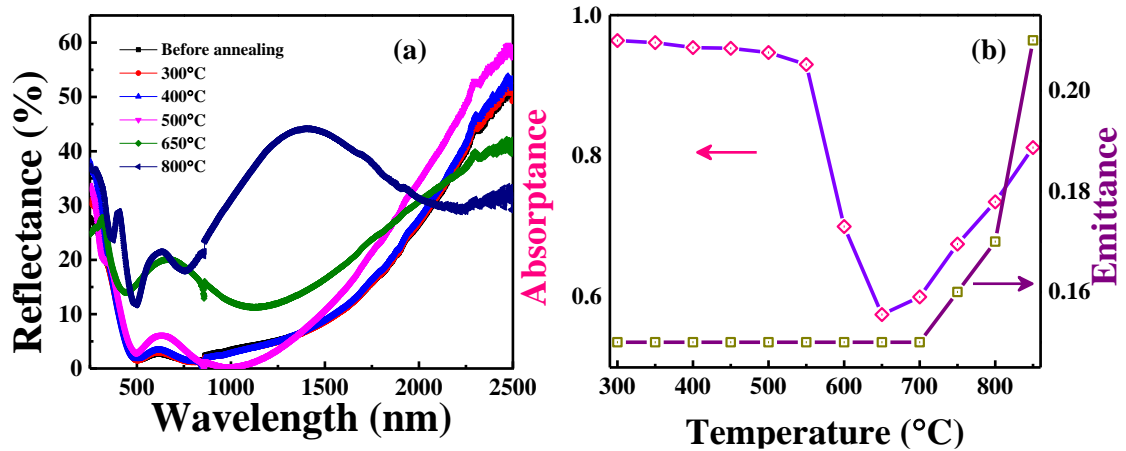
Figure 6.8: (a) Reflectance of tandem absorber annealed in air for 2 h at different temperatures; (b) the measured absorptance and emittance of the annealed tandem absorber in air at different temperatures. The absorptance was measured at R.T., whereas, the emittance was measured at 82°C using Devices and Services instrument.

Emittance of the tandem absorber, measured at 82°C, is constant up to annealing at 700°C. Increase in emittance value was observed from 750°C onwards. The tandem

absorber shows the highest emittance value (0.21) after annealing at 850°C. The temperature versus absorptance graph shows almost constant absorptance up to 500°C. Thereafter, a decrease in absorptance of the tandem absorber with temperature up to 650°C was observed. Further increase in temperature increases the absorptance and emittance values, due to oxidation of the tandem absorber or out-diffusion of metallic interlayer or that of substrate into the absorber coating as explained earlier. The XRD data presented in Fig. 6.9 shows that when the coating is heated at 800°C in air, there is a significant oxide formation either due to outward diffusion of Fe or inward diffusion of oxygen through the coating. This results in increases in both absorptance and emittance values as depicted in Fig. 6.8(b). The increase in absorptance beyond 650°C in Fig. 6.8(b) is attributed to increase in surface roughness (Fig. 6.10(d-f)).
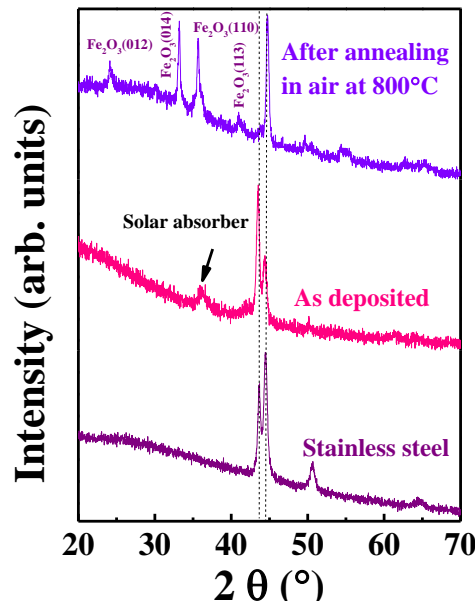
Figure 6.9: XRD data of stainless substrate, as-deposited solar absorber coating and solar absorber coating heated in air at 800°C for 2 h.

As discussed earlier, emittance depends upon the roughness of the substrate. The surface morphology affects the interaction of light differently for macroscopic and microscopic surfaces. In the former the light undergoes reflection and scattering after being

absorbed partially (Raut et al., 2011). However, when the roughness creates fine nanostructure patterns or sub-wavelength structures, the light rays get trapped in by multiple reflections, resulting in high absorption of the incident radiation. The surface roughness of the annealed tandem absorber at different temperatures was studied by AFM as shown in Fig. 6.10. The roughness of the tandem absorber did not show any significant change up to 500°C, whereas, further increase in the annealing temperature
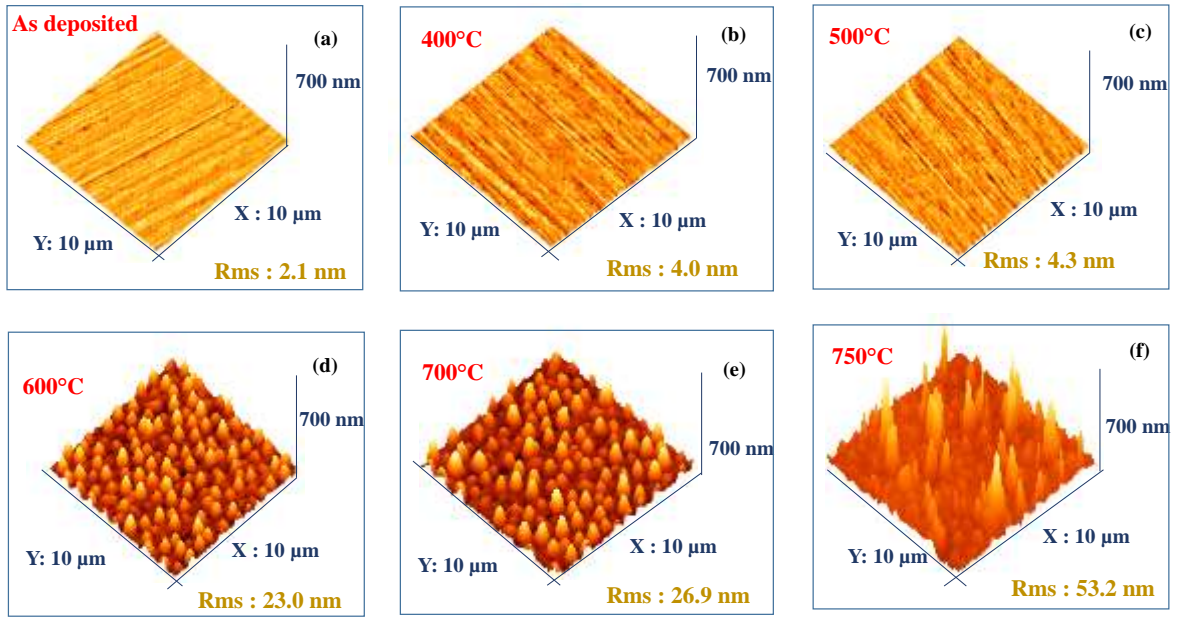
Figure 6.10: 3D- AFM images of the annealed tandem absorber in air: (a) as-deposited, (b) 400°C, (c) 500°C, (d) 600°C, (e) 700°C, and (f) 750°C.

increases the surface roughness of the tandem absorber as shown in Fig. 6.10(d-f). The highest surface roughness of the tandem absorber (σ_{rms} = 53.2 nm) was observed at the temperature of 750°C, which leads to a decrease in selectivity of the tandem absorber. Concurrently, the formation of oxide as discussed in Fig. 6.9 also contributes to a decrease in selectivity of the coating. This data further supports the previous observation, the increase in emittance of the tandem absorber with annealing temperature of 750°C onwards (see Fig. 6.8(b)). Looking at Figs. 6.8 and 6.10, it is clear that the effect of roughness on

the emittance up to 500°C is minimal and hence the emittance data presented in Table 6.3 represents intrinsic behavior of the spectrally selective coating at high temperatures.

6.3.4   Adhesion measurements

The adhesion deals with functionality of the coating at high temperature, which is very important for solar thermal applications.
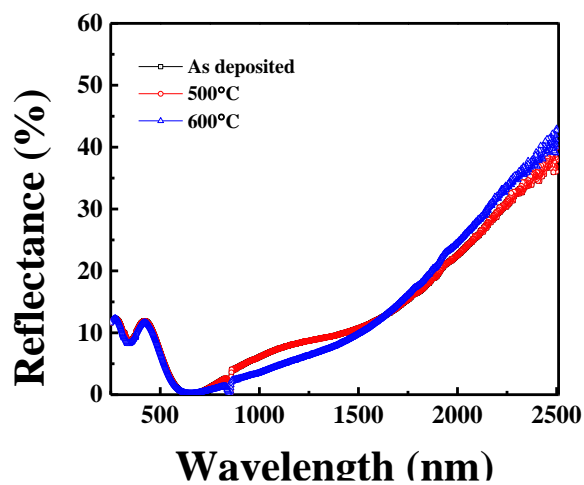
Figure 6.11: Reflectance spectra of the tandem absorber before and after adhesion test. The samples were heated in air for 8 h at 500 and 600°C.

The adhesion failure of the tandem absorber coating was assessed by performing adhesive tape test for samples heat treated at 500 and 600°C for 8 h. After each temperature cycle, adhesion test was performed and measured the reflectance spectra of the tandem absorber as shown in Fig. 6.11. The samples do not show any major changes in reflectance spectra before and after adhesion test, indicating very good adhesion of the coating on substrate as a result of heat-treatment. Further, there no visual peeling off the coating from the substrate was observed. Which shows the adhesion of the coating is good. The slight change in reflectance spectrum for sample heat treated at 600°C is due to the degradation of the coating as a result of heat treatment. Further, solar coating was annealed under thermal shock conditions at 300, 350 and 400^{0}C in air up to 100 cycles each. Fig. 6.12 shows reflectance spectra after thermal shock tests at different temperatures and cycles.
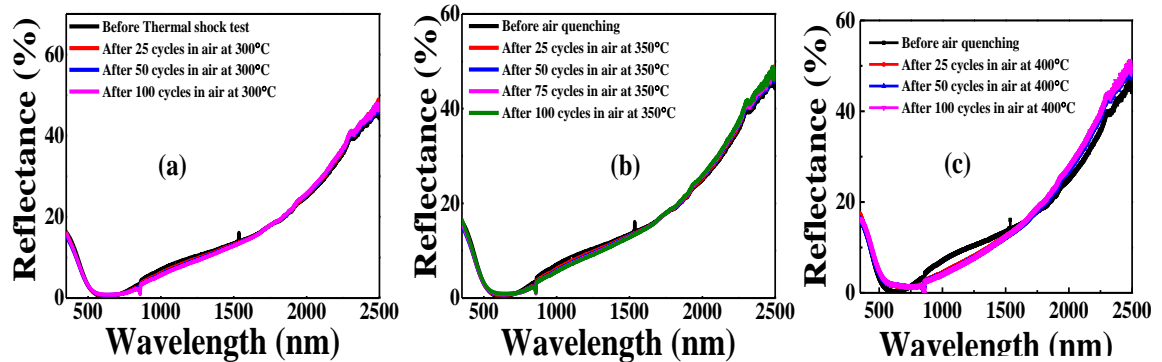
Figure 6.12: Reflectance spectra of solar absorber coating after subjecting to thermal shock tests in air (different cycles) at temperatures of: (a) 300 (b) 350 and (c) 400°C.

The adhesion remained unaffected after the thermal shock tests.

There are no changes in the spectra even after the thermal shock tests. The adhesion of these coatings was also measured as stated above and it remained unaffected even after thermal shock tests, which demonstrates very good adhesion of the coating.

6.3.5 Photothermal conversion efficiency of the tandem absorber

The performance of solar absorber can be predicted by calculating their photothermal conversion efficiency using Equation (1.8) (Cao et al., 2002). Assuming a concentration ratio of 100 and the absorber temperature of 500°C for a typical parabolic trough (vacuum receiver) or linear Fresnel (receiver in static air) power plants and the typical solar flux intensity of 1000 W/m^2, the photothermal conversion efficiency is approximately 88%. Absorptance of 0.928 and emittance of 0.248 at 500°C have been considered for these calculations. It may be noted that thermal losses other than radiative have not been taken into consideration for the above calculation, as convective and conductive losses are negligible compared to radiative losses at high temperature.

6.4 SUMMARY

> The reflectance spectra of the samples were acquired in the 0.25 – 25 μm range at room temperature using two spectrophotometers. Their solar absorptance and thermal emittance at 400°C and 500°C were calculated from these measurements.

> The samples exhibited good selectivity (α_S = 0.927 – 0.929, ε (500°C) = 0.244 – 0.251). High temperature reflectance measurements were carried out in the 1.2 – 25 μm range on one of the samples.

> HT tests caused some degree of aging to the sample, as its visual aspect and reflectance changed after the tests, leading to lower α_S (0.890 – 0.907) and ε (0.231) as measured at RT on the cooled sample.

> As ε decreases (lower IR emission), compensating for the loss of solar absorption, the overall optical efficiency of the coating will however not be dramatically altered, thus leading to a photo-thermal conversion efficiency of 88%.

> Ca0The estimation of thermal emittance based on reflectance measurements at room temperature was found to be rather acceptable when considering thermal emittance at real sample temperature instead of set-point, with low relative error of 2% at 500°C (ε = 0.248).

Chapter 7

CONCLUSIONS AND SCOPE FOR THE FUTURE WORK

This Chapter dedicates the overall summary of the results with justification described in previous Chapters. Moreover, this Chapter includes few propositions for the future work.

7. 1 CONCLUSIONS

The main idea of this work was to study the suitability of carbide and carbo-nitrides materials for high temperature solar thermal applications. The study of the structural, optical properties and thermal stability proves the usefulness of designed tandem absorber beneficial for high temperature solar thermal applications. Overall, these studies offer a better understanding and suitability of these materials for high temperature solar thermal applications. The salient features of this work is summarized below:

- Spectrally selective coatings of TiAlC/TiAlCN/TiAlSiCN/TiAlSiCO/TiAlSiO were deposited on stainless steel and silicon substrates using unbalanced magnetron sputtering system. The designed tandem absorber shows high absorptance of 0.961 with an emittance of 0.15 at 82°C. Further, emittance of the tandem absorber was decreased to 0.07 by incorporating the tungsten layer.

- The design of the coating has been achieved by controlling the electrical resistivity and the thicknesses of the individual layers. The measured resistivity and reflectance data confirm the decrease of metallic nature from bottom to the top layer of the tandem absorber. The individual layer thicknesses of TiAlC, TiAlCN, TiAlSiCN, TiAlSiCO and TiAlSiO were 62, 18, 20, 16, 27 nm, respectively.

- The influence of reactive gas flow rates (C_2H_2, N_2, O_2) and thicknesses of each individual layers of the tandem absorber on selective properties was also studied in detail using XPS, UV-NIR-IR spectrophotometer and nanoprofilometer.

- Thick layers of TiAlC, TiAlCN, TiAlSiCN, TiAlSiCO and TiAlSiO were deposited on stainless steel substrates, and their refractive indices and extinction coefficients were studied by spectroscopic ellipsometry technique. Cauchy's absorbent model was used to fit TiAlC, TiAlCN, and TiAlSiCN layers, whereas Tauc-Lorentz model was employed for TiAlSiCO and TiAlSiO layers.

- At 500 nm, the refractive indices of TiAlC, TiAlCN, TiAlSiCN, TiAlSiCO, and TiAlSiO layers were 2.51, 2.15, 1.54, 1.48, and 1.44, respectively. The TiAlC layer shows the highest extinction coefficient value, indicating that the TiAlC plays a major role as an absorbing layer. The extinction coefficient values follows the decreasing order from TiAlC (bottom) to TiAlSiO (top) layers. The k values of TiAlSiCO and TiAlSiO were almost zero, confirming that these layers are intermediate and antireflective in nature.

- SCOUT software was utilized to simulate the experimental reflectance spectra by means of the appropriate thickness, refractive index, and extinction coefficient of each layer of the tandem absorber. The simulated spectra were in good accordance with the experimental spectra.

- The average reflectance spectra of the tandem absorber show a low reflectance in the solar spectral region over a wide range of angles from 8° to 58°. No significant change in the emittance of the tandem absorber was observed for angles below 50° in the infrared region either. The tandem absorber therefore keeps its selective properties at a wide range of incidence angles.

- High temperature reflectance measurements were carried out in the 1.2–25 μm range. At the temperature of 200°C, 300°C, 400°C and 500°C the tandem absorber shows the emittance of 0.152–0.157, 0.181–0.19, 0.214–0.246 and 0.251–0.275, respectively.

- The estimation of thermal emittance based on reflectance measurements at room temperature was found to be rather acceptable when considering thermal emittance at real sample temperature instead of set-point, with low relative error of 2% at 500 °C (ε=0.248).

- The performance evaluation of the tandem absorber was studied by heating it in air and vacuum at different temperatures. The tandem absorber shows the long thermal stability up to 325°C for 600 h in air environment and in vacuum up to 600°C for 910 h under cyclic heating conditions.

7. 2 Scope and predictions

❖ The idea of the present research work is to understand and extend the knowledge on suitability of carbide and carbo-nitride materials for high temperature solar thermal applications.

❖ More detailed analysis is required to study the failure mechanism of the designed tandem absorber at high operating temperature in air and vacuum. The change in structural, micro structural and inter-diffusion properties of individual layers of the tandem absorber with respect to the annealed temperatures has to be studied. Various techniques such as depth profile in XPS, SIMS, EPMA, DSC and high temperature XRD can be utilized to study the failure mechanism of the coating.

❖ The selective properties of the designed tandem absorber can be improved by using the alloy targets. In order to reduce the manufacture cost of designed tandem absorber, few more experimental analysis yet to be done for the simple and less processing steps. So, as to reduce the number of individual layers.

❖ Studies have to be carried out further for suitability and performance of the designed tandem absorber for high temperature solar tower applications.

❖ To improve the quality of the product and to increase the potential of the selective surfaces for high temperature applications. The better possible way is by using the HfC and TaC materials as spectrally selective surfaces, which have high melting points.

❖ Furthermore, another possible material for future work is by using the combination of transition metals with borides, which are the promising materials for future applications.

REFERENCES

Agnihotri, O.P. and Gupta, B.K. (1981). ''*Solar Selective Surfaces.*'' John Wiley & Sons, New York.

Alejandro, A. and Ulises. M. (2006). "Thermally and air-plasma-oxidized titanium and stainless steel plates as solar selective absorbers." *Sol. Energy Mater. Sol. Cells,* 90, 2556–2568.

Alfonsetti. R., Simone, D.G., Lozzi, L., Passacantando, M., Picozzi, P. and Santucci, S. (1994). "SiO, Surface stoichiometry by XPS: a comparison of various methods." *Surf. Interface Anal*., 22, 89 – 92.

Andersson, A., Hunderi, O. and Granqvist, C.G. (1980). "Nickel pigmented anodic aluminium oxide for selective absorption of solar energy." *J. Appl. Phys.,* 51, 754–764.

Andreas, S. Ivan, R.V., Peter, O. and Stefan, B. (2001). "Titanium-containing amorphous hydrogenated silicon carbon films (a-Si:C:H/Ti) for durable solar absorber coatings." *Sol. Energy Mater. Sol. Cells*, 69, 271 – 284.

Antonaia, A., Castaldo, A., Addonizio, M. L. and Esposito, S. (2010). "Stability of W-Al_2O_3 cermet based solar coating for receiver tube operating at high temperature." *Sol. Energy Mater. Sol. Cells,* 94, 1604–11.

Antonucci, P.L., Alderucci, V., Giordano, N., Cocke, D.L. and Kim, H. (1994). "The role of surface functional groups in Pt carbon interaction." *J. Appl. Electrochem*., 24, 58 – 65.

Atasi, D., Kamanio, C., Barshilia, H.C. and Bikramjit, B. (2016). "Colored selective absorber coating with excellent durability." *Thin Solid Films,* 620, 17 – 22.

Atasi, D., Barshilia, H.C., Chattopadhyay, K. and Bikramjit, B. (2017). "Solar energy absorption mediated by surface plasma polaritons in spectrally selective dielectric-metal-dielectric coatings: A critical review." *Renew. Sust. Energ. Rev.,* 79, 1050–1077.

Atkinson, C., Sansom, C.L., Almond, H.J. and Shaw, C.P. (2015). "Coatings for concentrating solar systems – A review." *Renew. Sust. Energ. Rev.,* 45, 113–122.

Azadi, M., Rouhaghdam, A.S. and Ahangarani, S. (2013). "Properties of TiC coating by pulsed DC PACVD." *J. Coat.,* 2013, 1–6.

Azzam, R.M.A. and Bashara, N.M. (1977). *Ellipsometry and Polarized Light*, 3rd edn., Elsevier, North-Holland, Amsterdam.

Barshilia, H.C. (2014). "Growth, characterization and performance evaluation of Ti/AlTiN/AlTiON/AlTiO high temperature spectrally selective coatings for solar thermal power applications." *Sol. Energy. Mater. Sol. Cells,* 130, 322–330.

Barshilia, H.C., Deepthi, B. and Rajam, K.S. (2006). "Reactive sputtering of hard nitride coatings using asymmetric-bipolar pulsed DC generator." *Surf. Coat. Technol.,* 201, 1827 – 1835.

Barshilia, H.C., Kumar, P., Rajam, K.S. and Biswas, A. (2011). "Structure and optical properties of Ag–Al$_2$O$_3$ nanocermet solar selective coatings prepared using unbalanced magnetron sputtering." *Sol Energy Mater. Sol. Cells,* 95, 1707–15.

Barshilia, H.C., Selvakumar, N. and Rajam, K.S. (2006). "TiAlN/TiAlON/Si$_3$N$_4$ tandem absorber for high temperature solar selective applications." *Appl. Phys. Lett*., 89, 191909-1 – 3.

Barshilia, H.C., Selvakumar, N. and Rajam, K.S. (2007). "Thermal stability of TiAlN/TiAlON/Si$_3$N$_4$ tandem absorbers prepared by reactive direct current magnetron sputtering." *J. Vac. Sci. Technol.*, 25(2), 383–390.

Barshilia, H.C., Selvakumar, N. and Rajam, K.S. (2008). "Structure and optical properties of pulsed sputter deposited Cr$_x$O$_y$/Cr/Cr$_2$O$_3$ solar selective coatings." *J. Appl. Phys.,* 103, 023507-11.

Barshilia, H.C., Selvakumar, N., Rajam K.S., Sridhara, D.V. and Muraleedharan, K. (2008). "Deposition and characterization of TiAlN/TiAlON/Si$_3$N$_4$ tandem absorber prepared using direct current magnetron sputtering." *Thin Solid Films*, 516, 6071 – 6078.

Barshilia, H.C., Selvakumar, N., Rajam, K.S. and Biswas, A. (2008). "Optical properties and thermal stability of TiAlN/AlON tandem absorber prepared by reactive DC/RF magnetron sputtering." *Sol. Energy. Mater. Sol. Cells,* 92(11), 1425–1433.

Barshilia, H.C., Selvakumar, N., Rajam, K.S. and Biswas, A. (2008). "Spectrally selective NbAlN/NbAlON/Si$_3$N$_4$ tandem absorber for high-temperature solar applications." *Sol. Energy. Mater. Sol. Cells,* 92(4), 495 – 504.

Barshilia, H.C., Selvakumar, N., Rajam, K.S. and Biswas, A. (2008). "Structure and optical properties of pulsed sputter deposited Cr$_x$Oy/Cr/Cr$_2$O$_3$ solar selective coatings." *J. Appl. Phys.,* 103, 0203507-1-0203507–11.

Barshilia, H.C., Selvakumar, N., Rajam, K.S., Sridhara, D.V., Muraleedharan, K. and Biswas, A. (2006). "TiAlN/TiAlON/Si$_3$N$_4$ tandem absorber for high temperature solar selective applications." *App. Phys. Lett.*, 89(19), 1– 4.

Barshilia, H.C., Selvakumar, N., Vignesh, G., Rajam and K.S., Biswas, A. (2009). "Optical properties and thermal stability of pulsed-sputter-deposited Al$_x$O$_y$/Al/Al$_x$O$_y$ multilayer absorber coatings." *Sol. Energy Mater. Sol. Cells*, 93, 315 – 323.

 Bartelmeß, L., Monte, C., Adibekyan, A., Sohr, O., Ottermann, C., Korb, T. and Hollandt, J. (2014). "Characterization of high temperature solar thermal selective absorber coatings at operation temperature." *Energy Procedia*, 49, 2070 – 2079.

Basu, S., Obando, N., Gowdy, A., Karaman, I. and Radovic, M. (2012). "Long-term oxidation of Ti$_2$AlC in air and water vapor at 1000–1300 °C temperature range." *J. Electro Chem. Soc.,* 159, C90–C96.

Bell, F.G. and Ley, L. (1988). "Photoemission study of SiO alloys." *Phys. Rev. B,* 37, 8383 – 8393.

Beng, J.T., Kenneth, J.K. and Peter, M.A.S. (1991). "XPS studies of solvated metal atom dispersed catalysts: Evidence for layered cobalt-manganese particles on alumina and silica." *J. Am. Chem. Soc.*, 113, 855 – 861.

Berg, S., Larsson, T. and Biom, H.O. (1985). "The use of nitrogen flow as a deposition rate control in reactive sputtering." *J. Vac. Sci. Technol. A*, 4, 594 – 600.

Berreman, D.W. (1963). "Infrared absorption at longitudinal optic frequency in cubic crystal films." *Phys. Rev.*, 130, 2193–2198.

Bhattacharya, D., Biswas, A. and Sahoo, N.K. (2004). "Investigation on dispersion of optical constants of Gd_2O_3 films by phase modulated spectroscopic ellipsometry." *Appl. Surf. Sci.* 233, 155–162.

Bhattacharyya, D., Sahoo, N.K., Thakur, S. and Das, N.C. (2001). "Characterization of a multilayer highly reflecting mirror by spectroscopic phase-modulated ellipsometry." *Appl. Opt.* 40, 1707–1714.

Bhattacharyya, D., Sahoo, N.K., Thakur, S. and Das, N.C. (2002). "Phase modulated spectroscopic ellipsometry of dielectric multilayer beam combiner." *Thin Solid Films,* 416, 97-105.

Biswas, A., Bhattacharyya, D., Barshilia, H.C., Selvakumar, N. and Rajam, K.S. (2008). "Spectroscopic ellipsometric characterization of $TiAlN/TiAlON/Si_3N_4$ tandem absorber for solar selective applications." *Appl. Surf. Sci.*, 254(6), 1694 – 1699.

Brandt, R., Bird, C. and Neuer, G. (2008). "Emissivity reference paints for high temperature applications." *Measurement,* 41, 731–736.

Brewer, L. (1967). "A most striking confirmation of the Engel metallic correlation," *Acta Met.,* 15, 553–556.

Brodu, E., Balat-Pichelin, M., Sans, J.L., Freeman, M.D. and Kasper, J.C. (2015). "Efficiency and behavior of textured high emissivity metallic coatings at high temperature." *Mater. Des.,* 83, 85-94.

Campo, L.D., Perez - Saez, R.B. and Tello, M.J. (2008). "Iron oxidation kinetics study by using infrared spectral emissivity measurements below 570°C". *Corro. Sci.,* 50, 194 – 9.

Cao, A., Zhang, X., Xu, C., Wei, B. and   Wu, D. (2002). "Tandem structure of aligned carbon nanotubes on Au and its solar thermal absorption." *Sol. Energy Mat. Sol. Cells*, 70, 481-486.

Cao, F., McEnaney, K., Chen, G. and Ren, Z. (2014). "A review of cermet-based spectrally selective solar absorbers." *Energy Environ. Sci.,* 7, 1615–27.

Cao, F., Daniel, K., Sun, T., Lan, Y., Chen, G. and Ren, Z. (2015). "Enhanced thermal stability of W–Ni–Al$_2$O$_3$ cermet-based spectrally selective solar absorbers with tungsten infrared reflectors." *Adv. Energy. Mater.,* 5, 1401042-1–1401042-7.

Cao, G., Weber, S.J., Martin, S.O., Anderson, M.H., Sridharan, K. and Allen, T.R. (2012). "Spectral emissivity measurements of candidate materials for very high temperature reactors." *Nucl. Eng. Des.,* 251, 78–83.

Cao, S., Wang, J. and Hao, W. (2016). " Formation mechanism of large SiC grains on SiC fiber surfaces during the heat treatment." *Cryst. Eng. Comm*., 18, 3674 -3682.

Cartalis, C., Synodinou, A., Proedrou, M., Tsangrassoulis, A. and Santamouris, M. (2001). "Modifications in energy demand in urban areas as a result of climate changes: an assessment for the southeast Mediterranean region." *Energy Convers. Manage.,* 42, 1647–1656.

Chang, S.L., Andreregg, J.W. and Theil, P.A. (1996). "Surface oxidation of an Al-Pd-Mn quasi-crystal characterized by X-ray photoelectron spectroscopy." *J. Non-Cryst. Solids,* 195, 95 – 101.

Chester, D., Bermel, P., Joannopoulous, J. D., Soljacic, M. and Celanovic, I. (2011). "Design and global optimization of high-efficiency solar thermal systems with tungsten cermets." *Opt. Exp., 19,* A245–257.

Cindrella, L. (2007). "The real utility ranges of the solar selective coatings." *Sol. Energy Mater. Sol. Cells*, 91, 1898–1901.

 Craighead, H.G., Howard, R.E., Sweeney, J.E. and Buhrman, R.A. (1981). "Graded-index Pt-Al$_2$O$_3$ composite solar absorbers." *Appl. Phys. Lett.,* 39, 29–31.

Cullity, B.D. (1956). "*Elements of X-ray Diffraction.*" Addison-Wesley, Reading, Massachusetts.

Cuomo, J.J., Ziegler, J.F. and Woodall. J.M. (1975). "A new concept for solar energy thermal conversion." *Appl. Phys. Lett.*, 26, 557–559.

Dan, A., Chattopadhyay, K., Barshilia, H.C. and Basu, B. (2016). "Angular solar absorptance and thermal stability of W/WAlN/WAlON/Al$_2$O$_3$-based solar selective absorber coating." *Appl. Therm. Eng.* 109, 997–1002.

Daniel, K., Kenneth M.E., Feng, C., Zhifeng, R. and Gang, C. (2015). "Accurate determination of the total hemispherical emittance and solar absorptance of opaque surfaces at elevated temperatures." *Sol. Energy Mater. Sol. Cells,* 132, 640–649.

DeWitt, D.P. and Nutter, G.D. (1988). "*Theory and Practice of Radiation Thermometry.*" John Wiley and Sons, Inc.*,* Hoboken, New Jersey.

Dincer, I. (2000). "Renewable energy and sustainable development: a crucial review." *Renew. Sustainable Energy Rev.,* 4,157–175.

Dorninique, C., Leon, G., Michel, G., Yolande, B. and Barbara, G. (1994). "Effect of potassium on the surface potential of titania." *J. Chem. Soc. Faraday Trans*., 90, 895 – 898.

Du, M., Hao, L. Jing, M., Fang, L., Liu, X., Jiang, L. and Shumao, W. (2011). "Optimization design of Ti$_{0.5}$Al$_{0.5}$N/Ti$_{0.25}$Al$_{0.75}$N/AlN coating used for solar selective applications." *Sol. Energy. Mater. Sol. Cells*, 95, 1193 – 1196.

Du, P., Wang, X., Lin, I.K. and Zhang, X. (2012). "Effects of composition and thermal annealing on the mechanical properties of silicon oxycarbide films." *Sens. Actuators A*, (176), 90-98.

Dubrovinsky, L.S., Dubrovinskaia, N.A., Swamy, V., Muscat, J., Harrison, N.M., Ahuja, R., Holm, B. and Johansson, B. (2001). "Materials science: The hardest known oxide". *Nature*, 410 (6829), 653–654.

Duffie, J. and Beckman, W. (2006). "*Solar Engineering of Thermal Processes.*" John Wiely & Sons, Inc., Hoboken, New Jersey.

Echaniz, T., Setien-Fernandez, I., Perez-Saez, R.B., Prieto, C., Galindo, R.E. and Tello, M.J. (2015). "Importance of the spectral emissivity measurements at working temperature to determine the efficiency of a solar selective coating." *Sol. Energy Mater. Sol. Cells,* 140, 249–252.

Edlmayr, V., Moser, M., Walter, C. and Mitterer, C. (2010). "Thermal stability of sputtered Al_2O_3 coatings." *Surf. Coat. Technol.* 204, 1576–1581.

Effertz, T. Pernpeintner, J. and Schiricke, B. (2016). "Steady state calorimetric measurement of total hemispherical emittance of cylindrical absorber samples at operating temperature." 22nd *SolarPACES Conf.*, Abu Dhabi, UAE.

Ehrenreich, H. and Seraphin, B.O. (1975). "Symposium on the Fundamental Optical Properties of Solids Relevant to Solar Energy Conversion." *NASA STI/Recon Technical Report N*; 77, 12538.

EI-Awadi, G.A., Abdel-Samad, S. and Waheed, A.F. (2013). "Characterization and properties of TiAlC layer on hard metal substrate WC/Co deposited by physical vapor deposition." *Arab J. Nucl. Sci. Appl.*, 46 (4), 195–202.

Esposito, S., Antonaia, A., Addonizio, M.L. and Aprea, S. (2009). "Fabrication and optimization of highly efficient cermet-based spectrally selective coatings for high operating temperature." *Thin Solid Films,* 517, 6000–6006.

Fan, J.C.C., and Spura, S.A. (1977). "Selective black absorbers using RF-sputtered Cr_2O_3/Cr cermet films." *Appl. Phys. Lett*, 30, 511–3.

Fang, Z., Lu, C., Guo, C., Lu, Y., Gao, D., Ni, Y., Kou, J., Xu, Z. and Li, P. (2015). "Suitability of layered Ti_3SiC_2 and $Zr_3[Al(Si)]_4C_6$ ceramics as high temperature solar absober for solar energy applications." *Sol. Energy. Mater. Sol. Cells,* 134, 252 – 260.

Feng, J., Shuo, Z., Yu, L., Hongwen, Y., Limin, K., Xianyang, W., Zongming, L., Haicheng, D., Yun, T. and Ouyang, J. (2015). "The spectral selective absorbing characteristics and thermal stability of SS/TiAlN/TiAlSiN/Si_3N_4 tandem absorber prepared by magnetron sputtering." *Sol. Energy,* 111, 350 – 356.

Feng, J., Zhang, S., Liu, X., Yu, H., Ding, H., Tian, Y. and Ouyang, J. (2015). "Solar selective absorbing coatings TiN/TiSiN/SiN prepared on stainless steel substrates." *Vacuum,* 121, 135–141.

Feng, J., Zhang, S., Lu, Y., Yu, H., Kang, L., Wang, X., Liu, Z., Ding, H., Tian, Y. and Ouyang, J. (2015). "The spectral selective absorbing characteristics and thermal stability of SS/TiAlN/TiAlSiN/Si_3N_4 tandem absorber prepared by magnetron sputtering." *Sol. Energy*, 111, 350 – 356.

Gao, Y., Yoshitake, M., Zifei, P., Testu, Y. and Kunihito, K. (2003). "Room temperature deposition of a TiO_2 thin film from aqueous peroxotitanate solution." *J. Mater. Chem*., 13, 608 – 613.

Gesing, T. M.; Jeitschko, W. (1995). "The crystal structure and chemical properties of U2Al3C4 and structure refinement of Al_4C_3". *Z. Naturforsch*., *B: Chem. Sci*., 50, 196–200.

Giostri, A., Marco, B., Astolfi, M., Silva, P., Ennio, M. and Giampaolo M. (2012). "Comparsion of different solar plants based on parabolic trough technology." *Sol. Energy*, 86, 1208-1221.

Giraud, P., Braillon, J., Delord, C. and Raccurt, O. (2016). "Development of optical tools for the characterization of selective solar absorber at elevated temperature." *AIP Conference Proceedings,* 1734 130008:1-9.

Goldner, R.B. and Haskal, H.M. (1976). "Indium tin-oxide coated silicon as a selective absorber." *Appl. Opt.,* 15, 1122, 2328–2329.

Goldstein, J.J., Newbury, D.E., Echlin, P., Joy, D.C., Lyma, C.E., Lifshin. E., Sawyer, L. and Michael, J.R. (2003). "*Scanning Electron Microscopy and X-Ray Microanalysis.*" Kluwer Academic/Plenum Publishers, New York.

Gong, D., Liu, H., Luo, G., Zhang, P., Cheng, X., Yang, B., Wang, Y., Min, J., Wang, W., Chen, S., Cui, Z., Kewei, L. and Lifang, H. (2015). "Thermal aging test of AlCrNO-based solar selective absorbing coatings prepared by cathodic arc plating." *Sol. Energy. Mater. Sol. Cells,* 136, 167 –171.

González, F., Barrera-Calva, E., Huerta, L. and Mane, R.S. (2011). "Coatings of Fe_3O_4 nanoparticles as selective solar absorber." *Open Surf. Sci. J*, 3, 131–5.

Granqvist, C.G., Wittwer, V. (1998). "Materials for solar energy conversion: an overview." *Sol. Energy Mater. Sol. Cells*, 54, 39–48.

Gulbinski, W., Mathur, S., Shen, H., Suszko, T., Gilewicz, A. and Warcholinski, B. (2005). "Evaluation of phase, composition, microstructure and properties in TiC/a-C: H thin films deposited by magnetron sputtering." *Appl. Surf. Sci*., 239, 302 – 310.

Hanssen, L.M., Cagran, C. P., Prokhorov, A.V., Mekhontsev, S.N. and Khromchenko, V.B. (2007). "Use of a high temperature integrating sphere reflectometer for surface temperature measurements." *Int. J. Thermo. Phys.,* 28, 566–580.

Harding, G.L. and Lake, M. R. (1981). "Sputter etched metal solar selective absorbing surfaces for high temperature thermal collectors." *Sol. Energy Mater*., 5, 445–464.

Harsh, A.C., Gaurav, G., Praveen K., Srinivas, G., Sijju, Barshilia, H.C. (2015). "Structural and mechanical properties of reactively sputtered TiAlC nanostructured hard coatings." *Surf. Coat. Technol.*, 276, 431–439.

Haynes, William M., ed. (2011). "*CRC Handbook of Chemistry and Physics."* 92nd ed., Boca Raton, FL: CRC Press. p. 4.88.

He, X., Li, Y., Wang, L., Sun, Y. and Zhang, S. (2009) "High emissivity coatings for high temperature application: Progress and prospect." *Thin Solid Films,* 517, 5120–5129.

Heavens, O, S. (1965). *Optical Properties of Thin Solid Films*, 88th edn., Dovers Publications, New York.

Heide, P.V. (2012). "*X-ray Photo-electron Spectroscopy.*" John Wiley & Sons, Inc., New Jersey.

Heidelberg, Shtansky, D.V., Kuptsov, K.A., Kirvukhanstev-Korneev, Ph.V., Sheveiko, A.N. (2011). "Comparative investigation of Al- and Cr- doped TiSiCN coatings." *Surf. Coat. Technol.*, 205, 4640–4648.

Heras, L., Krause, M., Abrasonis, G., Pardo, A., Endrino, J. L., Guillen, E. and Escobar-Galindo, R. (2016). "Advanced characterization and optical simulation for the design of solar selective coatings based on carbon: transition metal carbide nanocomposites." *Sol. Energy Mater. Sol. Cells,* 157, 580 – 590.

Ho, C.K., Mahoney, A.R., Ambrosini, A., Bencomo, M., Hall, A. and Lambert, T.N. (2012). "Characterization of Pyromark 2500 for high-temperature solar receivers." *Am. Soc. Mech. Eng.*, 10, 509–518.

Ienei, E., Isac, L. and Duta, A. "Synthesis of alumina thin films by spray pyrolysis." (2010). *Rev. Roum. Chim.,* 55, 161–165.

Incropera, F.P. and DeWit, D.P. (2002). "*Fundamentals of Heat and Mass Transfer." 5th ed.,* John Wiley and Sons, Inc., New Jersey.

Iqbal, M. (1983). "*An Introduction to Solar Radiation*." Academic press, Cannada.

Jackson, J.D. (1999). "*Classical Electrodynamics*." Wiley, John Wiley & Sons, New York.

Jang, C.S., Jun-Ha, J., Song, P.K. Kang, M.C. and Kim, K.H. (2005). "Synthesis and mechanical properties of $TiAlC_xN_{1-x}$ coatings deposited by arc ion plating." *Surf. Coat. Technol.* 200, 1501–1506.

Jaworske, D.A. (1997). "Thermal modeling of a calorimetric technique for measuring the emittance of surfaces and coatings." *Thin Solid Films,* 236, 146–152.

JCDPS: Joint Committee on Powder Diffraction Standards, file nos.17-0438, 88-2156, 42-1488,74-0310, 76-2484,71-2206,89-4920 and 88–1172.

Jellison, G.E.Jr. and Modine, F.A. (1996). "Parameterization of the optical functions of amorphous materials in the inter band region." *Appl. Phys. Lett.,* 69,

371–372.

Jellison, G.E.Jr., Modine, F.A. (1996)."Erratum: Parameterization of the optical functions of amorphous materials in the interband region.'' *Appl. Phys. Lett.,* 69, 2137–2137.

Jiang, J.Z., Kragh, F., Frost, D.J., Stayhi, K. and Lindelov, K. (2001). "Hardness and thermal stability of cubic silicon nitride." *J. Phys. Condens. Matter*., 13, L515–L520.

Kaltchev, M. and Tysoe, W.T. (1999). "An infrared spectroscopic investigation of thin alumina films: measurement of acid sites and surface reactivity." *Surf. Sci.* 430, 29–36.

Kathy, L., Donald, E. and Mengying, L. (2016). "Thermal stability and electrical conductivity of carbon-enriched silicon oxycarbide." *J. Mater. Chem. C.,* 4, 1829–1837.

Kennedy, C. E. (2002.). "Review of mid-to high-temperature solar selective absorber materials." *Golden, Colo, USA,* National Renewable Energy Laboratory, 1–58.

Kosolapova, T.Y. (1971). "*Carbides*: *Properties, Production and Application."* Plenum Press, New York.

Krishna, V., Murali K.D. and Joshi, S.V. (2014). "Functional multilayer nitride coatings for high temperature solar selective applications." *Sol. Energy Mater. Sol. Cells*, 121, 14 – 21.

Krishnan, R., David, C., Ajikumar, P.K., Nithya, R., Tripura, S.S., Dash, S., Panigrahi, B.K., Kamruddin, M., Tyagi, A.K., Vikram, J. and Baldev, R. (2013). "Reactive pulsed laser deposition of titanium nitride thin films: Effect of reactive gas pressure on the structure, composition, and properties." *J. Mater.,* 2013, 1–5.

Kuhn TS. (1978). "*Blackbody Theory and the Quantum Discontinuity.*" University of Chicago Press, London.

Kumar, S.N., Malhotra, L.K. and Chopra, K.L. (1983). "Nickel pigmented anodized aluminium as solar selective absorbers." *Sol. Energy Mater.,* 7, 439–52.

Kuptsov, K.A. Kiryukhantsev-Korneev, Ph.V., Sheveyko, A.N. and Shtansky D.V. (2013). "Comparative study of electrochemical and impact wear behavior of TiCN, TiSiCN, TiCrSiCN, and TiAlSiCN coatings." *Surf. Coat. Technol.*, 216, 273–281.

Lee, A.W., James, L., Bikram, B., David, M.B., Evelyn N.W. and Gang, C. (2015). "Concentrating solar power." *Chem. Rev*, 115, 12797–12838.

Leng, Y.X., Chen, J.Y., Yang, P., Sun, H. and Huang, N. "Structure and properties of passivating titanium oxide films fabricated by DC plasma oxidation." *Surf. Coat. Technol.*, 166 (2003) 176–182.

Levien L.; Prewitt C. T. (1981). "High-pressure crystal structure and compressibility of coesite." *Am. Mineral.*, 66, 324–333.

Liu, H.D., Wan, Q., Xu, Y.R., Luo, C., Chen, Y.M., Fu, D.J., Ren, F., Luo, G., Cheng, X.D., Hu, X.J. and Yang, B. (2015). "Long-term thermal stability of CrAlO-based solar selective absorbing coating in elevated temperature air." *Sol. Energy. Mater. Sol. Cells,* 134, 261– 267.

Liu, Y., Wang, Z., Lei, D. and Wang, C. (2014). "A new solar spectral selective absorbing

coating of SS–(Fe$_3$O$_4$)/Mo/TiZrN/TiZrON/SiON for high temperature application." *Sol. Energy. Mater. Sol. Cells,* 127, 143 – 146.

Macleod, H.A. (2010). *Thin Film Optical Filters*, 4th edn., CRC press, London, New York.

Maksym, R. and Bell, J.M. (2007). "The effect of sp^2 fraction and bonding disorder on micro-mechanical and electronic properties of a-C:H films." *Thin Solid Films* 515, 7855 – 7860.

Markham, J.R., Solomon, P.R. and Best, P.E. (1990). "An FTIR based instrument for measuring spectral emittance of material at high temperature." *Rev. Sci. Instrum.,* 61, 3700–3708.

Mercatelli, L., Meucci, M. and Sani, E. (2016). "Design and test of a new facility for assessing spectral normal emittance of solid materials at high temperature." Proc. SPIE 9744, *Optical Components and Materials* XIII, 97440H, *Metall.*, 15, 553–556.

Mikhelashvili, V., Eisenstein, G., (2006). "Composition, surface morphology and electrical characteristics of Al$_2$O$_3$–TiO$_2$ nano-laminates and AlTiO films on silicon." *Thin Solid Films*, 515, 346–352.

Modest, M.F. (2003). *Radiative Heat Transfer*, Academic Press, New York.

Moghaddam, S., Lawler, J., McCaffrey, C. and Kim, J. (2005). "Heat flux-based emissivity measurement." *AIP Conference Proceedings,* 764, 32–7.

Moore, T.J., Jones, R.M., Tree, R.D., Maynes, D.R. and Baxter, L.L. (2011). "An experimental method for making spectral emittance and surface temperature measurements of opaque surfaces." *J. Quant. Spectrosc. Radiat. Transfer,* 112, 1191–1196.

Morgan, S. J., Williams, R. H. and Mooney, J. M. (1992). "An XPS study of thin Pt and Ir silicide over layer formation on Si (100)2 × 1 surfaces." *Appl. Surf. Sci.,* 56, 493-500.

Morin, G., Dersch, J., Platzer, W., Eck, M. and Haberle, A. (2012). "Comparison of linear Fresnel and parabolic trough collector power plants." *Solar Energy,* 86, 1–12.

Muranaka, T., Kikuchi, Y., Taku, Y., Shirakawa, N. and Akimitsu, J. (2008). "Superconductivity in carrier-doped silicon carbide." *Sci. Technol. Adv. Mater.*, 9, 044204-1–8.

Niklasson, C.G., Granqvist, C.G. (1983). "Surfaces for selective absorption of solar energy: an annotated bibliography 1955-1981." *J. Mater. Sci.*, 18, 3475–3534.

Ning, Y., Wang, W., Wang, L., Sun, Y., Song, P., Man, H., Zhang, Y., Dai, B., Zhang, J., Wang, C., Zhang, Y., Zhao, S., Tomasella, Bousquet., E., Cellier, J. (2017). "Optical simulation and preparation of novel Mo/ZrSiN/ ZrSiON/SiO$_2$ selective absorbing coating." *Sol. Energy Mater. Sol. Cells, 167, 178–183.*

Nuru, Z.Y., Arendse, C.J., Nemutudi, R., Nemraoui, O. and Maaza, M. (2012). "Pt–Al$_2$O$_3$ nanocoatings for high temperature concentrated solar thermal power applications." *Phys B: Condens Matter*; 407, 1634–7.

Nuru, Z.Y., Msimanga, M., Muller, T.G.F., Arendse, C.J., Mtshali, C. and Maaza, M. (2015). "Microstructural, optical properties and thermal stability of MgO/Zr/MgO multilayered selective solar absorber coatings." *Sol. Energy*, 111, 357 – 363.

Oyama, S.T. (1996). "*The Chemistry of Transition Metal Carbides and Nitrides*." Blackie Academic & Professional, London.

Palik, E.D., Bermudez, V.M. and Glembocki, O.J. (1985). "Ellipsometric Study of the etch-stop mechanism in heavily doped silicon." *J. Solid. State Sci. Technol.*, 132, 135-141.

Patnaik, P. (2002). "*Handbook of Inorganic Chemicals*." McGraw-Hill, New York.

Pearce, S.J., Charlton, M.D.B., Hiltunen, J., Puustinen, J., Lappalainen, J. and Wilkinson, J.S. (2012). "Structural characteristics and optical properties of plasma assisted reactive magnetron sputtered dielectric thin films for planar waveguiding applications." *Surf. Coat. Technol.*, 206, 4930–4939.

Peterman, E. and Wuite, G.J.L. (2011). "*Single Molecule Analysis-Methods and Protocols.*" Springer, New York.

Petzow, G. and Herrmann. (2002). "*High-performance non-oxide cermaics-11, Silicon Nitride Ceramics.*" 102, pp: 47-167, Springer-Verlag, Berlin.

Ping, S., Wu, Y., Wang, L., Sun, Y., Ning, Y., Zhang, Y., Dai, B., Tomasell, E., Bousquet, A., Wang, C. (2017). "The investigation of thermal stability of Al/NbMoN/ NbMoON/SiO_2 selective absorbing coating." *Sol. Energy Mater. Sol. Cells, 171, 253–257.*

Planck, M. (1914). "*The Theory of Heat Radiation.*" (2nd ed.). P. Blakiston's Son & Co., London.

Qi-Chu, Z. and David R.M. (1992). "Very low emittance solar selective surfaces using new film structures." *J. Appl. Phys.,* 72, 3013-3021.

Randich, E. and Allred, D.D. "Chemically vapor-deposited ZrB_2 as a selective solar absorber." (1984). *Thin Solid Films,* 83, 393–8.

Raut, H.K., Ganesh, V.A., Nair, A.S. and Ramakrishna, S. (2011). "Anti-reflective coatings: A critical, in-depth review." *Energy Environ. Sci.,* 4, 3779-3804.

Rebouta, L., Sousa, A., Capela, P., Andritschky, M., Santilli P., Matilainen, A., Pischowb, K., Barradas N.P. and Alves, E. (2015). "Solar selective absorbers based on Al_2O_3: W cermets and AlSiN/AlSiON layers." *Sol. Energy Mater. Sol. Cells,* 137, 93 –100.

Ren, D., Tan, H., Xuan, Y., Han, Y. and Li, Q. (2016). "Apparatus for measuring spectral emissivity of solid materials at elevated temperatures." *Int. J. Thermophys.,* 37, 51-71.

Restrepo, E.P., Pedro, J.A.A. and Vicente, J.B.P. (2010). "XPS structure analysis of TiN/TiC bilayers produced by pulsed vacuum arc discharge." *Dyna* 163, 64 – 74.

Ritchie, I.T. and Window, B. (1977). "Applications of thin graded-index films to solar absorbers." *Appl. Opt.,* 16, 1438–1444.

Robert, C.W. (1982). *Handbook of Chemistry and Physics*, 63rd Edn., CRC Press, FL, , P. D 63.

Rudy, E., Worcester, S. and Elkington. W. (1974). "*High Temp. High Pressures.*" 6, 447-451.

Sahoo, N.K., Thakur, S., Senthilkumar, M., Bhattacharyya, D. and Das, N.C. (2003). "Reactive electron beam evaporation of gadolinium oxide optical thin films for ultraviolet and deep ultraviolet laser wavelengths." *Thin Solid Films,* 440, 155–168.

Sani, E., Mercatelli, L., Francini, F., Sans, J.L. and Sciti, D. (2011). "Ultra-refractory ceramics for high-temperature solar absorbers." *Scr. Mater.,* 65, 775–8.

Sani, E., Mercatelli, L., Sansoni, P., Silvestroni, L. and Sciti, D. (2012). "Spectrally selective ultrahigh temperature ceramic absorbers for high-temperature solar plants." *J. Renew. Sustain. Energy*, 4, 033104–108.

Santhanam, A.T., Tierney, P. and Hunt. J.L. (1990). "*Metals Handbook, Properties and Selection*." 2, 10th edition, ASM international, 950–977.

Sayigh, A. A. M. (2012). "*Solar Energy Engineering*." Academic Press, Inc., Florida.

Schon, J.H., Binder, G. and Bucher, E. (1994). "Performance and stability of some new high temperature selective absorber systems based on metal/dielectric multilayers." *Sol. Energy Mater. Sol. Cells*, 33, 403–416.

Schuler, A., Thommen, V., Reimann, P., Oelhafen. P., Francz, G., Zehnder, T., Marcel, D., Mathys, D., Guggenheim, R. (2001). "Structural and optical properties of titanium aluminum nitride films (Ti$_{1-x}$Al$_x$N). *J. Vac. Sci. Technol. A*., 19(3), 922–929.

Selvakumar, N. and Barshilia, H.C. (2012). "Review of physical vapor deposited (PVD) spectrally selective coatings for mid- and high-temperature solar thermal applications." *Sol. Energy. Mater. Sol. Cells,* 98, 1 – 23.

Selvakumar, N., Barshilia, H.C., Rajam, K.S. and Biswas, A. (2010). "Structure, optical

properties and thermal stability of pulsed sputter deposited high temperature HfO$_x$/Mo/HfO$_2$ solar selective absorbers." *Sol. Energy. Mater. Sol. Cells,* 94(8), 1412 – 1420.

Selvakumar, N., Biswas, A., Rajaguru, K., Girish, M.G. and Barshilia, H.C. (2015). "Nanometer thick tunable AlHfN coating for solar thermal applications: Transition from absorber to antireflection coating." *Sol. Energy Mater. Sol. Cells*, 137, 219 – 226.

Selvakumar, N., Manikandanath, N.T., Biswas, A. and Barshilia, H.C. (2012). "Design and fabrication of highly thermally stable HfMoN/HfON/Al$_2$O$_3$ tandem absorber for solar thermal power generation applications." *Sol. Energy. Mater. Sol. Cells,* 102, 86–92.

Selvakumar, N., Prajith, K., Biswas, A. and Barshilia, H.C. (2015). "Optical simulation and fabrication of HfMoN/HfON/Al$_2$O$_3$ spectrally selective coating." *Sol. Energy Mater. Sol. Cells,* 140, 328–334.

Seraphin, B.O. and Meinel. A.B. (1976). "*Optical Properties of Solids: New Development*." North Holland Publ. Co., Amesterdam.

Sergeant, N.P., Pincon, O., Agrawal, M. and Peumans, P. (2009). "Design of wide-angle solarselective absorbers using aperiodic metal-dielectric stacks." *Opt. Express*, 17, 22800–12.

Setien-Fernandez, I., Echaniz, T., Gonzalez-Fernandez, L., Perez-Saez, R.B., Cespedes, E., Sanchez-Garcla, J.A., Alvarez-Fraga, L., Galindo, R.E., Albella, J.M., Prieto, C. and Tello, M.J. (2013). "First spectral emissivity study of a solar selective coating in the150-600°C temperature range." *Sol. Energy Mater. Sol. Cells,* 117, 390-395.

Shi, L., Xia, Y.D., Xu, B., Yin, J. and Liu, Z.G. (2007). "Thermal stability and electrical properties of titanium–aluminum oxide ultrathin films as high-k gate dielectric materials." *J. Appl. Phys.* 10, 1034102-1–034102-4.

Shieh, J. and Hon, M.H. (2005). "Observation of plastic deformation in TiAlCN/a-C ceramic nanocomposite coating." *Appl. Phys. A*, 80, 131–134.

Shtansky, D.V., Kiryukhantsev-Korneev, Ph.V. Sheveyko, A.N., Marvrin, B.N., Rojas, C., Fernandez, A. and Levashov, E.A. (2009). "Comparative investigation of TiAlC(N), TiCrAlC(N), and CrAlC(N) coatings deposited by sputtering of MAX-phase $Ti_{2-x}Cr_xAlC$ targets." *Surf. Coat. Technol.*, 203, 3595–3609.

Shtansky, D.V., Kuptsov, K.A., Kiryukhantsev-Korneev, Ph.V. Sheveiko, A.N., Fernandez, A. and Petrzhik, M.I. (2011). "Comparative investigation of Al- and Cr- doped TiSiCN coatings." *Surf. Coat. Technol.*, 205, 4640–4648.

Shuxi, Z. and Wackelgard, E. (2006). "Optimizing of solar absorbing three-layer coatings." *Sol. Energy Mater. Sol. Cells*, 90, 243 – 261.

Sibin, K.P., Siju, J. and Barshilia, H.C., (2015). "Control of thermal emittance of stainless steel using sputtered tungsten thin films for solar thermal power applications." *Sol. Energy Mater. Sol. Cells,* 133, 1–7.

Siow, P.C., Jaharah, A.G., Siti, H.T. and Che, H.C.H. (2012). "Analysis of Ti based hard coating performance in machining process: A review." *J. Appl. Sci.*, 12; 1882 – 1890.

Sirotti, F., Maurizio, D.S. and Giorgio, R. (1993). "Synchrotron-radiation photoemission and X-ray absorption of Fe silicides." *Phys. Rev. B* 48, 8299 – 8306.

Sitnikov, P.A., Loptain, S.I., Ryabkov, Y.I. and Grass, V.E. (2004). "Thermal stability of aluminum oxo-carbides." *Rus. J. Gen. Chem.* 74, 989–992.

Soum-Glaude, A., Bousquet, I., Thomas, L. and Flamant, G. (2013). "Optical modeling of multilayered coatings based on SiC(N)H materials for their potential use as high-temperature solar selective absorbers." *Sol. Energy. Mater. Sol. Cells,* 117, 315 – 323.

Soum-Glaude, A., Gal, A.L., Bichotte, M., Escape, C. and Dubost, L. (2017). "Optical characterization of $TiAlN_x/TiAlN_y/Al_2O_3$ tandem solar selective absorber coatings." *Sol. Energy Mater. Sol. Cells,* 170, 254–262.

Sridhara, R.D.V., Muraleedharan, K. and Humphreys, C.J. (2010). "TEM specimen preparation techniques, In Microscopy: Science, Technology, Applications and Education, eds., *A. Mendez-Villas and Diaz, J.* 1232-1244, *Formatex Research Center*, Spain.

Srinivasa, R.A. and Sakthivel, S. (2015). "A highly thermally stable Mn–Cu–Fe composite oxide based solar selective absorber layer with low thermal loss at high temperature." *J. Alloys. Compd.*, 644, 906–915.

Tallmann, D., Anasori, B. and Barsoum, M.W. (2013). "A critical review of the oxidation of Ti_2AlC, Ti_3AlC_2 and Cr_2AlC in air." *Mater. Res. Lett.* 1, 115–125.

Tesfamichael., T. (2000). "*Characterization of Selective Solar Absorbers, Department of Materials Science". Ph. D. Thesis,* The Angstrom Laboratory, Uppsala University.

Theiss, W. in Theiss, M. (ed.), *SCOUT Thin Film Analysis Software Handbook*. (Hard- and Software, Aachen, Germany), http://www.mtheiss.com. Accessed 1 Mar 2017.

Toth, E.L. (1971). "*Transition Metal Carbides and Nitrides."* Academic Press, New York.

Touloukian, Y. S., Powell, R.W., Ho, C.Y. and Nicolaou, M. C. (1974). "Thermophysical properties of matter-the TPRC data series." *Therm Diffus DTIC Doc, 10.*

Valleti, K., Krishna, D.M. and Joshi, S.V. (2014). "Functional multi-layer nitride elcoatings for high temperature solar selective applications." *Sol. Energy. Mater. Sol. Cells,* 121, 14 – 21.

Vernoika, R., Senkevich, J.J., Joannopoulos, J.D., Marin, S., Harl, R.R and Rogers, B.R. (2012). "Low emissivity high-temperature tantalum thin film coatings for silicon devices." *J. Vac. Sci. Technol.*, A31(1), 011501– 5.

Vila, M. Ca´ceres, D. and Prieto, C. (2003). "Mechanical properties of sputtered silicon nitride thin films." *J. Appl. Phys.*, 94, 7868–7873.

Waite, M.M. and Ismat, S.S. (2007). "Microstructural, optical properties and thermal stability of MgO/Zr/MgO multilayered selective solar absorber coatings." *Mater. Sci. Eng*., B 140, 64 – 68.

Waite, M.M. and Shah, S.I. (2007). "Target poisoning during reactive sputtering of silicon with oxygen and nitrogen." *Mater. Sci. Eng., B*, 140, 64-68.

Wang, X., Li, H., Yu, X. and Shi, X. and Liu J. (2012). "High-performance solution-processed plasmonic Ni nanochain-Al_2O_3 selective solar thermal absorbers." *Appl. Phys. Lett*., 101, 203109–5.

Wihelmsson, O., Palmquist, J.P., Lewin, E., Emmerlich, J., Eklund, P., Persson, P.O.A., Hogberg, H., Li, S., Ahuja, R., Eriksson, O., Hultman, L. and Jansson, U. (2006). "Deposition and characterization of ternary thin films within the Ti-Al-C system by DC magnetron." *J. Crys. Growth*, 291, 290–300.

Williams, D.B. and Carter, C.B. (2009). "*Transmission Electron Microscopy- A Textbook for Materials Science*, Springer, New York.

Woskov, P.P. and Sundaram, S.K. (2002). "Thermal return reflection method for resolving emissivity and temperature in radiometric measurements." *J. Appl. Phys.* 92, 6302-6310.

Wu, Y., Wang, C., Sun, Y., Xue, Y., Ning, Y., Wang, W., Zhao, S., Tomasella, E. and Bousquet, A. (2015). "Optical simulation and experimental optimization of Al/NbMoN/NbMoON/SiO_2 solar selective absorbing coatings." *Sol. Energy. Mater. Sol. Cells,* 134, 373 – 380.

Wu, Y., Zheng, W., Lin, L., Qu, Y. and Lai, F. (2013). "Colored solar selective absorbing coatings with metal Ti and dielectric AlN multilayer structure." *Sol. Energy. Mater. Sol. Cells,* 115, 145 – 150.

Xue, Y., Wang, C., Wang, W., Liu, Y., Wu, Y. and Ning, Y. (2013). "Spectral properties and thermal stability of solar selective absorbing AlNi–Al_2O_3 cermet coating." *Sol. Energy,* 96, 113–118.

Yamada, M., Inamoto, T., Fukumoto, M. and Yasui, T. (2004). "Fabrication of silicon nitride thick coatings by reactive RF plasma spraying materials transactions." *Mater. Trans*., 45, 3304–3308.

Yang, R., Liu, J., Lin, L., Qu, Y., Zheng, W. and Lai, F. (2016). "Optical properties and thermal stability of colored solar selective absorbing coatings with double-layer antireflection coatings." *Sol. Energy,* 125, 453–459.

Yate, L., Caicedo, J.C., Macias, A.H., Espinoza-Beltran, F.J., Zambrano, G., Murioz-Saldana, J., Prieto, P. (2009). "Composition and mechanical properties of AlC, AlN and AlCN thin films obtained by RF magnetron sputtering." *Surf. Coat. Technol*., 203, 13, 1904-1907.

Yongxin, W., Cong, W., Ying, S., Yuping, N., Yingfang, L., Yafei, X., Wenwen, W., Shuxi, Z., Eric, T. and Angelique, B. (2015). "Study on the thermal stability of Al/NbTiSiN/NbTiSiON/SiO$_2$ solar selective absorbing coating". *Sol.Energy,* 119, 18 –28.

Zekai, S. (2008). "*Solar Energy Fundamentals and Modelling Techniques*." Springer, London.

Zhang, L. and Koka, R.V. (1998). "A study on the oxidation and carbon diffusion of TiC in alumina–titanium carbide ceramics using XPS and Raman spectroscopy."*Mater. Chem. Phys.,* 57(1), 23 – 32.

Zhang, Q-C. (1998). "Stainless-steel–AlN cermet selective surfaces deposited by direct current magnetron sputtering technology." *Sol. Energy Mater. Sol Cells,* 52, 95–106.

Zhang, X., Jiang, J., Yuqiao, Z., Lin, J., Wang, F. and John, J.M. (2008). "Effect of carbon on TiAlCN coatings deposited by reactive mgnetron sputtering." *Surf. Coat. Technol*., 203, 5-7, 594–597.

Zhang, K., Hao, L., Du, M., Mi, J., Ji-Ning, W. and Jian-ping, M. (2017). "A review on thermal stability and high temperature induced ageing mechanisms of solar absorber coatings." *Renew. Sust. Energ. Rev.,* 67, 1282–1299.

Zhao, S. and Wackelgard, E. (2006). "Optimization of solar absorbing three-layer coatings." *Sol. Energy. Mater. Sol. Cells,* 90(3), 243 – 261.

Zhou, C., Xie, W. and Shao, L. (2016). "Functional multi-layer solar spectral selective absorbing coatings of AlCrSiN/AlCrSiON/AlCrO for high temperature applications." *Sol. Energy Mater. Sol. Cells, 153, 9–17.*

LIST OF PUBLICATIONS

Publications from related work

1. **Jyothi, J**., Chaliyawala, H., Srinivas, G., Nagaraja, H.S. and Barshilia, H.C. (2015). "Design and fabrication of spectrally selective TiAlC/TiAlCN/TiAlSiCN/ TiAlSiCO/TiAlSiO tandem absorber for high-temperature solar thermal power applications." *Sol. Energy Mater. Sol. Cells*, 140, 209–216.

2. **Jyothi, J**., Latha, S., Bera, P., Nagaraja, H.S. and Barshilia, H.C. (2016). "Optimization of process parameters to achieve spectrally selective TiAlC/TiAlCN/TiAlSiCN/TiAlSiCO/TiAlSiO high temperature solar absorber coating." *Sol. Energy*, 139, 58–67.

3. **Jyothi, J**., Biswas, A., Sarkar, P., Soum-Glaude, A., Nagaraja, H.S. and Barshilia, H.C. (2017). "Optical properties of TiAlC/TiAlCN/TiAlSiCN/TiAlSiCO/TiAlSiO tandem absorber coatings by phase-modulated spectroscopic ellipsometry." *Appl. Phys. A*, 123, 496-1–10.

4. **Jyothi, J**., Soum-Glaude, A., Nagaraja, H.S. and Barshilia, H.C. (2017). "Measurement of high temperature emissivity and photothermal conversion efficiency of TiAlC/TiAlCN/TiAlSiCN/TiAlSiCO/TiAlSiO spectrally selective coating." *Sol. Energy Mater. Sol. Cells*, 171, 123–130.

Publications from other work

1. Atasi, D., **Jyothi**, **J.** Kamanio, C., Barshilia, H.C. and Basu, B. (2016). "Spectrally selective absorber coating of WAlN/WAlON/Al$_2$O$_3$ for solar thermal applications." *Sol. Energy Mater. Sol. Cells*, 157, 716–726.

2. Nitant, G., Kavya, M.V., Yogesh, R.G., **Jyothi, J.** and Barshilia, H.C. (2013). "Superhydrophobicity on transparent fluorinated ethylene propylene films with nano-protrusion morphology by Ar+O$_2$ plasma etching: Study of the degradation in hydrophobicity after exposure to the environment." J. Appl. Phys., 114,164307 1-8.

Conferences Attended

1. Functional and Energy Materials, Manufacturing & Structures (FAEMMS – 2013), Organized by School of Engineering Sciences and Technology, University of Hyderabad, Indian National Academy of Engineering, India & Royal Academy of Engineering, United Kingdom. March 24-26, 2013.

2. **Jyothi. J,** Nagaraja, H.S. and Barshilia, H.C. (2016). **"**A new spectrally selective tandem absorber TiAlC/TiAlCN/TiAlSiCN/TiAlSiCO/TiAlSiO for high temperature solar thermal applications." In MECS- 2016, March 11-13, 2016, Pondicherry (**Best Poster Award**)**.**

3. **Jyothi. J**, Nagaraja, H.S. and Barshilia, H.C. (2016), Effect of composition on designed tandem absorber to achieve selective properties for high temperature solar thermal applications. In ICNANO-2016, April 21-23, 2016, Bangalore.

Conference Proceedings

1. **Jyothi. J**, Nagaraja, H.S. and Barshilia, H.C. (2016). "Effect of composition on designed tandem absorber to achieve selective properties for high temperature solar thermal applications." *Materials Today Proceedings* (accepted)

CURRICULUM VITAE

Jyothi J

Senior Research Scholar

Department of Physics

National Institute of Technology, Surathkal

Mangalore-575025

India.

E-mail: jyothi.jambu@gmail.com

Phone number: 7406008663.

EDUCATION

2009-2011: I completed **M. Sc. (Physics)** with specialization in Electronics from Sri Padmavathi Women's Degree and Post-Graduation College under Sri Venkateshwara University in Tirupathi.

2006-2009: I completed **B. Sc. (Computer Science)** from Sri Padmavathi Women's Degree and Post-Graduation College in Tirupathi.

2004-2006: I completed **Intermediate** from CAN Junior College in Tirupathi.

2003-2004: I completed **S.S.C.** from Swarna Vidyalaya High School in Tirupathi.

ACHEIVEMENTS AND AWARDS

All India 54th rank in CSIR- UGC National Eligibility Test (NET) for Junior Research Fellowship (JRF) and eligibility Lectureship in "Physical Sciences" held on 19th June, 2011.

RESEARCH EXPIERENCE

Sep. 2014- Sep. 2017: Senior Research Fellow (CSIR), Surface Engineering Division, National Aerospace Laboratories (CSIR), Bangalore, India.

Sep. 2012- Sep.2014:   Junior Research Fellow (CSIR), Surface Engineering Division, National Aerospace Laboratories (CSIR), Bangalore, India.

Jan. 2012- Aug.2012:   Junior Research Fellow, Material Science and Research Center, Department of Physics, IIT Madras, India.

PERSONAL INFORMATION

Date of Birth   15-06-1989

Gender   Female

Marital status   Married

Nationality   Indian

Residential Address   H. No: 13-6-616J

                      Pedda Kapu Layout

                      Tirupathi-517501

                      Andhra Pradesh, India.